AN ABSTRACT OF THE THESIS OF

Pooya Tadayon for the degree of Doctor of Philosophy in Chemistry presented on February 6, 1998. Title: Determination of Interfacial Tension from Optical Measurements of Nucleation Rates.

Abstract approved: _____

Joseph W. Nibler

_____

Glenn T. Evans

Theoretical and experimental techniques have been used to measure the liquid-vapor, solid-vapor, and solid-liquid interfacial tension of simple molecules. In the theoretical work, molecular theory of capillarity along with a simple Lennard-Jones potential has been used to calculate the surface tension of supercooled liquids. The results offer justification for linear extrapolation of surface tension data in the normal liquid range into the supercooled regime. Extensions of the theory to solids was less successful, perhaps due to the presence of shear forces or lack of appropriate potential parameters for solids.

Experimentally, Coherent anti-Stokes Raman Spectroscopy (CARS) and Rayleigh scattering have been used to measure the vapor-liquid and vapor-solid nucleation rates in an adiabatic jet expansion. It is found that these rates are of the order

of 10^{26}-10^{27} m^{-3} s^{-1}, depending on the expansion conditions. Using homogeneous nucleation theory, we have calculated the liquid-vapor interfacial tension of supercooled methane, ethylene, and argon from the experimentally determined nucleation rates. The experimental values are in good accord with the theoretical predictions and with values extrapolated from the normal liquid range. This method has also been used to determine the solid-vapor interfacial tension of nitrous oxide, acetylene, and carbon dioxide. These values for solids are the first of their kind and are found to be consistent with indirect comparisons made using Young's equation.

Finally, the liquid-solid nucleation rate for small clusters (i.e. r = 5-15 nm) of nitrogen and methane were also determined and are found to be about 10^{29}-10^{30} m^{-3} s^{-1}. These rates and nucleation theory have been used to deduce the solid-liquid interfacial tension and the results are in accord with values predicted by the empirical relation of Turnbull and Tegze's theoretical model.

Determination of Interfacial Tension from Optical Measurements of Nucleation Rates

by

Pooya Tadayon

A THESIS

submitted to

Oregon State University

in partial fulfillment of
the requirements for the
degree of

Doctor of Philosophy

Presented February 6, 1998

Commencement June 1998

Doctor of Philosophy thesis of Pooya Tadayon presented on February 6, 1998.

APPROVED:

Co-Major Professor, representing Chemistry

Co-Major Professor, representing Chemistry

Chair of Department of Chemistry

Redacted for privacy

Dean of Graduate School

I understand that my thesis will become part of the permanent collection of Oregon State University libraries. My signature below authorizes release of my thesis to any reader upon request.

Redacted for privacy

Pooya Tadayon, Author

ACKNOWLEDGMENT

I would like to begin by thanking my advisors and my friends, Dr. Joseph W. Nibler and Dr. Glenn T. Evans. Joe has been very supportive and patient with me during the past four years, and thanks to him, I will leave Oregon State not only with a degree but also the tools necessary to succeed in the real world. I am grateful that Joe gave me the freedom to pursue my own interests and explore areas of physical chemistry outside the realm of his research. Although he probably does not realize it, Joe has had the most influence in my life outside of my parents. I am forever indebted to him.

It has been a pleasure working with Dr. Evans on the theoretical portions of my research. This collaboration came about by accident and I am glad that it did for it made me appreciate the theoretical viewpoint of science. One of the things I will miss the most about OSU will be the spontaneous non-scientific conversations I had with Dr. Evans in the hallways of Gilbert Hall. I am fortunate to have had the opportunity to work with him.

Helpful discussions and comments from the following individuals are greatly appreciated: Dr. John Loeser, Dr. Philip Watson, Dr. Darrah Thomas, Dr. Adel Faridani, Dr. Anthony Diaz, and Dr. Philip Minarik. I extend a special thanks to Dr. Minarik for teaching me how to use the equipment in the lab.

My parents have been an integral part of my success and I wish to thank them for their patience, understanding, encouragement, guidance, and support. They have made

numerous sacrifices in order for me to obtain an education and it is difficult to imagine how my life would be without them.

I would like to take a moment to thank Ms. Amy Edmonson for her never ending love and support. These last few months have been especially 'rocky' and she has been there every step of the way, cheering me up with her beautiful smile and kind words. I am certainly a better person because of her.

I thank the following individuals for making my stay in Corvallis enjoyable:

- ☺ The Corvallis Bahá'í Community for providing much needed spiritual support.
- ☺ Nizar "Plumber Boy" Krayem for making me laugh with his asinine sense of humor, always bailing me out with his design expertise, showing me the difference between good and bad movies, and introducing me to Vince.
- ☺ Vahid "Pumpkinhead" Motazedian for giving me useless stock tips, getting me in trouble with several ROTC guys, and sticking a potato in my tailpipe.
- ☺ Tom "Cougar" Gannon for spotting me in the gym, creating matchups based on real characters in the gym, watching *really* bad movies with me, and letting me beat him at backgammon on a regular basis. Tom is also the only person who has witnessed me doing statistical mechanics in my sleep.
- ☺ Dr. Anthony Diaz for all the hours we spent on the tennis court, including the time when he separated his shoulder trying to return my blistering forehand.
- ☺ Nick Drapela for making prank phone calls and discussing politics, football, and religion with me.

TABLE OF CONTENTS

TABLE OF CONTENTS (continued)

TABLE OF CONTENTS (continued)

LIST OF FIGURES

LIST OF FIGURES (continued)

LIST OF FIGURES (continued)

LIST OF FIGURES (continued)

LIST OF TABLES

LIST OF APPENDICES

LIST OF APPENDIX FIGURES

LIST OF APPENDIX TABLES

To Humanity

Man is the supreme Talisman. Lack of a proper education hath, however, deprived him of that which he doth inherently possess. Through a word proceeding out of the mouth of God he was called into being; by one word more he was guided to recognize the Source of his education; by yet another word his station and destiny were safeguarded. The Great Being saith: Regard man as a mine rich in gems of inestimable value. Education can, alone, cause it to reveal its treasures, and enable mankind to benefit therefrom.

- Bahá'u'lláh

DETERMINATION OF INTERFACIAL TENSION FROM OPTICAL MEASUREMENTS OF NUCLEATION RATES

1. INTRODUCTION

The work presented in this thesis is a continuation of the ongoing cluster research in our laboratory at Oregon State University. In the past, various spectroscopic techniques have been used to determine cluster properties such as phase, size, and temperature. Recently, however, there has been a growing interest in studying the mechanism of phase transitions in clusters. These experiments have shown that it is possible to measure the rate of transformation from one phase to another which then allows us to deduce the interfacial tension between the two phases. This is a physical quantity which is extremely difficult to measure when one of the phases is a solid.

In this work, we present theoretical and experimental studies aimed at determining the liquid-vapor, solid-vapor, and solid-liquid interfacial tensions. We begin in this chapter by giving a formal definition of interfacial tension followed by a summary of previous experiments and results. Chapter 2 contains a brief description of homogeneous nucleation theory along with other pertinent information necessary to understand the work in this thesis. The experimental setup is described in Chapter 3. In Chapter 4, we present the molecular theory of interfacial tension for the liquid-vapor interface and calculate values for several systems in the supercooled region. In Chapter 5, we demonstrate how spectroscopy can be used to measure the rate of formation of liquid and solid clusters from the vapor phase. These results are then used to deduce the

interfacial tension of supercooled liquids and solids. Finally, experiments directed at studying the kinetics of liquid-solid phase transitions for several molecular systems are presented in Chapter 6.

1.1 Interfacial Tension

In a system composed of two phases α and β, the molecules at or near the surface dividing the phases are in a different environment than are molecules in the bulk phase. This region between the two phases where molecules interact with molecules of both phases is referred to as the interface layer. The interface is not homogeneous like the bulk phases and therefore exhibits properties different from those of the bulk phase. One quantity that is used to characterize these properties is the interfacial free energy or interfacial tension.

Interfacial tension is important for a large variety of phenomena (e.g. droplet formation, cellular phagocytosis, capillary action, flotation, and lubrication) which occur everyday in nature or take place in industrial processes.[1-4] To understand the role of the interface in such phenomena, we must first understand the physical nature of interfacial tension.

1.1.1 Thermodynamic Definition[1-2]

Molecules in an interface region have a different average free energy than molecules in a bulk phase. Consider a flask containing a liquid in equilibrium with its

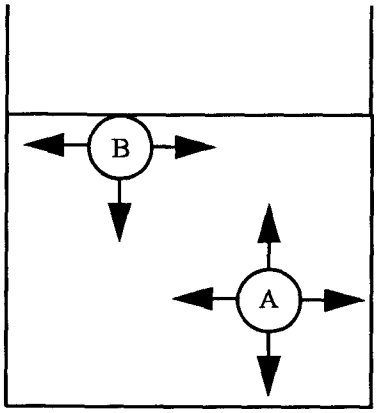

Figure 1.1 Attractive forces on molecules in the bulk and surface regions.

vapor. Figure 1.1 shows a molecule in the bulk liquid region and a molecule at the surface of the liquid. Molecule A is interacting with other liquid phase molecules from all directions. Molecule B, however, experiences fewer attractions from liquid phase molecules and is in an environment which is in between that of the pure liquid and vapor. As a result, molecule B has a higher average free energy than molecule A.

The number of molecules in the interface is proportional to the area A of the interface. To increase the area of the interface by dA, one needs to bring molecules from the bulk phase into the surface region. Because molecules in the interface have a higher free energy than molecules in the bulk phase, positive work is required to increase the area. The amount of work is proportional to dA and the proportionality constant is given by σ and is called the interfacial free energy or interfacial tension. This number is positive because work has to be performed on the system. The expression for the interfacial tension is given by

$$\sigma = \left(\frac{dG}{dA}\right)_{T,P} \tag{1.1}$$

where dG is the change in the free energy of the system. Nature requires that this quantity be minimized for processes at constant temperature and pressure. For this reason, systems tend to assume a configuration of minimum surface area. As a result, water droplets form a sphere because this is the geometrical shape with the lowest surface area to volume ratio.

1.1.2 Mechanical Definition[5]

Consider a two phase system, α (gas) and β (liquid), confined by a piston in a rectangular box of dimensions l_x, l_y, and l_z (Figure 1.2). Allow the piston to move to the right a distance dl_y and exert a force F_y on the system. The total work done by the piston on the system is given by

$$dw_{rev} = F_y\, dl_y \tag{1.2}$$

Since this work changes both the interior volume and the surface area of the interface, (1.2) can be written as

$$F_y\, dl_y = -P_N\, dV + \sigma\, dA \tag{1.3}$$

where P_N is the pressure normal to the interface in each of the bulk phases. The volume of the box is given by $V = l_x\, l_y\, l_z$ and thus, $dV = -\, l_x\, l_z\, dl_y$. The area of the interface

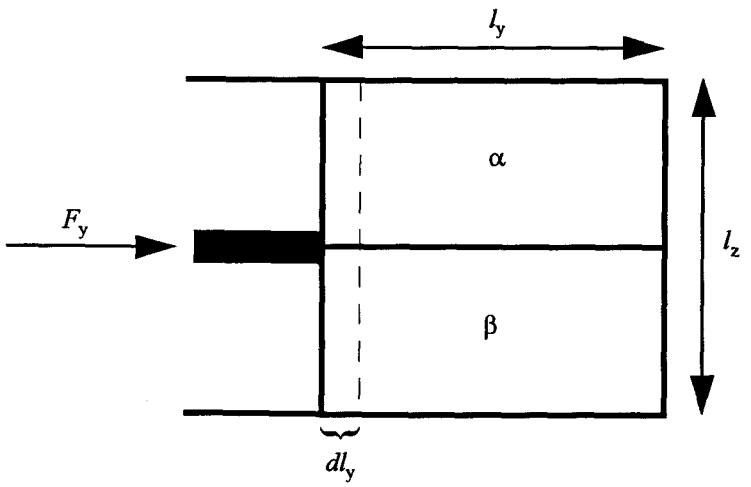

Figure 1.2 A two phase system confined by a piston in a rectangular box. The interface separating the two phases lies in the *xy*-plane with the *x*-axis perpendicular to the plane of the page.

between the two phases is $A = l_x l_y$ and therefore $dA = - l_x dl_y$. (Since the volume of the box and the area of the interface are decreasing for the positive displacement dl_y, dV and dA must be negative.) As a result, (1.3) reduces to

$$F_y = P_N l_x l_z - \sigma l_x \tag{1.4}$$

The pressure P_y exerted by the piston is F_y/A_{pist}, where A_{pist} is the piston's area. Division of (1.4) by $A_{pist} = l_x l_z$ gives

$$\sigma = [P_N - P_y] l_z \tag{1.5}$$

Note that the pressure exerted by the piston does not equal the system pressure because of the interfacial tension. The presence of the interface causes a force σl_x to be exerted

by the system on the piston in a direction opposite that of the systems pressure. In other words, interfacial tension is an attractive force which acts parallel to the surface and prevents the surface from extending.

The pressure, P_N, in the bulk phases is uniform in all directions. In the interface region, the pressure in the z direction is also equal to P_N. This is due to the mechanical stability of the interface and is a requirement of the hydrostatic equilibrium equation given by[5]

$$\frac{dP_N}{dz} = 0 \tag{1.6}$$

The pressure in the x and y directions, however, are less than P_N according to (1.5). Since the interface region is not homogeneous, the pressures P_x and P_y are functions of the z coordinate. As a result, (1.5) can be rewritten as[5]

$$\sigma = \int_{-\infty}^{\infty} [P_N - P_T(z)]\, dz \tag{1.7}$$

where $P_T(z)$ is the tangential pressure. This equation is generally referred to as the mechanical definition of interfacial tension. It is interesting to consider the magnitude of P_T. The thickness of the surface of a liquid is typically on the order of 10Å and the value of the interfacial tension is about 15 mN/m. As a result, the average value of $[P_N - P_T(z)]$ is 150 atm. Since the normal pressure is 1 atm at the boiling point, the average value of $P_T(z)$ is about -150 atm.[5]

1.2 Interfaces & Interfacial Phenomenon

There are five different types of interfaces whose properties depend on the respective interfacial tension.[1-2] These are the liquid-vapor (σ_{lv}), solid-vapor (σ_{sv}), liquid-liquid (σ_{ll}), solid-liquid (σ_{sl}), and solid-solid (σ_{ss}) interfaces. In the case of the liquid-vapor and solid-vapor interfaces where one phase is gaseous the term surface tension is more commonly used instead of interfacial tension. Although all these interfaces are of considerable interest, in this thesis we shall focus our attention on the liquid-vapor, solid-vapor, and solid-liquid interfaces. As we shall see later, the interfacial tensions of these three interfaces are related to each other by a simple formula.

The contribution of the interfacial tension to the total free energy is negligible for macroscopic systems. However, for microscopic systems (i.e. particles smaller than 10^{-6} m) where the ratio of surface area to volume is large, the interfacial tension determines the principal characteristics of the system.[6-7] For example, the equilibrium vapor pressure of nanometer sized water droplets is three times the vapor pressure of the bulk due to the surface tension. Also, it has been shown that smaller particles which have a larger surface area to volume ratio are more soluble and exhibit faster reaction kinetics than larger particles.

The interfacial tension of an interface can also be altered by addition of impurities to the system.[8] This is of paramount importance in industry. For example, in waterproof materials, the surface has been treated with a substance which increases the interfacial tension of the interface and forces the water to bead. Conversely, surfactants are added to insecticides to reduce the interfacial tension so that the liquid will spread over the

leaves. This process is also useful in the printing industry. If the paper-ink interfacial tension is too low, the ink will spread over the paper and produce a poor quality impression. On the other hand, if the interfacial tension is too high, the ink will bead on the paper and prevent it from drying. As a final example, the walls of a steam condenser are often coated with wax to increase the interfacial tension. This prevents the water from spreading on the walls and reducing the condensation efficiency.

Other areas where interfacial tension plays a major role is in adsorption processes, crystal growth, and in reaction rates and phase transformations of small particles.[8-11] One area of interest over the past decades has been the kinetics of phase changes in the gaseous and condensed states. Turnbull,[12-13] Buckle,[14] Bradley,[15] Bartell,[16-21] and others[22- 23] have demonstrated that the rate of nucleation is heavily dependent on the magnitude of the interfacial tension. Research in this area, however, has been hampered by lack of knowledge about the exact value of the interfacial tension.

1.3 Measurements of Interfacial Tension

There are many experimental methods available to determine the liquid-vapor surface tension in the normal liquid range. These methods include the capillary rise method, the forced bubble method, and the stalagmometer method.[6-7] However, there are no methods available to measure σ_{lv} in the supercooled regime. These values are typically approximated by extrapolating the data in the normal liquid range into the supercooled region. Another approach to estimating σ_{lv} for supercooled liquids is to use theoretical methods.

Unlike the situation for σ_{lv}, there is no reliable or facile method to directly measure the surface tension σ_{sv} for a solid-vapor interface. The only available experimental data is by Wulff, who in 1949 measured the surface tension of solid copper.[24] Wulff found that when a thin copper wire is heated to near its melting point, it behaves as a viscous liquid. Thus, a wire with radius r shortens because of the surface tension forces. This force of contraction was balanced by means of weights hung at the end of the wire. At the point where the strain rate is equal to zero, the weight downwards is equal to the surface forces $\pi r\sigma_{sv}$ upwards. This method yields a σ_{sv} value of 1370 mJ/m^2 at the melting point, a value somewhat higher than the σ_{lv} value of 1303 mJ/m^2 at the same temperature.[25]

As for σ_{sv}, direct measurement of a solid-liquid interfacial tension (σ_{sl}) is extremely difficult. To our knowledge, there are only two methods available that allow direct measurement of σ_{sl}. The first method involves measuring the dihedral angle between the liquid and two small crystals separated by a grain boundary (see Figure 1.3). In 1969, Hobbs and Ketcham[26] used this method to determine a σ_{sl} value of 33 mJ/m^2 for water at 273 K; this is significantly less than a σ_{lv} value of 75.6 mJ/m^2 at the same temperature.[25]

The second method is a cleavage technique developed by Bailey and Kay in 1966 which takes advantage of (1.1).[27] In this method, one determines the work done to cleave a thin strip of a solid surface surrounded by a liquid. High resolution multiple beam interference fringes are then used to locate the line of bifurcation and hence to determine the area of the new interface formed during cleavage. Using this technique,

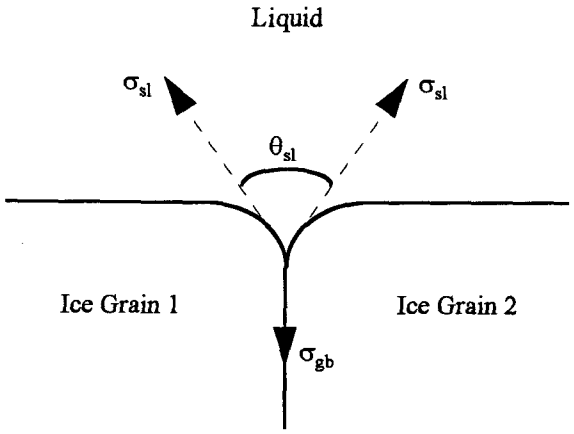

Figure 1.3 Diagram of grain boundary grooves at the solid-liquid interface. σ_{gb} is the grain boundary interfacial tension.

Bailey and Kay have determined a σ_{sl} value of 107.3 mJ/m^2 for mica in contact with water.

An indirect, but more convenient, method of determining σ_{sl} takes advantage of homogeneous nucleation theory, which states that the rate of nucleation of liquid droplets is a function of σ_{sl}. In 1952 Staveley and Thomas were able to determine nucleation rates by measuring the freezing rate of fine mists of supercooled liquid carbon tetrachloride in prechilled air.[23] They determined a value of 6.67 mJ/m^2 for σ_{sl} at 200 K. Recently, Bartell and coworkers used electron diffraction methods to deduce values for σ_{sl} by measuring the rate of freezing of supercooled nanoclusters formed in a supersonic expansion using electron diffraction methods.[16-17] They obtained a σ_{sl} value of 5.48 mJ/m^2 for carbon tetrachloride at ~175 K. Both values are much lower than the σ_{lv} value of 32.3 mJ/m^2 at 250 K.[25]

In our laboratory, we have a devised a method similar to Bartell's which allows us to indirectly measure σ_{lv}, σ_{sv}, and σ_{sl} for various substances. This is done by forming supercooled clusters in a supersonic expansion and measuring the nucleation rate using Coherent anti-Stokes Raman Spectroscopy (CARS) and/or Rayleigh scattering. Minarik has recently used this technique to deduce a σ_{sl} value of 11.8 mJ/m^2 at 140 K for acetylene.[28] Minarik has also shown that this method can be used to measure σ_{ss} in cases where a solid-solid phase transition exists; he deduced a σ_{ss} value of 3.2 mJ/m^2 at 135 K between the cubic and orthorhombic phases of acetylene. As expected, both values are considerably lower than the σ_{lv} value of 18.9 mJ/m^2 at the melting temperature of 192 K.[25]

1.4 Interfacial Tension of Simple Molecules

In our laboratory, we have employed CARS and Rayleigh methods to measure the liquid-vapor, solid-vapor, and solid-liquid interfacial tension of various simple molecules such as N_2, N_2O, CH_4, CO_2, C_2H_4, and C_2H_2. These systems were chosen for several reasons. First, these molecules are in the gaseous state at room temperature, which allows us to manipulate more easily the initial temperature and pressure of the free jet expansions. Secondly, most of these molecules play crucial roles in the composition of the atmosphere. For example, carbon dioxide and methane are the two largest contributors to the greenhouse effect and methane is known to be a major factor in the formation of ozone in the troposphere.[29] In the stratosphere and mesosphere, where temperatures are as low as 160 K, some of these molecules are expected to form liquid

and/or solid particles. These molecules are also known to exist in liquid and solid forms on the surface of other planets.

Nucleation processes are important in many atmospheric phenomenon, such as acid rain and the destruction of ozone in the polar stratosphere.[11,29] The formation of sulfuric acid particles and polar stratospheric clouds, whose surface catalyzes the destruction of ozone in the polar regions, are believed to be caused by the nucleation of supercooled molecules. Thus, in order to better understand these events, it is important to have a fundamental understanding of nucleation kinetics, especially of the interfacial tension, since the nucleation rate is heavily dependent on this value.

2. BACKGROUND INFORMATION

2.1 Generation of Clusters

In this section we shall consider the mechanical aspects for the production of clusters by expanding a gas in a free jet expansion. Free jets are produced by expanding a gas from a high pressure region into vacuum through a small aperture of diameter D. The interesting characteristic of a free jet is that as the gas expands, its mean forward velocity increases but the width of the velocity distribution, and hence the temperature, decreases. This is a result of flow work being done on the gas as it expands.

The most important quantity for characterizing a free jet expansion is the Mach number. All properties of interest such as the temperature, pressure and the velocity of the jet are a function of the Mach number.[30] The Mach number is the ratio of the gas velocity to the local adiabatic speed of sound and is given by

$$M = \frac{\upsilon}{(\gamma RT/m)^{1/2}} \tag{2.1}$$

where υ is the velocity of the gas, R is the gas constant, m is the molecular mass and γ is the heat capacity ratio, given by C_p/C_v. The denominator of (2.1) corresponds to the speed of sound in an ideal gas at some temperature T. Because the Mach number changes at every position in the jet, it is customary to define M as a function of X/D where X is the distance from the nozzle. From measurements of large scale expansions,

it is found that the Mach number, for *X/D* values greater than 0.5, is given by the empirical relation

$$M = \left(\frac{X}{D}\right)^{\gamma-1}\left[C_1 + C_2\left(\frac{X}{D}\right)^{-1} + C_3\left(\frac{X}{D}\right)^{-2} + C_4\left(\frac{X}{D}\right)^{-3}\right] \qquad (2.2)$$

where C_1, C_2, C_3 and C_4 are constants specific to planar (2D) and axisymmetric (3D) expansions.[30] The local properties of interest at a given *X/D* value are then given by

$$\frac{T}{T_0} = \left[1 + \left(\frac{\gamma-1}{2}\right)M^2\right]^{-1} \qquad (2.3)$$

$$\frac{P}{P_0} = \left(\frac{T}{T_0}\right)^{C_p/R} \qquad (2.4)$$

$$\frac{\rho}{\rho_0} = \left(\frac{T}{T_0}\right)^{1/(\gamma-1)} \qquad (2.5)$$

$$\frac{\upsilon}{\upsilon_\infty} = \left(\frac{T}{T_0}\right)^{1/2} M\left(\frac{\gamma-1}{2}\right)^{1/2} \qquad (2.6)$$

where T_0, P_0, and ρ_0 are the initial temperature, pressure, and number density, respectively. Figure 2.1 shows that temperature, pressure, and density fall quickly as a function of *X/D* while the velocity increases towards a terminal velocity, $\upsilon_\infty = (2RT_0/m)^{1/2}(1\text{-}1/\gamma)^{-1/2}$.[30] Note that T is the translational temperature in these expressions and this may be less than the rotational or vibrational temperatures for polyatomic

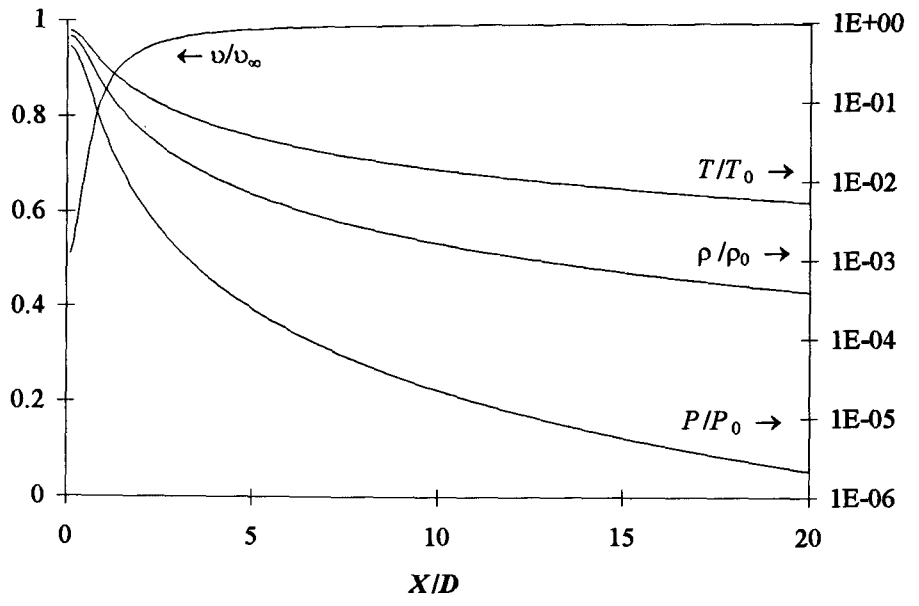

Figure 2.1 Free jet centerline properties for a monatomic molecule ($\gamma = 5/3$) as a function of X/D. The arrows indicate the corresponding axis.

molecules. The fact that the molecules cool dramatically in a free jet expansion is the feature that allows us to condense a supersaturated gas into a liquid or solid cluster.

2.2 Homogeneous Nucleation Theory

It is well known that the formation of a critical nucleus is the key step in a phase change.[14] According to classical nucleation theory, the nucleation rate is similar to the rate of a first order homogeneous reaction.[12] The rate of such a reaction is given by an Arrhenius-type equation

$$k = A \exp(-\Delta E_a / k_B T) \tag{2.7}$$

where k is the rate constant, A is the pre-exponential factor, ΔE_a is the Arrhenius activation energy, and k_B is Boltzmann's constant. The activation energy is the energy required for a reaction to occur. Extending this idea to a phase transition, we assume that there is a free energy barrier ΔG^* to the formation of a critical nucleus. Hence, the expression for the nucleation rate is[15]

$$J_{ij} = A_{ij} \exp\left(-\Delta G_{ij}^* / k_B T\right) \tag{2.8}$$

where J is the nucleation rate from phase j to i.

The structure of the critical nucleus is comprised of bulk and surface components whose relative contributions to the free energy are governed by size. The free energy for the formation of the nucleus is usually expressed as[15]

$$\Delta G_{ij}(n) = -n \upsilon_m \Delta G_{v,ij} + \alpha \sigma_{ij} \upsilon_m^{2/3} n^{2/3} \tag{2.9}$$

where n is the number of molecules in the nucleus, $\Delta G_{v,ij}$ is the change in free energy per unit volume of a bulk molecule due to the phase transition, υ_m is the molecular volume, and σ_{ij} is the interfacial tension between phases i and j. The variable α is a shape factor such that the number of molecules in the surface of a nucleus of n molecules is $\alpha n^{2/3}$ and is equal to $(36\pi)^{1/3} \approx 4.84$ for a spherical nucleus or 6 for a cubic nucleus. (See Appendix A for derivation of the shape factor.)

The exact shape of the nucleus depends on the phase of the embryo. Liquid nuclei minimize their surface free energy by assuming a spherical configuration. Solid

nuclei, however, are different from their liquid counterparts in that the molecules within the nucleus are not able to move about freely and are locked into specific lattice sites. Thus, the shape of a solid embryo is dependent on the crystal structure of the bulk material. For example, using the concept of minimal surface free energy for a given volume, Tegze has determined that the shape of the nucleus for simple cubic and face centered cubic crystals are the cube and the truncated octahedron, respectively.[31]

The value of α changes only slightly for different shapes and as a result, plays a minor role in nucleation theory. Therefore, for the sake of simplicity and clarity, we will assume a spherical nucleus throughout this thesis and express (2.9) in terms of the radius. Using the relation $n = (4/3)\pi r^3/\upsilon_m$, (2.9) reduces to

$$\Delta G_{ij}(r) = -\frac{4}{3}\pi r^3 \Delta G_{v,ij} + 4\pi r^2 \sigma_{ij} \tag{2.10}$$

The first term in (2.10) represents the decrease in free energy due to a phase transition while the second term represents the increase in free energy due to the formation of a surface. It can be shown that the free energy increases to a maximum value at some critical radius r^* and then decreases with increasing r. At the maximum, $\partial[\Delta G(r)]/\partial r = 0$ and the critical size and the free energy barrier for the formation of a nucleus are given by

$$r_{ij}^* = \frac{2\sigma_{ij}}{\Delta G_{v,ij}} \tag{2.11}$$

$$\Delta G_{ij}^{*} = \frac{16\pi\sigma_{ij}^{3}}{3\,\Delta G_{v,ij}^{2}} \tag{2.12}$$

The pre-exponential factor, A_{ij}, of equation (2.8) is referred to as the kinetic coefficient of nucleation and is defined as the rate of mass exchange between the critical nucleus and the surrounding phase.[22] Although the general forms of (2.8), (2.11), and (2.12) hold for all phase transitions, we shall see in the next two sections that the expressions for A_{ij} and $\Delta G_{v,ij}^{*}$ are different depending on whether nucleation is triggered from the vapor, liquid, or solid phase.

Note that (2.12) contains a σ_{ij} to the third power. Once (2.12) is substituted into the rate equation (2.8), it becomes obvious that the nucleation rate is extremely sensitive to the value of σ_{ij}. In fact, it can be shown that varying the value of σ_{ij} by 10-20% changes the nucleation rate by several orders of magnitude. This is unfortunate for it limits the predictive capability of the theory in cases where accurate interfacial tension data is not available. Looked at from a different viewpoint, however, the relation means that it is not crucial to measure extremely accurate nucleation rates in order to obtain reasonable values for σ_{ij}. This is an important advantage which we exploit.

2.2.1 Nucleation from the Vapor Phase

Liquid and/or solid clusters are typically formed from a gas that is supersaturated. According to nucleation theory, a gas must be supersaturated in order to form a critical

nucleus of finite radius in equilibrium with the vapor.[15] Supersaturation is characterized in terms of the supersaturation ratio which is given by

$$S = \frac{P_v}{P_{eq}} \tag{2.13}$$

where P_v is the vapor pressure of the gas and P_{eq} is the equilibrium vapor pressure. In a jet expansion, P_v is the local pressure and is given by (2.4). In the case where $S > 1$, homogeneous nucleation can occur spontaneously and the gas transforms to the more stable condensed phase.

The size and free energy barrier to the formation of a critical nucleus are very sensitive to the exact value of the supersaturation ratio. Equations (2.11) and (2.12) indicate that the critical size and free energy barrier are both functions of $\Delta G_{v,ij}$, which for a vapor to liquid transition is given by

$$\Delta G_{v,lv} = \frac{k_B T}{v_m} \ln S \tag{2.14}$$

assuming ideal gas behavior for the vapor. Figure 2.2 shows a plot of the free energy of formation of critical nuclei as a function of nucleus size and supersaturation ratio. Note that as the value of S increases, the size of the critical nucleus decreases thus making nucleation energetically favorable. The value of S in a typical jet expansion is of the order of $10\text{-}10^3$ which corresponds to a critical radius of 4-10 Å.

The process of forming liquid or solid clusters from the vapor phase in a jet expansion can be illustrated by an isentrope-coexistence curve of the type shown in

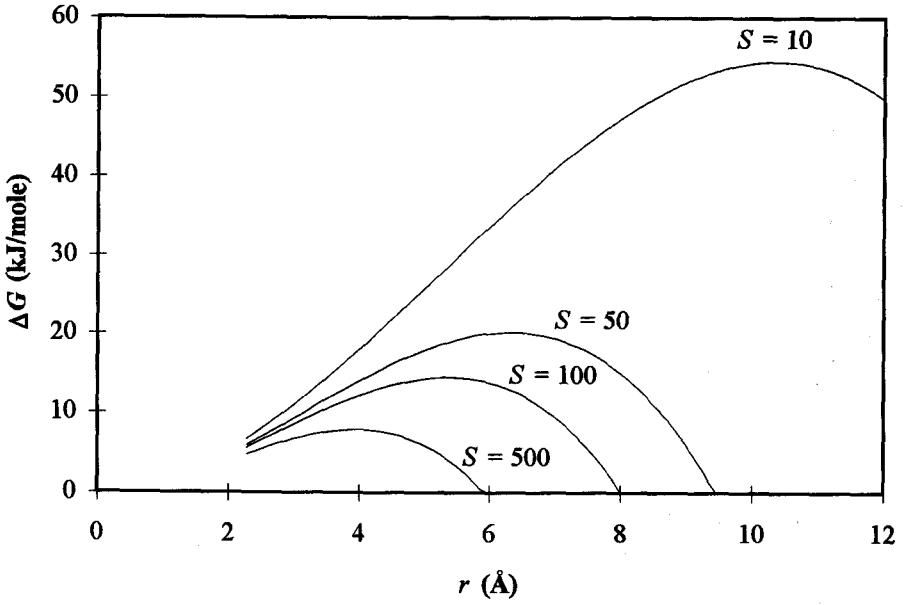

Figure 2.2 Free energy for the formation of critical nuclei in gaseous methane at various supersaturation conditions using $T = 60$ K and $\sigma_{lv} = 25$ mJ/m^2 .

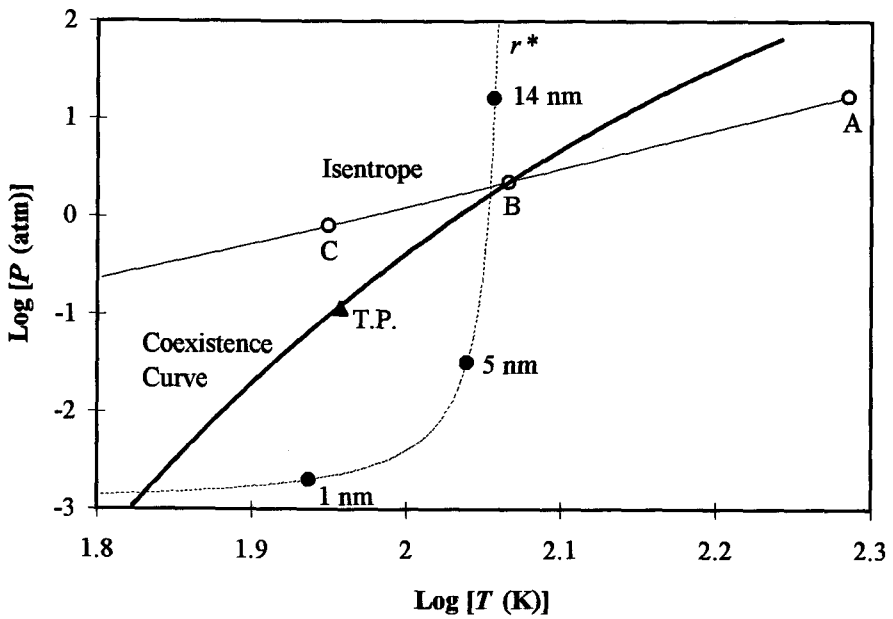

Figure 2.3 A typical isentrope-coexistence curve for neat methane. The triangle labeled T.P. indicates the triple point. ($P_0 = 17$ atm, $T_0 = 193$ K, $\sigma_{lv} = 25$ mJ/m^2).

Figure 2.3. The thick line represents the liquid-vapor and solid-vapor coexistence curves obtained from equilibrium vapor pressure data. The thin line is the isentrope for the expanding gas, which is calculated from (2.5), and the dashed line is the size of the critical nucleus as a function of temperature.

Point A indicates the stagnation condition which is characterized by the initial temperature T_0 and pressure P_0. As the gas expands, it follows the isentrope until it crosses the coexistence curve at point B, where the supersaturation ratio $S = 1$. However, clusters are not formed at this point since the rate of forming critical nuclei is negligible due to the large size of the critical nucleus.

Beyond point B, the gas becomes supersaturated and continues to cool. The rate of forming critical nuclei also begins to increase as the size of the critical nucleus decreases. Once the nucleation rate is appreciable, clusters of critical size begin to form at point C; this is the onset of condensation.

The nucleation rate is also a function of the pre-exponential factor A_{lv} which in this case is the rate of molecular exchange between the vapor and the nucleus and is referred to as the velocity of condensation.[32] To a first approximation, this is the rate at which molecules of mass m strike a nucleus of surface area A and is given by

$$A_{lv} = Z_w \rho A = \frac{P_v}{(2\pi m k_B T)^{1/2}} \left(\frac{P_v}{k_B T}\right)\left(4\pi r_{lv}^{*2}\right) \tag{2.16}$$

where Z_w is the gas kinetic collision frequency per unit area of surface per second and ρ is the molecular density. Here, it is assumed that all molecules hitting the nucleus will

stick; as we shall see in Section 2.4.1, this is not true. Some corrections to (2.16) have been proposed which take into consideration the rate of evaporation of nuclei. By assuming that nucleation results from a series of reactions in which nuclei grow or shrink one atom at a time, Bradley[15] and Frenkel[32] have rigorously derived an equation the same as (2.16) with a correction factor β,

$$\beta = \frac{1}{n_{lv}^*}\left(\frac{\Delta G_{lv}^*}{3\pi k_B T}\right)^{1/2} = \frac{\upsilon_m}{4\pi r_{lv}^{*2}}\left(\frac{4\sigma_{lv}}{k_B T}\right)^{1/2} \tag{2.16}$$

where n_{lv}* is the number of molecules in the critical nucleus. Thus, A_{lv} reduces to

$$A_{lv} = \left(\frac{2\sigma_{lv}}{\pi m}\right)^{1/2}\left(\frac{P_v}{k_B T}\right)^2 \upsilon_m \tag{2.17}$$

Note that (2.14) and (2.17) also apply in the case where solid nuclei are formed.

The initial phase of the clusters is a function of the stagnation conditions and can be controlled to some extent. Liquid clusters are favored by adjusting the conditions such that the isentrope crosses the coexistence curve well above the triple point (if close to the triple point, solid clusters could also form). Solid clusters are always favored by choosing conditions where the isentrope crosses the coexistence curve below the triple point. Another method of controlling the phase of the clusters is to mix the sample with a carrier gas such as He or Ne. This changes the slope of the isentrope, which is given by C_p/R. It also changes the intersection point B since only the partial pressure of the sample is used in (2.5).

2.2.2 Nucleation from the Liquid Phase

Once liquid clusters are formed, they rapidly grow in size and become warmer than the expanding gas around them due to the heat of condensation. At this point, the temperature of the clusters no longer follow the isentrope and instead is given by the coexistence curve. Due to their small size, the clusters have a high vapor pressure and as a result they cool by evaporation at rates as high as 10^6 K/s. These high cooling rates rapidly reduce the vapor pressure of the clusters until the evaporation rate becomes so low that the temperature-time profile flattens. This "final" temperature is referred to as the evaporative cooling temperature, T_{evp}, and is chosen by Bartell to be the temperature at which the vapor pressure of the bulk liquid is 0.4 Pa.[16,21] It is possible to cool the clusters below their evaporative cooling temperature by using carrier gas (He or Ne), which acts as a heat sink.

At temperatures as low as T_{evp} the clusters are sufficiently supercooled that the formation of a critical nucleus becomes energetically favorable. The free energy can be calculated from (2.10) with $\Delta G_{v,ij}$ written as[16]

$$\Delta G_{v,sl} = \frac{1}{\upsilon_m N_a} \int_{T_m}^{T} \Delta S_{fus}(T)\, dT \tag{2.18}$$

Here $\Delta S_{fus}(T)$ is the molar entropy of fusion of the supercooled liquid estimated from

$$\Delta S_{fus}(T) = \int_{T_m}^{T} \frac{\Delta C_p(T)}{T} dT \tag{2.19}$$

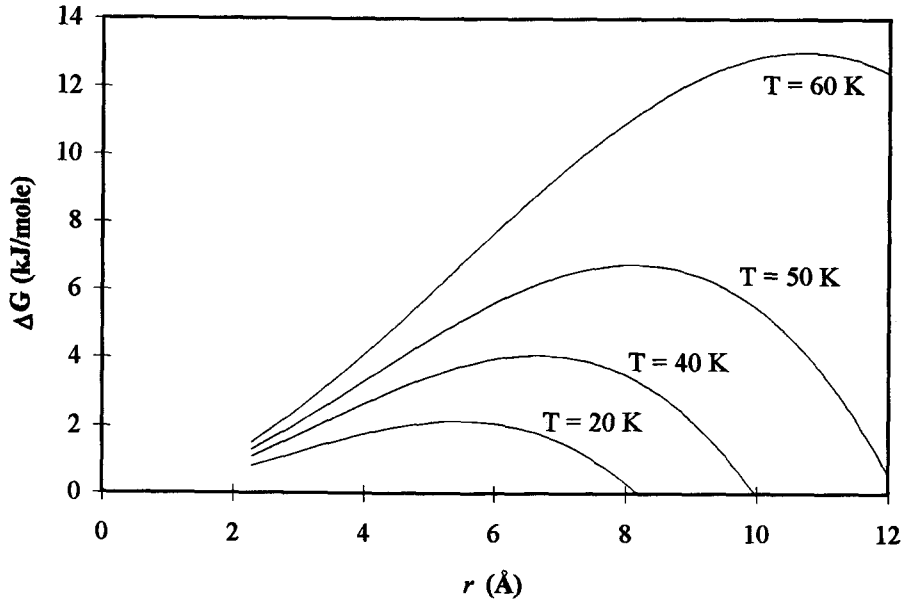

Figure 2.4 Free energy for the formation of critical nuclei in liquid methane ($T_{evp} \sim 45$ K) as a function of temperature and nucleus size assuming a constant value of $\sigma_{sl} = 3.5$ mJ/m^2.

where ΔC_p is the difference between experimental liquid and solid heat capacities extrapolated into the supercooled region.

Figure 2.4 shows a plot of the free energy as a function of nucleus size at various temperatures. The behavior of the free energy is very similar to that observed for vapor-liquid transitions (Figure 2.2). The plot shows that at high temperatures the size of the critical nucleus is too large and the energy barrier to the formation such a nucleus is too high. As the temperature is lowered, the size of the critical nucleus decreases and as a result the formation of a nucleus becomes energetically favorable.

The kinetics of nucleation for liquid-solid transitions is much less well understood than for vapor-liquid transitions mainly because of the form of the pre-exponential factor.

The rate of mass exchange between the solid nucleus and the liquid phase, which is represented by A_{sl}, is a function of the activation energy for the assimilation of a molecule by a growing nucleus. There is little information available about this activation energy and it is commonly approximated as the activation energy for viscous flow as given by Eyring's expression.[33] It is assumed that this barrier to flow determines the rate of diffusion to the nucleus and that the liquid molecules do not need additional time or energy to reorient themselves to join the lattice of the nucleus. With these assumptions, A_{sl} is given by[16]

$$A_{sl} = \frac{2(\sigma_{sl} k_B T)^{1/2}}{\upsilon_m^{5/3} \eta} \tag{2.20}$$

where η is the viscosity of the liquid. It should be said that it is not clear if (2.20) is an accurate approximation in the supercooled region, due to the rapidly increasing value of the viscosity as T is lowered. However, for lack of better knowledge, we will follow others and use this current model.

2.3 Nucleation Rates & Spectroscopy

The single most important quantity required for calculating the interfacial free energy is the nucleation rate, J. It is then of paramount importance to determine the nucleation rate experimentally. Here we show how the nucleation rate can be determined using Coherent anti-Stokes Raman Spectroscopy (CARS).

2.3.1 Coherent anti-Stokes Raman Spectroscopy

The theory for CARS has been described in detail before.[28,34] Figure 2.5 shows an energy level diagram for the CARS process. The upper two states are referred to as virtual states and are not necessarily quantum states of the molecule. The two lower levels are the ground vibrational state (v = 0) and the first excited vibrational state (v = 1) of the molecule. Two waves with fixed frequency ω_1 and a wave with tunable frequency ω_2 are mixed to generate a fourth wave with frequency $\omega_3 = 2\omega_1 - \omega_2$. The intensity of the anti-Stokes signal is given by

$$I_3 = k|\chi^{(3)}|^2 I_1^2 I_2 \tag{2.21}$$

where I_i is the intensity of the beam of frequency ω_i, k is a collection of constants, and $\chi^{(3)}$ is the third order susceptibility, which is proportional to the Raman cross section and the molecular density.

If the difference between ω_1 and ω_2 is equal to the energy difference between the two vibrational states, then the excited state is selectively populated. The molecules in this excited state are then stimulated by a second ω_1 photon to a higher virtual state. The anti-Stokes photon at ω_3 is generated as the molecules relax to the ground state. (It should be noted that, in fact, this process occurs simultaneously and not via step-by-step events as described above and by the energy level diagram.)

The vibrational spectrum of the clusters provides several pieces of information. First, the frequencies of a given vibrational mode in the vapor, liquid, and solid phases

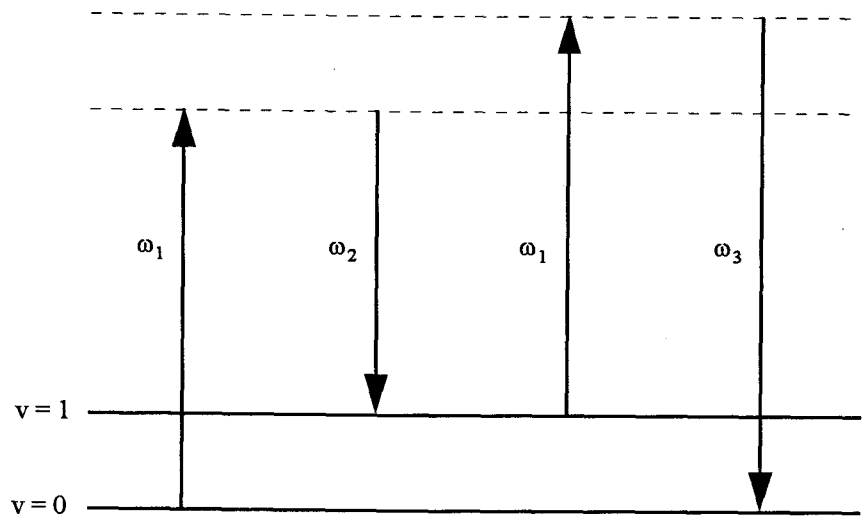

Figure 2.5 CARS energy level diagram. The dashed lines represent virtual states.

are readily distinguishable in most cases. Since the CARS signal intensity is proportional to the molecular density squared, the area under a CARS peak can be related to the number of molecules present in each phase at a given time. This information can be used to calculate the fraction of clusters that are liquid and/or solid at time *t*.

In addition, the temperature of the clusters can be determined by monitoring the frequency shift of the liquid and solid peaks. It is known that the vibrational frequency of a substance shifts with temperature.[35] This is a result of the increased interaction between the molecules as the temperature is lowered. If attractive forces dominate, the increased interaction pulls the outer atoms away from the central atom, thereby increasing the length of the bond and effectively reducing the force constant of the bond. As a result, the vibrational frequency decreases with decreasing temperature. In order to determine the temperature dependence of the vibrational frequencies of the clusters, it is

necessary to study bulk samples of liquid and solid in a cryostat. Here we assume that the clusters are large enough (i.e. ~10^5 molecules) that they are similar to the bulk material. Cluster temperatures are important in determining cluster size and the temperature at which nucleation takes place in liquid clusters.

2.3.2 Vapor-Liquid Nucleation

The nucleation rate is defined as the rate of formation of critical nuclei per unit volume and is given by[16]

$$J = \frac{dN/dt}{V} \tag{2.22}$$

where N is the number of critical nuclei and V is the volume in which the observed nucleation events are taking place. In the case of nucleation from the vapor phase, V is taken to be the CARS probing volume (Figure 3.3).

The CARS spectrum yields information regarding N and t. The X/D position at which clusters are first observed sets an upper limit to the value of t. If we assume that each cluster is a result of one nucleation event, then the number of clusters N_C at this X/D position gives an estimate for N. The number of clusters at a given position can be determined from

$$N_{\text{Total}} = N_M + N_C M_C \tag{2.23}$$

where N_{Total} is the predicted total number of monomers calculated from (2.5), N_M is the actual number of monomers observed, and M_C is the number of monomer units per cluster and is deduced from the mean cluster size. According to (2.23) if there are no clusters present (N_C = 0), then the number of monomers observed is equal to the calculated value. The area under the peaks in a CARS spectrum gives us the ratio of monomers to clusters, N_M/N_CM_C, which along with (2.23), can be used to obtain an estimate for N. The procedure described above will be discussed in greater detail in Chapter 5.

2.3.3 Liquid-Solid Nucleation

Equation (2.22) also applies in the case of a liquid-solid transition with V being replaced by V_l which is the total volume of the liquid in which the nucleation events are taking place. The liquid to solid nucleation rate, J_{sl}, is deduced from the freezing rate, which we can determine from the fraction of clusters that are frozen at various time intervals. A key assumption here is that the rate of freezing is determined by the rate of nucleation, and not by the rate of crystal formation or loss of heat of fusion.

According to current nucleation models,[36-37] once a solid nucleus is formed, the cluster can freeze adiabatically or isothermally. Figure 2.6 shows a diagram describing both processes. In the slow isothermal case, a solid nucleus is formed and the cluster begins to freeze. This in turn raises the temperature of the cluster due to the heat of fusion and prevents further nucleation events from taking place. The cluster continues to freeze isothermally by exchanging heat with the surroundings through evaporation and

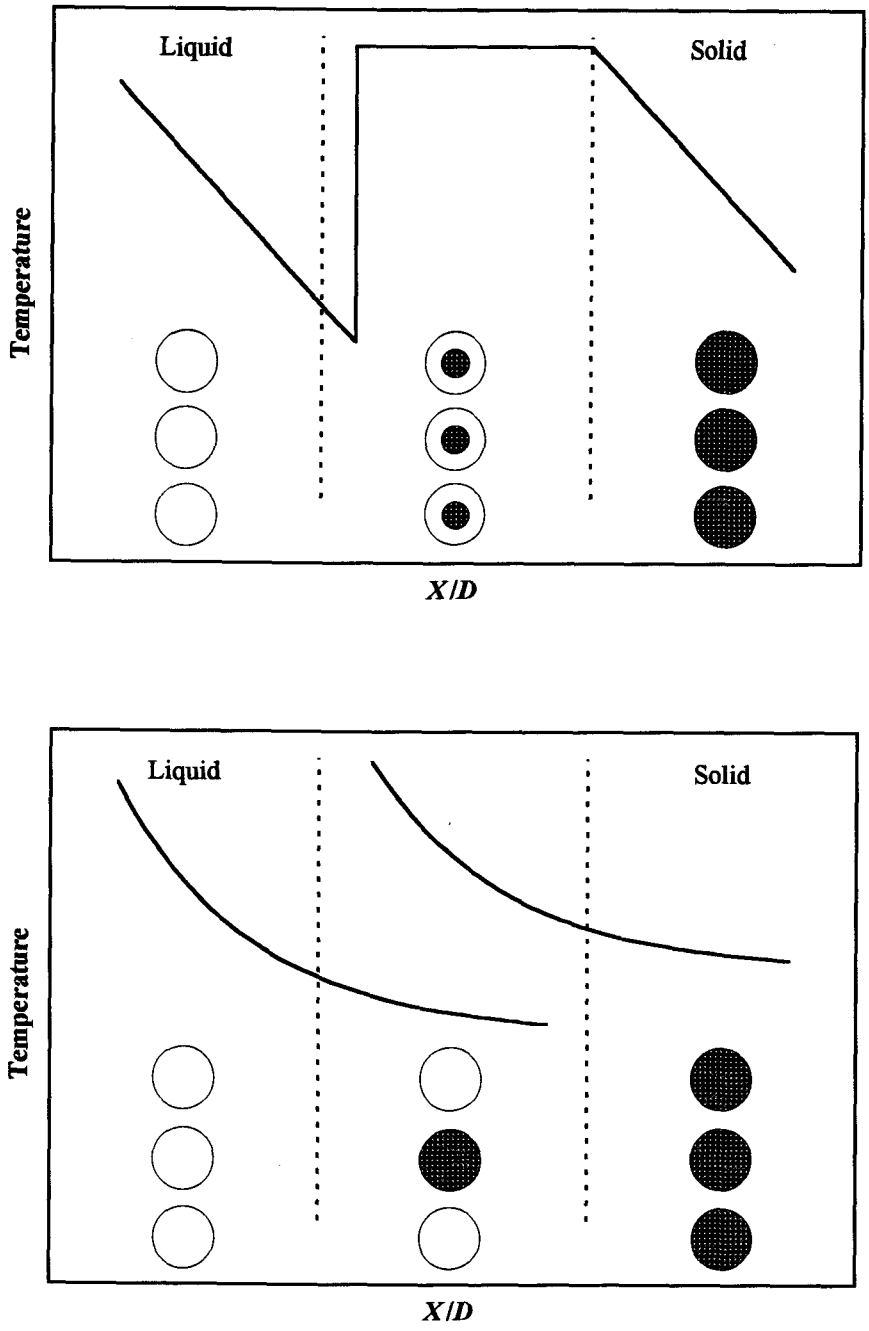

Figure 2.6 Qualitative plots of the isothermal (top) and adiabatic (bottom) freezing models. The model shows that isothermal freezing takes place at the transition temperature while the cluster exchanges heat with its surroundings. In the adiabatic case, freezing occurs at some temperature below the melting point and the cluster absorbs the excess heat. The change in temperature is given by $\Delta H_{fus}/C_{p,liq}$ and it is assumed that the extent of supercooling exceeds this.

inelastic collisions with the surrounding gas. As a result, the rate of freezing is not only dependent on the formation of the solid nucleus, but also on the rate of evaporation and the number of collisions with the surrounding gas.

In the fast adiabatic case, as soon as a solid nucleus is formed, the entire cluster freezes and absorbs the heat of fusion. Therefore, the freezing rate is equal to the rate of formation of the first solid nucleus. This model is supported by Minarik's acetylene data which show that both liquid and solid clusters are present in the freezing zone.[28] More importantly, the temperature of the solid is ~35 K higher than that of the liquid, which is in good agreement with a predicted temperature change of $\Delta H_{fus}/C_{p,l}$ ~33 K.

If freezing is adiabatic, then we can determine the nucleation rate from the freezing rate by assuming that the total volume of liquid consists of N_T clusters, each of volume V_C. If N_S of these clusters are frozen, then the remaining liquid volume is given by $(N_T - N_S)V_C$ and (2.22) can be rearranged to give

$$\frac{dN_S}{dt} = JV_C(N_T - N_S) \tag{2.24}$$

Integrating (2.24) and letting N_S/N_T be the fraction f of clusters that are frozen gives

$$f(t) = 1 - \exp[-JV_C(t - t_0)] \tag{2.25}$$

where $f(t)$ is the number fraction of clusters that are frozen at time t and t_0 is the time at which freezing begins. From this, it is seen that the nucleation frequency, JV_C, can be obtained by fitting the data to (2.25).

The above treatment assumes that the clusters are of equal size. This is in fact not the case. The size of the clusters is distributed over a range of values and is dependent on the stagnation conditions. Researchers have used various computer modeling methods to account for this size distribution.[18] We have found that the results are relatively insensitive to the exact value of the cluster size and hence an average cluster size will be used.

The material presented in this and the previous section shows that the experimentally determined nucleation rate can be used to calculate the interfacial free energy. Before undertaking this task, however, we need to know more about the physical properties of supercooled liquids.

2.4 Physical Properties of Supercooled Clusters

In order to calculate σ_{ij} from the nucleation rate, we must first have some knowledge about the cluster size, density, vapor pressure, and viscosity. The vapor pressure and viscosity are particularly difficult to determine due to the lack of data in the supercooled regime. In this section we will discuss the methods used to establish reasonable values for these parameters.

2.4.1 Size

The cluster size is required to calculate the liquid to solid nucleation rate from the nucleation frequency and to obtain an estimate for M_C. Several different methods have

been proposed for determining cluster sizes. These methods include Rayleigh scattering,[38] mass spectrometry,[39] electron diffraction,[16,40] and cooling curve models. In our experiments, cooling curve models were chosen to determine the cluster size.

The theory behind the cooling curve model is as follows. Figure 2.7 shows what can happen to a cluster once it is formed. The clusters can undergo elastic collisions in which neither the size nor the temperature is affected. Clusters can also undergo inelastic collisions in which the size of the cluster is not affected but the temperature is lowered. Inelastic collisions have a cooling effect because the temperature of the colliding gas molecule is much lower than the temperature of the cluster. Therefore, through collision, the gas molecules are able to remove some energy from the cluster in the form of heat.

The amount of the heat being carried away through inelastic collisions is determined by an effective heat capacity which is a function of the heat capacity of the colliding molecule and the thermal accommodation coefficient, α. The purpose of α is to take into account the efficiency of the energy transfer, which in an inelastic collision, is governed by the mass of the colliding molecule and the mass of the cluster molecules. The effective heat capacity is given by

$$C_{p,\text{eff}} = \sum_i \alpha_i C_{p,i} \tag{2.26}$$

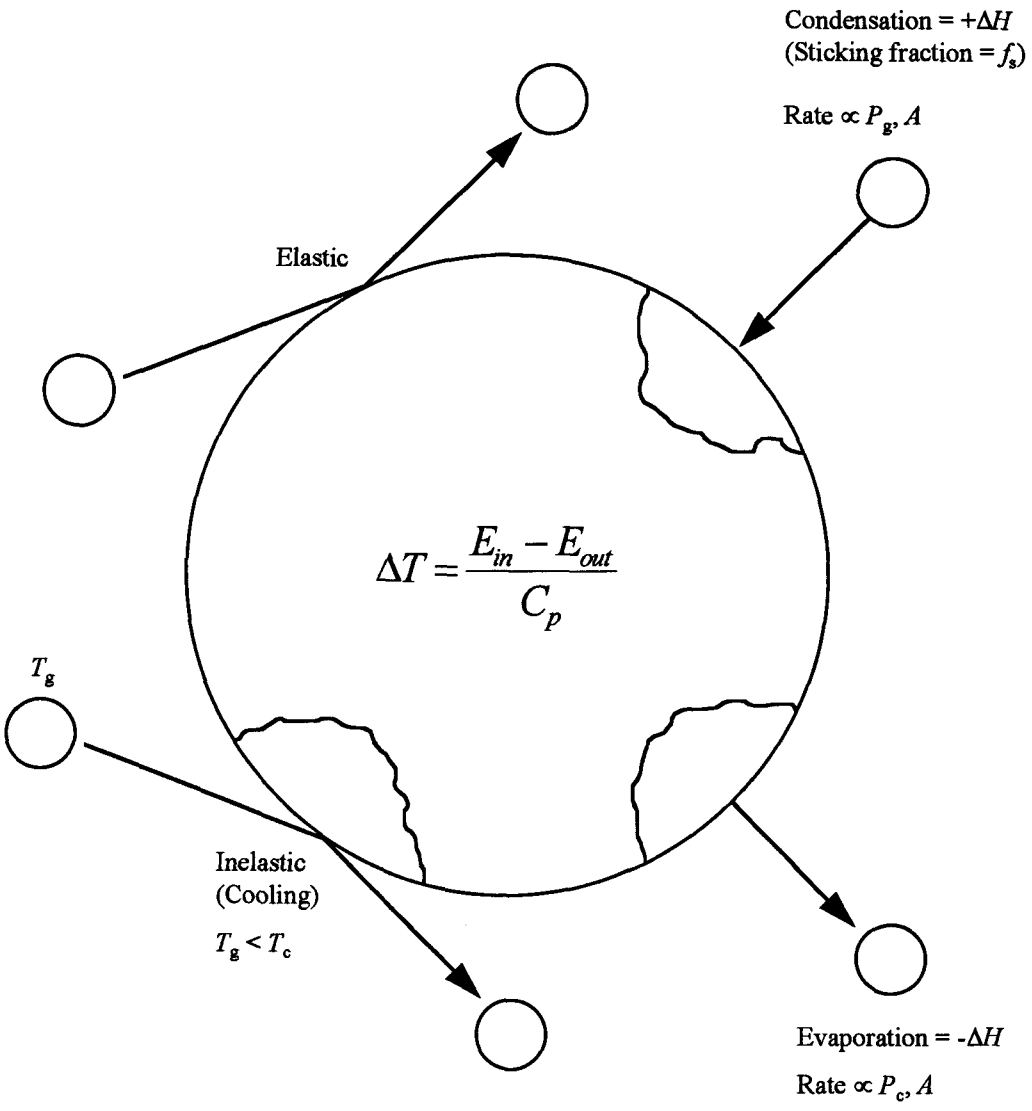

Figure 2.7 Diagram showing the processes by which a cluster can change in size and temperature.

where the subscript i indicates the different types of colliding molecules. α is in the range of 0-1; it is been our experience that the calculated cluster size is insensitive to the exact value of α, hence it is typically chosen to yield the best fit for the cooling curve.

Two processes which affect both the size and temperature of clusters are condensation and evaporation. Condensation occurs when a colliding gas sticks to the cluster, thus increasing the size of the cluster. When the gas condenses onto the surface of the cluster, it releases its heat of vaporization and increases the overall temperature of the cluster. Condensation is a function of the background gas pressure, the surface area of the cluster, and the sticking fraction. The gas pressure and the surface area determine the number of collisions that the cluster undergoes. However, not all collisions result in condensation. Therefore, it is necessary to define a sticking fraction, f_s, which is the fraction of molecules that actually condense onto the cluster. This is a variable that is adjusted in the fitting routine and typically has values between 0.01 to 0.2. It might be noted that these values are relatively small compared to values of 0.5-0.9 which have been reported for condensation of small molecules on cold flat surfaces;[41] this is perhaps reasonable since the surface is so strongly curved for small clusters. The total increase in the energy of the cluster in a time interval Δt is given by

$$E_{\text{in}} = Z_{\text{w}}^{(P_g,T_g)} A f_s \Delta H_{\text{vap}} \Delta t \tag{2.27}$$

where the superscript on Z_w indicates the pressure and temperature at which the gas kinetic collision frequency is calculated.

We have already shown that clusters can lose energy through inelastic collisions. Clusters can also lose energy and decrease in size through evaporation. The rate of evaporation is a function of the vapor pressure and the surface area of the cluster. Evaporation carries away energy in the form of heat from the cluster and has an overall cooling effect. The total loss of energy of a cluster through evaporation and inelastic collisions is given by

$$E_{\text{out}} = \left[Z_{\text{w}}^{(P_{\text{C}},T_{\text{c}})} A \, \Delta H_{\text{vap}} + Z_{\text{w}}^{(P_{\text{g}},T_{\text{g}})} A \, C_{\text{p,eff}} \, (T_{\text{c}} - T_{\text{g}}) \right] \Delta t \qquad (2.28)$$

One can then calculate the change in temperature of the cluster by

$$\Delta T_{\text{c}} = \frac{E_{\text{in}} - E_{\text{out}}}{C_{\text{p,c}}} \qquad (2.29)$$

where $C_{\text{p,c}}$ is the heat capacity of the cluster at constant pressure. The size of the cluster plays an important role in the magnitude of E_{in} and E_{out}. If the cluster is small, then condensation and evaporation will have a large effect on the temperature of the cluster. However, if the cluster is very large, then the temperature effect of condensation and evaporation will be negligible. More details on this cluster cooling model can be found in the M.S. thesis of Alan Richardson.[42]

2.4.2 Density & Vapor Pressure

The liquid cluster molar volume and vapor pressure appear in nucleation theory in several places and values for these are needed at various temperatures. Although there is extensive density and vapor pressure data available for the systems we will be studying, none extend into the supercooled region. We thus consider approximate extrapolations based on data for other systems.

The density of most simple organic liquids is close to the value for the crystalline solid; the difference is usually no more than 10%.[43] The closeness in the values of the solid and liquid are indicative of the similarity in the molecular packing. The extensive data collected on density show that the density of many liquids varies linearly with temperature, following an equation in the form of

$$\rho = A + BT \tag{2.30}$$

where A and B are empirical constants. The deviation from linearity is usually found to be less than 0.1% even over a liquid temperature range of 200 K. There is little information on the variation of density with temperature for supercooled liquids but the available data shows that the linearity of (2.30) extends well into the supercooled region.[43] Of course, linear extrapolation of the density can eventually make the liquid denser than the crystalline solid. However, in practice we find that our results are insensitive to the exact value of the density and (2.30) is regarded as an adequate approximation.

Less certain are the values of vapor pressure for a supercooled liquid for which there is virtually no existing experimental data. In the normal liquid range, vapor pressure data for liquids and solids are well represented by the Clausius-Clapeyron equation of the form

$$\log P = A + \frac{B}{T} \tag{2.31}$$

where A and B are empirical constants. For lack of better knowledge regarding the behavior of P in the supercooled region, we shall fit the existing data to (2.31) and extrapolate into the supercooled regime.

2.4.3 Viscosity

Viscosity enters into nucleation theory in the pre-exponential factor A_{sl} since movement of liquid molecules is involved in the formation of a solid nucleus. Just as before, there is little data available for the viscosity of liquids in the supercooled region, forcing us to extrapolate existing experimental data.

It is common knowledge that the viscosity of a liquid increases rapidly as temperature decreases due to the decrease in free volume.[43] In other words, as the temperature decreases, the molecules pack more closely to each other, thereby decreasing the free volume available in which the molecules can flow. The temperature dependence of viscosity for liquids is generally given by[44]

$$\log \eta = A + \frac{B}{T} + CT + DT^2 \tag{2.32}$$

where A, B, C and D are constants specific to a liquid. In the supercooled region, the viscosity of the liquid continues to increase rapidly, up to the glass transition temperature, T_g. This is the point at which the material begins to behave like a glass and is defined as the temperature at which the viscosity reaches a value of 10^{12} Pa s.[45-47] For comparison, the viscosity of water at room temperature is $\sim 10^{-4}$ Pa s while that of ice is $\sim 10^{14}$ Pa s.[6]

Unfortunately, (2.32) does not increase rapidly in the supercooled regime and predicts T_g values that are much lower than the experimentally determined glass transition temperatures. As a result, Doolittle has proposed that the viscosity of a liquid in the supercooled regime can be approximated by[43]

$$\eta = A' \exp\left[\frac{B'}{T - T^*}\right] \tag{2.33}$$

where A', B', and T^* are constants. Table 2.1 lists the glass transition temperatures obtained by fitting liquid viscosity data for several substances to (2.33). There is reasonable agreement between the experimental and estimated T_g values, indicating that (2.33) is a better approximation for the temperature dependence of viscosity than (2.32). Fortunately, the calculated value of σ_{sl} is relatively insensitive to the exact value of the viscosity. To illustrate this, a 10^3 order increase in viscosity lowers the value of σ_{sl} by only 10%.

Table 2.1 Glass transition temperatures obtained from experiment and fit of viscosity data of reference 44 to (2.32) and (2.33). Experimental T_g values are from references 48-50.

Substance	$T_{g\,2.32}$ (K)	$T_{g\,2.33}$ (K)	$T_{g\,exp}$ (K)
CH_4	16	8	< 4.2
C_3H_8	16	40	46
C_3H_6	21	45	55
n-C_4H_{10}	31	63	58
CCl_4	50	110	135

3. EXPERIMENTAL DESIGN

3.1 CARS Apparatus

The CARS setup in our laboratory is shown in Figure 3.1. The primary laser is a seeded Quanta Ray DCR-1A Nd^{+3}:YAG laser which produces 8 ns pulses of 1064 nm light at 10 Hz with a spectral linewidth of 0.003 cm^{-1}. The seeder is a Lightwave Electronics S-100 monolithic, laser diode pumped, unidirectional resonator giving a cw single frequency beam of about 2 mW. This output is introduced into the cavity of the pulsed YAG laser to produce single mode operation.

A KDP crystal within the laser housing is used to double the 1064 nm output from the laser. The infrared beam is separated from the resulting 532 nm light by a Pellin-Broca prism and steered into a beam dump. The green beam is sent through a beam splitter and two-thirds (~66 mJ/pulse) is used to pump the dye laser while the remaining third (~33 mJ/pulse) serves as the ω_1 beam. The ω_1 beam is sent through a time delay path (~2 m) so that it will arrive in the molecular beam chamber at the same time as the lower frequency dye beam (ω_2). The ω_1 beam is then sent through a rotatable 532 nm half-wave plate which is used to assure vertical polarization, thus maximizing the signal. This beam is split in two by a 50% reflecting dichroic mirror. The two ω_1 beams are then steered by micrometer controlled prisms which allow fine tuning to achieve spatial overlap of the beams.

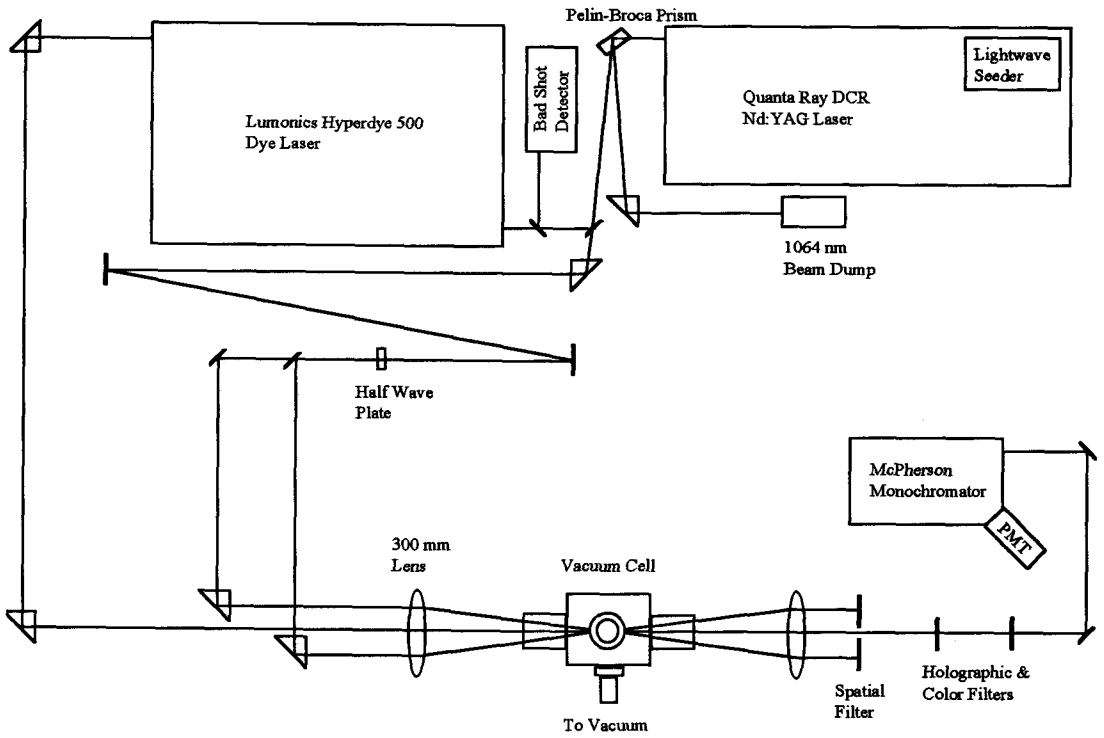

Figure 3.1 Schematic diagram of the CARS apparatus at Oregon State University.

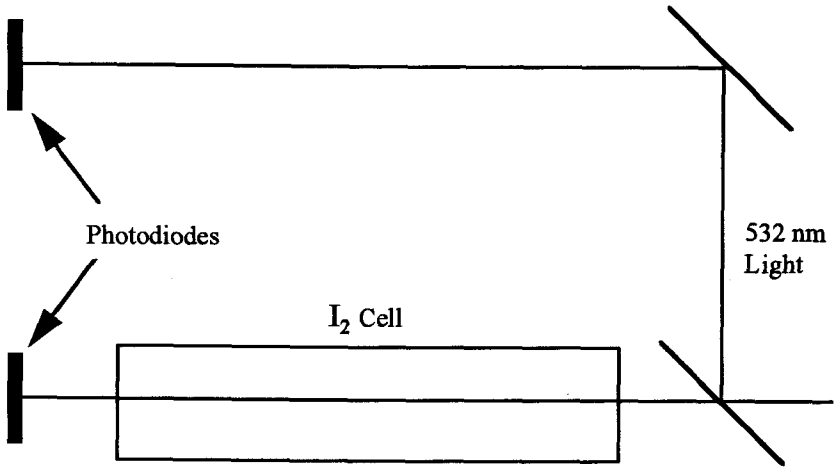

Figure 3.2 Schematic diagram of the bad shot detector.

A small fraction of the beam used to pump the dye laser is split off into the bad shot detector shown in Figure 3.2. The purpose of the bad shot detector is to ensure the stability of the ω_1 beam by detecting shots that are multi-mode and not seeded. The seeder frequency is adjusted so that the second harmonic generation lies on a strong iodine absorption line. Inside the detector, the ω_1 beam is split in two with one-half going through an iodine cell and the other half serving as a reference. Two photodiodes are used to monitor the intensity of the beam going through the cell and the reference beam. If the laser is not seeding at the desired frequency, the two photodiodes will have equivalent signals and a TTL pulse is generated by the detector to indicate that a bad shot has occurred. However, if the laser is running single mode, then the signal at the two photodiodes will be different and no TTL pulse is generated by the detector. The

data acquisition software uses the output pulse to reject bad shots thus improving signal-to-noise ratio.

The dye laser is a Lumonics Hyperdye-500 tunable laser which uses a 2400 grooves/mm holographic grating in the oscillator cavity to scan the frequency of the ω_2 beam. The ω_2 beam has a linewidth of 0.03 cm^{-1} with output energies of the order of 10 mJ/pulse, depending on the type of dye being used. The ω_2 beam is steered around the laser table by two prisms and focused into the molecular beam chamber along with the two ω_1 beams in a folded BOXCARS geometry shown in Figure 3.3. This arrangement is used because it is a convenient method for separating the anti-Stokes beam from the other three beams. For complete details of the alignment procedure refer to reference 28.

The anti-Stokes signal is generated at the sample point which is the region in space where the ω_1 and ω_2 beams overlap. The probing area is approximately a cylinder of about 0.1 mm diameter and 1-3 mm length, corresponding to a volume of $\sim 10^{-11}$ m^3. The anti-Stokes beam is spatially filtered from the other beams and a holographic filter is used to block out any scattered 532 nm light. Additional colored filters are used to block out scattered light from the dye laser.

The ω_3 beam is steered into a McPherson single grating monochromator by two mirrors. The photons are detected by an RCA 31034 photomultiplier tube. The output is processed by a Stanford Research Systems SR 250 gated integrator. The integrated signal is digitized with a Scientific Solutions Lab Master A/D converter. Data

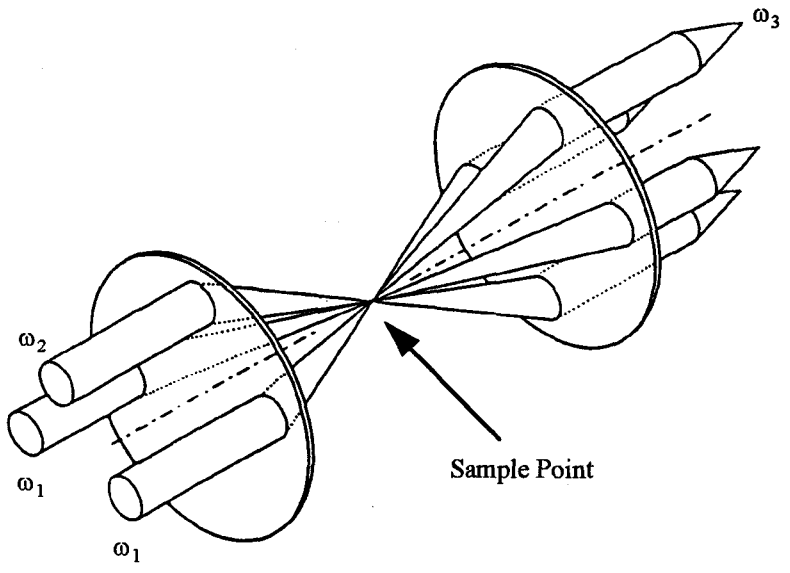

Figure 3.3 The folded BOXCARS arrangement used to achieve phase matching.

acquisition and dye laser control are achieved through interface with a microcomputer using software written by M. Orlov.

Because the frequency of the ω_2 beam shifts due to dye concentration, age, and temperature, a method is required to calibrate all data. The simplest procedure is to use the monomer Q-branch to determine the absolute Raman shift. This method is quite reliable due to the fact that the Q-branch is usually well defined while the cluster peaks are all broad. A high resolution scan of the monomer in a static cell at ~5 Torr is taken at the beginning and the end of the day to determine if there was any drift. The spectrum is then compared to the literature to establish the dye laser offset.

3.2 Jet Samples

Clusters are formed by expanding high pressure gas inside the molecular beam chamber shown in figure 3.4. The pressure inside the chamber is ~0.2 Torr when the nozzle is closed and ~1 Torr when the nozzle is opened. The background pressure, P_b, determines the position of the Mach disk; the region where the gas reheats due to collisions with the background gas. The position of the Mach disk is given by[30]

$$X/D = 0.67\sqrt{\frac{P_0}{P_b}} \tag{3.1}$$

where P_0 is the initial pressure. In a typical experiment, where P_0 = 15 atm, the Mach disk is at X/D = 160 whereas the region being studied never exceeds X/D = 40.

It is also desirable to keep the background pressure as low as possible to minimize the heat load on the nozzle. If P_b is too high, then the warm background gas will heat the nozzle and the dewar assembly through collisions. This effect is especially important when studying molecules with low boiling points such as N_2 (77 K), O_2 (90 K) and H_2 (20 K). In such cases, we would like to be able to cool the nozzle as much as possible.

The laser beams enter the chamber through the side windows which are held at Brewster's angle to minimize reflections. The nozzle used for the expansions is a modified Bosch fuel injector and is held inside the chamber by a dewar assembly. A shim is welded on the tip of the fuel injector to reduce the size of the nozzle. Inside the fuel injector is a plunger, spring and a solenoid. When a voltage is applied to the solenoid, a

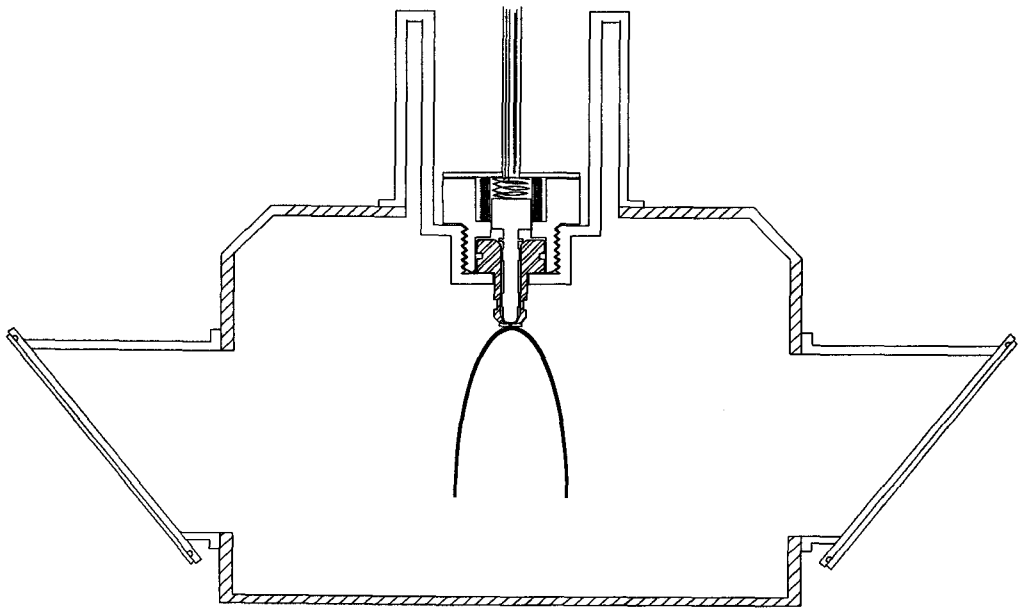

Figure 3.4 Diagram of the molecular beam chamber used to generate and study the clusters. Clusters are produced by pulsing high pressure gas into the evacuated chamber.

magnetic field is formed which pulls the plunger up and opens the nozzle. Once the voltage is discontinued, the spring pushes the plunger down and closes the nozzle. The solenoid is driven by a pulse driver which was constructed at OSU and is typically set at 200 V. The nozzle opening is synchronized with the laser pulses by a Hewlett-Packard 222A pulse generator.

A thermocouple is located just above the solenoid to measure the temperature of the nozzle. The thermocouple readout is an Omega HH-51 digital meter. The temperature of the nozzle increases over time from the heat generated by the solenoid. Therefore it is necessary to flow air over the fuel injector to keep it at room temperature.

There are times when it is necessary to cool the nozzle to increase the formation of clusters. In such cases, cold air is blown into the dewar assembly to cool the nozzle below room temperature. The air is cooled by passing it through liquid nitrogen. This method has yielded nozzle temperatures as low as 160 K.

3.3 Bulk Samples

The bulk samples are studied with the aid of an APD Cryogenics HC-4MK1 cryostat shown in figure 3.5. A minimum pressure of 10^{-3} Torr is required for the operation of the cryostat. In this setup, a roughing pump and a diffusion pump are used to attain pressures of 10^{-6} Torr. Just as in the molecular beam chamber, the laser beams enter the cryostat through side mounted windows held at Brewster's angle.

The sample is introduced into the cryogenic cell which is shown in Figure 3.6. This cell consists of a thin copper body with quartz windows on both sides. Indium gaskets are used to achieve a vacuum seal. O-rings cannot be used because they freeze and become brittle at low temperatures. The cell is first evacuated and then the sample is introduced through a thin stainless steel tube. The temperature of the cell is controlled by a Lakeshore 330 Autotuning Temperature Controller. Crystals are produced by lowering the temperature of the sample to just above the melting point. The sample is then cooled at a rate of 0.5 K/hour. This slow cooling allows the crystal to anneal uniformly. Once the crystal is formed, the temperature is lowered to 15 K. Scans are taken from low temperatures to high temperatures at a constant interval.

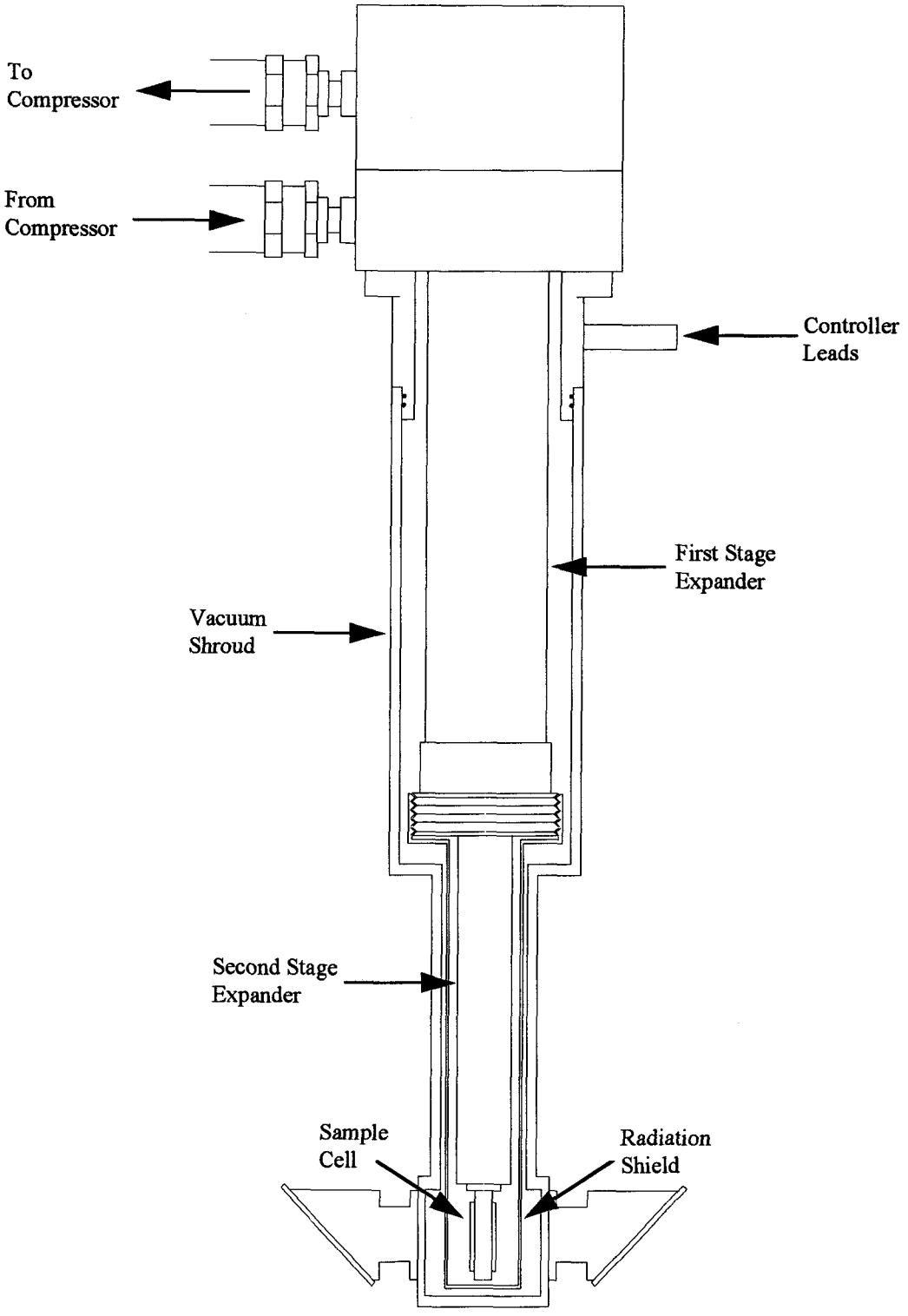

Figure 3.5 Diagram of the cryogenic stack used to prepare bulk samples.

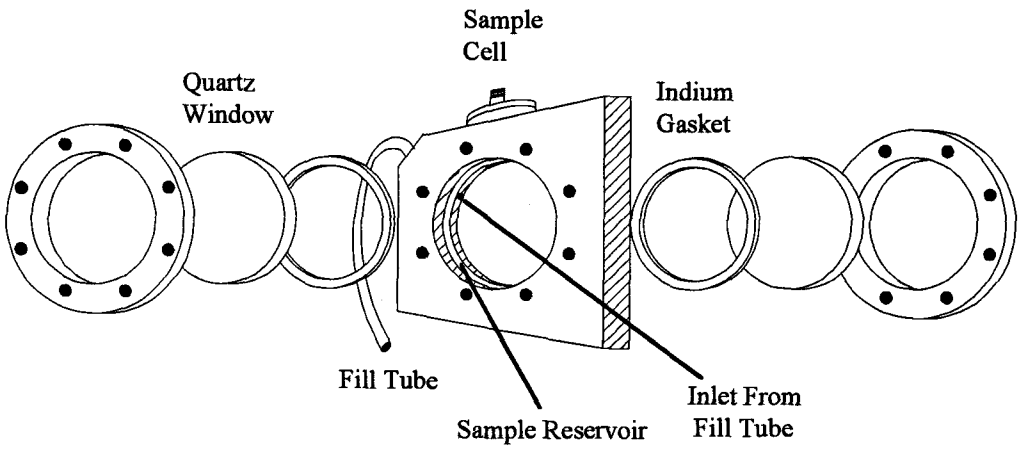

Figure 3.6 Diagram of the cryogenic sample cell. The gaseous sample is introduced into the copper cell through the fill tube.

The high power of the laser beams raises two concerns in taking spectra of samples in a cryostat. The first concern is burning a hole through the quartz windows and the second concern is thermal decomposition of the samples. Both of these concerns are addressed by overlapping the beams 1-2 cm prior to or after the focus. One can also reduce the intensity of the beams by placing neutral density filters in front of the sample cell. Both methods lead to a reduction in signal intensity which is compensated by increasing the photomultiplier voltage.

4. MOLECULAR THEORY OF INTERFACIAL TENSION

The first attempt at deriving an *ab initio* model for interfacial tension was made by Laplace in 1806.[5] With certain approximations, he was able to express the liquid-vapor interfacial tension in terms of the intermolecular forces. Laplace's work was followed up by Maxwell[51] and later by Fowler,[52] Buff,[53] and Kirkwood.[54] In 1949, Kirkwood used the mechanical definition of interfacial tension, with the aid of statistical mechanics, to calculate the liquid-vapor interfacial tension of liquid argon.

Soon thereafter, researchers began to examine the nature of the liquid-liquid and solid-liquid interface. In 1960, Ono and Kondo used thermodynamic arguments to describe the liquid-liquid interface.[55] In the late 1970's, Navascués and Berry made an attempt at deriving an expression for the solid-fluid interfacial tension using the mechanical and thermodynamic definition.[56] As we shall see later, the presence of a solid presents certain difficulties in the modeling of the interface.

The purpose of this chapter is to present the theory of interfacial tension for the liquid-vapor interface. We will begin by deriving an expression for σ_{lv} using the mechanical definition of interfacial tension (1.7). The mechanical definition is used instead of the thermodynamic definition because it is a more direct approach to a molecular theory. The theory will then be tested by calculating σ_{lv} values for several fluids. Finally, we will explore the possibilities of extending the theory to the solid-vapor and solid-liquid interface.

4.1 The Pressure Tensor

Pressure is defined as force per unit area and is most commonly thought of as a scalar quantity. However, it can be shown that pressure is neither a scalar quantity nor a vector, but rather a tensor.[57] The pressure tensor **P** can be written as

$$\mathbf{P} = \begin{bmatrix} P_{xx} & P_{xy} & P_{xz} \\ P_{yx} & P_{yy} & P_{yz} \\ P_{zx} & P_{zy} & P_{zz} \end{bmatrix} \tag{4.1}$$

For a non-flowing system at equilibrium, the non-diagonal components, commonly referred to as the shear components, are zero and **P** reduces to

$$\mathbf{P} = \begin{bmatrix} P_{xx} & 0 & 0 \\ 0 & P_{yy} & 0 \\ 0 & 0 & P_{zz} \end{bmatrix} \tag{4.2}$$

where at equilibrium, $P_{xx} = P_{yy} = P_{zz}$. In the interface region, however, the tangential components (P_{xx} and P_{yy}) are not equal to the normal component (P_{zz}) due to the interfacial tension (see Section 1.1.2). Thus, in order to use (1.7) to calculate σ_{lv}, we must first obtain an expression for the tangential and normal components of the pressure tensor. Irving and Kirkwood have derived such an expression by calculating the stress transmitted across a differential area within the fluid.[58] It is not our intention to derive in detail these expressions but rather to present the arguments used by Irving and Kirkwood in their derivation of **P**.

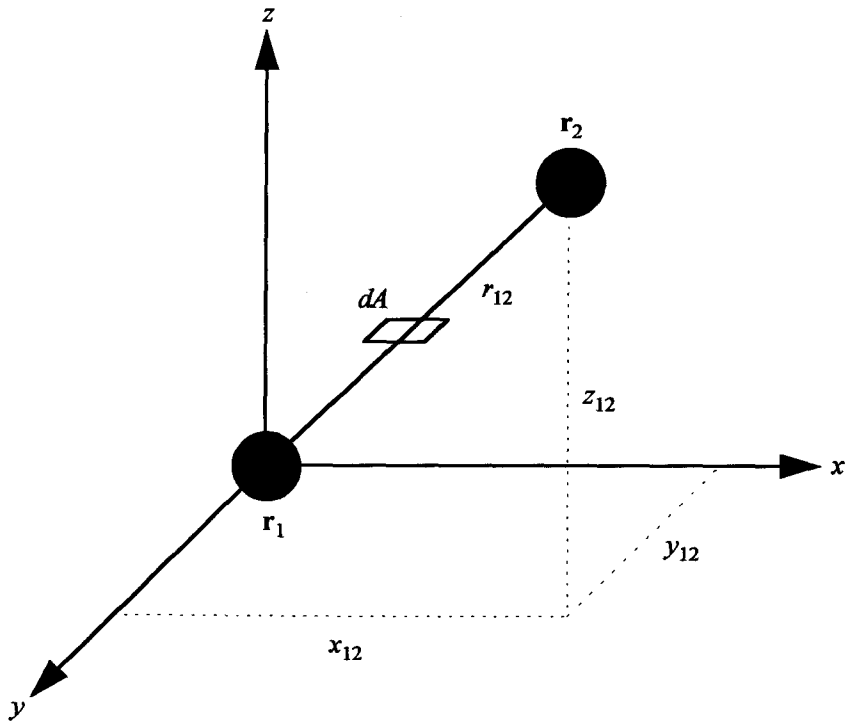

Figure 4.1 The stress across a surface element as a result of intermolecular forces.

Figure 4.1 shows a surface element *dA* within a fluid (no interface yet). According to Irving and Kirkwood, the stress across *dA* is comprised of a kinetic term due to the momentum of the molecules and a potential term due to the intermolecular forces. The kinetic term is isotropic, and according to classical statistical mechanics, is given by $k_B T\rho(\mathbf{r})$, where $\rho(\mathbf{r})$ is the density.

The potential term is governed by the intermolecular forces which contribute to the stress across *dA*. In this case, Irving and Kirkwood chose only those forces between pairs of molecules at $\mathbf{r}_1$ in the region below *dA* and at $\mathbf{r}_2$ in the region above *dA*, for which the vector $\mathbf{r}_{12} = \mathbf{r}_2 - \mathbf{r}_1$ passes through *dA*. The molecule at $\mathbf{r}_1$ experiences a force

$(\mathbf{r}_{12}/r_{12})u'(r_{12})$ from the molecule at $\mathbf{r}_2$, where $u'(r_{12})$ is the derivative of the intermolecular potential with respect to r_{12}. The probability that there is one molecule at $\mathbf{r}_1$ and another at $\mathbf{r}_2$ is proportional to the pair distribution function $\rho^{(2)}(\mathbf{r}_1,\mathbf{r}_2)$. Hence, the pressure tensor is

$$\mathbf{P}(\mathbf{r}) = k_B T\rho(\mathbf{r}) - \frac{1}{2}\int d\tau_{12}\,\frac{\mathbf{r}_{12}\,\mathbf{r}_{12}}{r_{12}}u'(r_{12})\,\rho^{(2)}(\mathbf{r}_1,\mathbf{r}_2) \tag{4.3}$$

where $d\tau_{12}$ is a volume element. The normal component of $\mathbf{P}$ is given by $\mathbf{e}_z\bullet\mathbf{P}(\mathbf{r})\bullet\mathbf{e}_z$, where $\mathbf{e}_z$ is the unit vector in the z-direction. Thus, $P_N(z)$ reduces to

$$P_N(z) = k_B T\rho(z) - \frac{1}{2}\int d\tau_{12}\,\frac{z_{12}^2}{r_{12}}u'(r_{12})\,\rho^{(2)}(r_{12},z_1,z_2) \tag{4.4}$$

Similarly, the transverse components are

$$P_{xx}(z) = k_B T\rho(z) - \frac{1}{2}\int d\tau_{12}\,\frac{x_{12}^2}{r_{12}}u'(r_{12})\,\rho^{(2)}(r_{12},z_1,z_2) \tag{4.5}$$

$$P_{yy}(z) = k_B T\rho(z) - \frac{1}{2}\int d\tau_{12}\,\frac{y_{12}^2}{r_{12}}u'(r_{12})\,\rho^{(2)}(r_{12},z_1,z_2) \tag{4.6}$$

For a planar interface, the density is cylindrically symmetric around the z-axis and $P_{xx}(z)$ is equal to $P_{yy}(z)$. Therefore, the tangential component of $\mathbf{P}$ is equal to $(P_{xx}(z) + P_{yy}(z))/2$ and may be written as

$$P_T(z) = k_B T\rho(z) - \frac{1}{4}\int d\tau_{12}\,\frac{x_{12}^2 + y_{12}^2}{r_{12}}\,u'(r_{12})\,\rho^{(2)}(r_{12}, z_1, z_2) \quad (4.7)$$

Additionally, Buff[53] and Harasima[59] have shown that $dP_N(z)/dz$ is equal to zero, a condition required for mechanical stability.

4.2 The Liquid-Vapor Interface

Having obtained an expression for the pressure tensor, we are now ready to derive an expression for σ_{lv}. Substituting (4.4) and (4.7) into the mechanical definition (1.7), we find that the isotropic parts of the pressure tensor cancel and we obtain

$$\sigma_{lv} = \frac{1}{4}\int_{-\infty}^{\infty} dz_1 \int d\tau_{12}\left(\frac{r_{12}^2 - 3z_{12}^2}{r_{12}}\right)u'(r_{12})\,\rho^{(2)}(r_{12}, z_1, z_2) \quad (4.8)$$

In order to integrate (4.8), we need an expression for the pair distribution function. Unfortunately, there is no exact expression for the distribution function and we start with the simplest approximation, namely a sharp liquid surface. In other words, $\rho(z)$ is a constant on the liquid side ($z \geq 0$) given by ρ_l and zero in the gaseous region ($z < 0$). We approximate $\rho^{(2)}$ in the liquid phase by

$$\rho^{(2)}(r_{12}, z_1, z_2) = \rho_l^2\, g(r_{12}) \quad (4.9)$$

where $g(r_{12})$ is the radial distribution function of a homogeneous liquid which can be determined from experiment or theory. Substitution of (4.9) into (4.8) and changing to cylindrical coordinates, where $d\tau_{12} = 2\pi\, dz_{12}\, r_{12}\, dr_{12}$ yields

$$\sigma_{lv} = \frac{\pi}{2}\rho_l^2 \int_0^\infty dr_{12} \iint_{-\infty}^{\infty} dz_1\, dz_{12} \left(r_{12}^2 - 3z_{12}^2\right) u'(r_{12})\, g(r_{12}) \qquad (4.10)$$

Before integrating (4.10), we must adjust the limits of integration over z_1 and z_{12} due to the density constraints imposed by the sharp interface conditions. To simplify the problem, we will momentarily ignore the integration over r_{12} and write the z-dependent integrals as

$$\int_{-\infty}^{\infty} dz_1 \int_{-\infty}^{\infty} f(z_{12})\, dz_{12} \qquad (4.11)$$

where $f(z_{12}) = (r_{12}^2 - 3z_{12}^2)$. As Figure 4.2 shows, the molecules are restricted to the liquid side of the interface. Therefore, $z_1 \geq 0$ and (4.11) becomes

$$\int_0^{\infty} dz_1 \int_{-\infty}^{\infty} f(z_{12})\, dz_{12} \qquad (4.12)$$

Furthermore, the relation $r_{12} = (x_{12}^2 + y_{12}^2 + z_{12}^2)^{1/2}$ shows that $r_{12} \geq z_{12} \geq -r_{12}$. Thus, the limits over z_{12} are $\pm r_{12}$ so that the integral is

$$\int_0^{\infty} dz_1 \int_{-r_{12}}^{r_{12}} f(z_{12})\, dz_{12} \qquad (4.12)$$

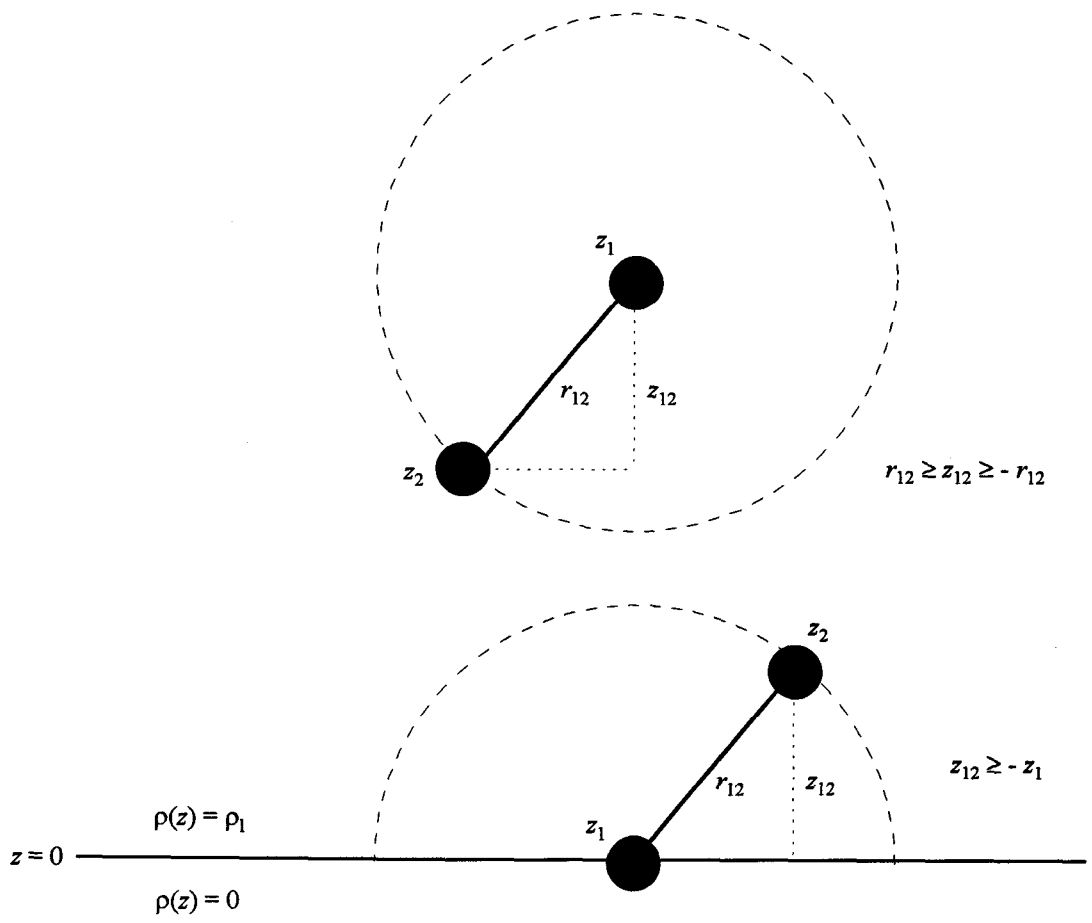

Figure 4.2 Effects of density constraints on the limits of integration of (4.10). The solid circles represent the molecules at z_1 and z_2 while the long dashes indicate the possible positions of z_2 with respect to z_1. The density in the gaseous region ($z < 0$) is equal to zero while the density in the liquid region ($z \geq 0$) is ρ_l. As a result, both z_1 and z_2 must be on the liquid side of the interface.

which can be rewritten as

$$\int_0^{r_{12}} dz_1 \int_{-r_{12}}^{r_{12}} f(z_{12})\,dz_{12} + \int_{r_{12}}^{\infty} dz_1 \int_{-r_{12}}^{r_{12}} f(z_{12})\,dz_{12} \qquad (4.13)$$

According to Figure 4.2, if the molecule at z_1 is within a distance r_{12} of the interface, then $z_{12} \geq -z_1$. This requirement is necessary to ensure that the molecule at z_2 will also be on the liquid side of the interface. Consequently, the limit of integration over z_{12} in the case where $r_{12} \geq z_1 \geq 0$ is

$$\int_0^{r_{12}} dz_1 \int_{-z_1}^{r_{12}} f(z_{12})\,dz_{12} + \int_{r_{12}}^{\infty} dz_1 \int_{-r_{12}}^{r_{12}} f(z_{12})\,dz_{12} \qquad (4.14)$$

Evaluation of the integrals in (4.14) shows that the second term vanishes while the first term is equal to $r_{12}^4/4$. As a result, (4.10) reduces to the single integral

$$\sigma_{lv} = \frac{\pi}{8}\rho_l^2 \int_0^{\infty} r^4\, u'(r)\, g(r)\, dr \qquad (4.15)$$

where the subscript '12' has been omitted for simplicity. If the intermolecular potential and the radial distribution function are known, (4.15) can be used to calculate the liquid-vapor interfacial tension. This expression was also derived by Navascués[60] using the thermodynamic definition of interfacial tension, showing that a system in thermodynamic equilibrium is also in mechanical equilibrium. If we make the assumption that the liquid is homogeneous at the molecular scale, then we can substitute $g(r) = 1$ into (4.15). Integration by parts gives

$$\sigma_{lv} = -\frac{\pi}{2}\rho_l^2 \int_0^\infty r^3 u(r)\, dr \tag{4.16}$$

which is the equation derived by Laplace in 1806. Having obtained an expression for interfacial tension in terms of molecular properties, we are now ready to calculate σ_{lv}.

4.3 The Hard-Sphere Model

As a first approximation in solving (4.15) for the liquid-vapor interfacial tension, we chose to use the hard-sphere intermolecular potential where the molecules are treated as infinitely hard "billiard balls." The hard-sphere potential has a steep repulsive part with no attractive part and is given by

$$u(r) = \begin{cases} 0 & r \geq d_{hs} \\ \infty & r < d_{hs} \end{cases} \tag{4.17}$$

where d_{hs} is the hard-sphere diameter and is given by the sum of the radii of the two colliding molecules. This potential is hardly an accurate representation of the intermolecular forces, but it greatly simplifies the calculations and is a good starting point for the calculation of σ_{lv}.

For a hard-sphere potential, $u'(r)$ is equal to zero everywhere except at $r = d_{hs}$ where it is a delta function. Thus, (4.15) becomes

$$\sigma_{lv} = -\frac{\pi}{8}\rho_l^2 k_B T \int_0^\infty r^4 \delta(r - d_{hs})\, g(r)\, dr \tag{4.18}$$

where the potential $u(r)$ was divided by $k_B T$ so that we would be differentiating and integrating a unitless function. Also note that $u'(r)$ is negative for a hard-sphere potential as is indicated by (4.18). To illustrate this point, consider a less repulsive potential such as $u(r) = 1/r^{50}$. It is clear that the derivative of this function is negative. Integrating (4.18), we get for a hard-sphere

$$\sigma_{lv} = -\frac{\pi}{8} k_B T \rho_l^2 d_{hs}^4 g(d_{hs}) \tag{4.19}$$

where $g(d_{hs})$ is the value of $g(r)$ at contact, which according to the Carnahan-Starling[57] equation of state for hard spheres is

$$g(d_{hs}) = \frac{1 - \frac{1}{2}\rho^*}{(1-\rho^*)^3} \tag{4.20}$$

and ρ^* is the packing fraction which is given by $\rho^* = \pi \rho d_{hs}^3/6$, where ρ is the bulk number density. Inserting (4.20) into (4.19) and converting densities into packing fractions gives

$$\sigma_{lv} = -\frac{9}{2\pi} \frac{k_B T}{d_{hs}^2} (\rho_l^*)^2 \frac{1 - \frac{1}{2}\rho_l^*}{(1-\rho_l^*)^3} \tag{4.21}$$

It is interesting that using a repulsive potential, such as the hard-sphere potential, gives σ_{lv} values that are negative. Recall that in Chapter 1 we described the interfacial tension

as an attractive force which prevents the surface from extending. It is no surprise then that using a potential with no attractive forces results in a σ_{lv} value of the wrong sign.

4.4 The Lennard-Jones Model

Since interfacial tension is an attractive force, it is necessary for us to use an intermolecular potential that resembles these forces. Thus, in this section we will use a Lennard-Jones 6-12 potential to calculate σ_{lv}. This potential is given by

$$u(r) = 4\varepsilon\left[\left(\frac{d}{r}\right)^{12} - \left(\frac{d}{r}\right)^{6}\right] \tag{4.22}$$

where ε is the potential well depth and d is the distance at which $u(r) = 0$ (Figure 4.3). The r^{-12} term in (4.22) accounts for the short-range repulsive forces while the r^{-6} term simulates the long-range attractive forces. Although the Lennard-Jones potential is a more realistic potential than the hard-sphere potential, it is still not a very accurate representation of intermolecular interactions, even for rare-gas atoms.

Moreover, solving (4.15) using a Lennard-Jones potential brings about several difficulties. First, there is no analytical expression for the radial distribution function which means that (4.15) must be solved numerically. Second, and more importantly, finding the radial distribution function for a Lennard-Jones liquid is not trivial. Here we make use of existing perturbation theories to approximate the Lennard-Jones $g(r)$.

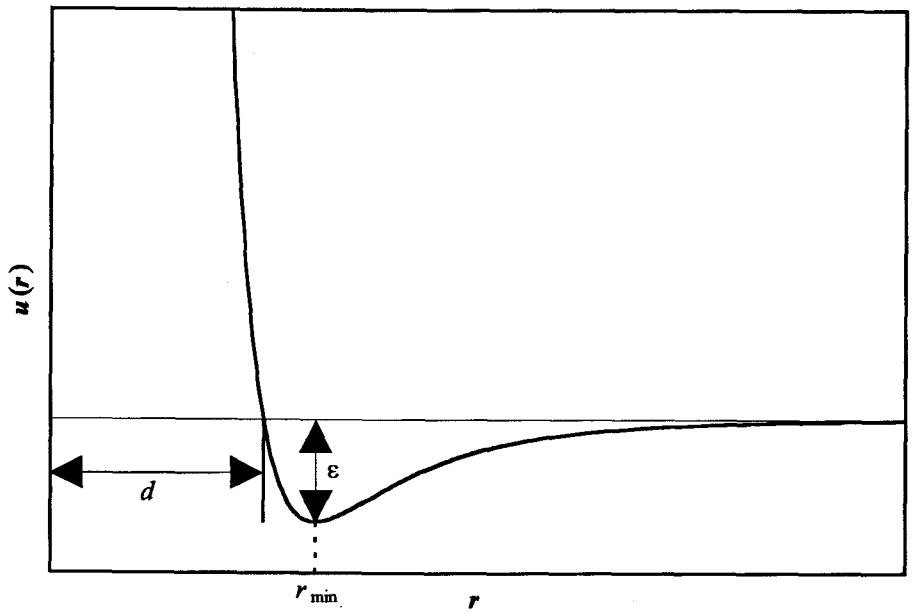

Figure 4.3 A typical Lennard-Jones 6-12 intermolecular potential.

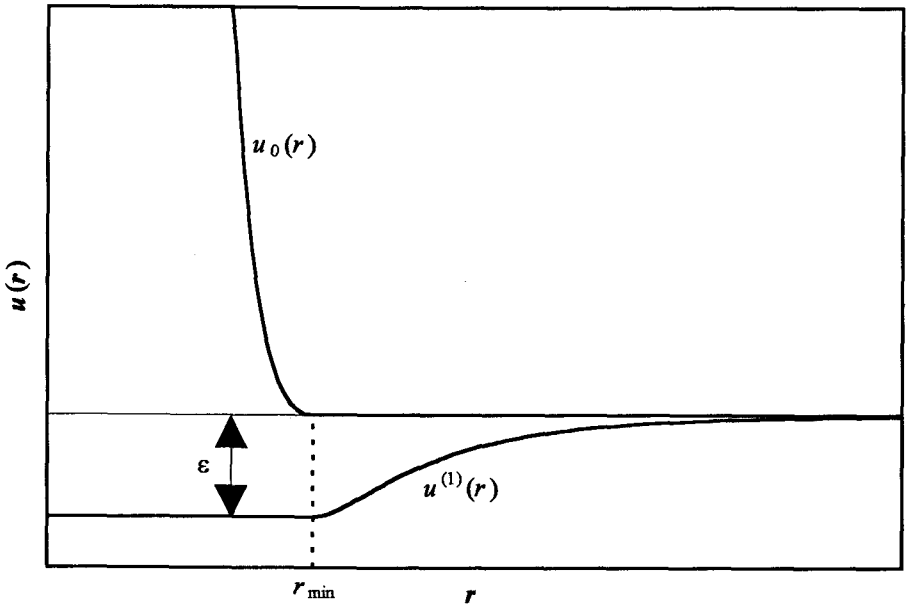

Figure 4.4 The CWA separation of a Lennard-Jones potential into a repulsive part and an attractive part.

4.4.1 Lennard-Jones $g(r)$

Thus far, we have mentioned the significance of $g(r)$ in the development of the theory but have neglected to give a formal definition of $g(r)$. Simply put, $g(r)$ describes the structure of a liquid in terms of density. In other words, the local density $\rho(r)$ about some fixed molecule is given by

$$\rho(r) = \rho\, g(r) \tag{4.23}$$

where ρ is the bulk density of the liquid. The radial distribution function is extremely important in the theory of liquids for it can be shown that all the thermodynamic functions of a system can be written in terms of $g(r)$.[57]

The only way to determine the exact $g(r)$ for a system is to use X-ray or neutron diffraction data. However, various theoretical methods exist in which one can find an accurate, but not exact, $g(r)$. One such method is the Chandler-Weeks-Andersen (CWA) perturbation theory of liquids which was developed in 1971.[61] We will not discuss the details of this theory here but rather its application to our problem.

In CWA theory, the intermolecular potential is separated into a part which contains the repulsive forces and a part which contains the attractive forces (Figure 4.4). Therefore,

$$u(r) = u_0(r) + u^{(1)}(r) \tag{4.24}$$

where for a Lennard-Jones 6-12 potential

$$u_0(r) = \begin{cases} u(r) + \varepsilon & r < r_{min} \\ 0 & r \geq r_{min} \end{cases} \tag{4.25a}$$

$$u^{(1)}(r) = \begin{cases} -\varepsilon & r < r_{min} \\ u(r) & r \geq r_{min} \end{cases} \tag{4.25b}$$

According to CWA theory, $g(r)$ for a Lennard-Jones liquid is then given by

$$g(r) = g_{hs}(r) \exp\left[\frac{-u_0(r)}{k_B T}\right] \tag{4.26}$$

where $g_{hs}(r)$ is the radial distribution function of a fluid of hard spheres. The radial distribution function can be calculated from molecular dynamics simulations or computer programs which numerically solve one of the many available integral equations for $g(r)$.[57,62] The program which we have used to calculate $g_{hs}(r)$ is described in great detail in Appendix B. Figure 4.5 shows the calculated hard-sphere $g_{hs}(r)$ for a typical liquid at several different densities. Our program does not calculate $g_{hs}(r)$ inside the hard core ($r/d < 1$), forcing us to extrapolate the calculated $g_{hs}(r)$ into this region using a second order polynomial.

Figure 4.6 shows the experimental and calculated radial distribution function for methane at 92 K. The maxima at $r = d$, $2d$, etc. are due to the shells of first nearest neighbors, second nearest neighbors, etc. surrounding the central molecule. This indicates that liquids have short range order. Note that the value of $g \rightarrow 0$ as $r \rightarrow 0$ due to the intermolecular repulsion at $r < d$. On the other hand, $g \rightarrow 1$ as $r \rightarrow \infty$ indicating the lack of long range order in liquids. The calculated Lennard-Jones $g(r)$ is in

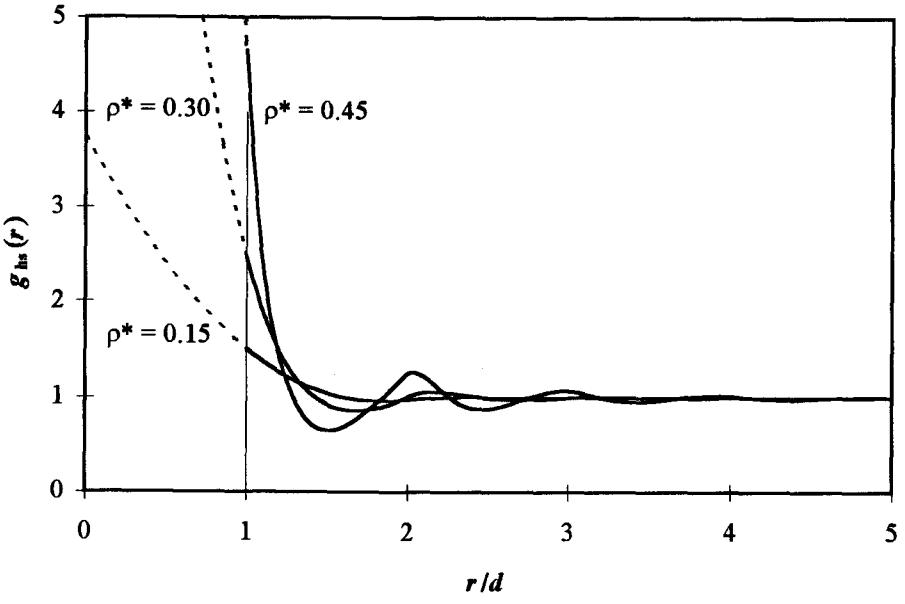

Figure 4.5 The radial distribution function of a hard-sphere calculated for different liquid densities. The dashed lines represent a second-order polynomial extrapolation into the hard core region.

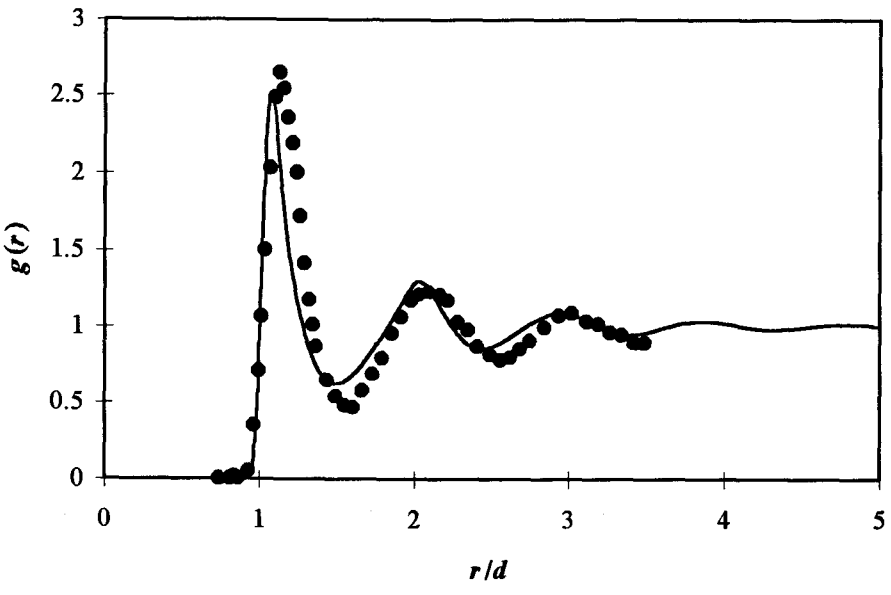

Figure 4.6 The radial distribution function for methane at 92 K ($\rho^* = 0.46$) calculated using CWA theory and a Lennard-Jones potential. The dots are from X-ray diffraction studies of reference 63.

satisfactory agreement with the experimental $g(r)$ for liquid methane deduced from X-ray diffraction studies.[63]

4.4.2 Interfacial Tension of a Lennard-Jones Fluid

Having demonstrated the capability to calculate the $g(r)$ for a Lennard-Jones system, we can now venture to calculate the interfacial tension. Before attempting to calculate the surface tension of supercooled liquids, it is prudent to determine how accurate our model is by calculating the liquid-vapor interfacial tension of several common fluids in the normal liquid range. The systems chosen for this test were Ar, Kr, N_2, O_2, and CH_4. These systems are attractive because accurate thermodynamic data and Lennard-Jones parameters are readily available. Table 4.1 lists the results obtained by using our model and treating each system as a Lennard-Jones fluid.

The results show that at low temperatures, where we are far away from the critical point, our model is in excellent agreement with experimental values. For example, for Ar at 90 K, we obtain a σ_{lv} value of 12.3 mJ/m^2 compared to the experimental value of 11.9 mJ/m^2. In 1949, Kirkwood calculated the interfacial tension of liquid argon at 90 K to be 14.9 mJ/m^2 using (4.15).[54] At the time, there were no methods available to calculate $g(r)$ and as a result, Kirkwood used thermodynamic data to approximate $g(r)$. Our results are presumably better because we used a more accurate $g(r)$. Using Laplace's equation (4.16), where $g(r) = 1$ everywhere, we arrive at a much poorer value of 22.1 mJ/m^2. It is clear then that given the same potential, the relative success of the theory is dependent on the exact form of the distribution function.

Table 4.1 Calculated and experimental σ_{lv} values for several fluids. The normal range of liquid existence and the Lennard-Jones potential parameters[a] are also listed for each fluid. Experimental σ_{lv} values and thermodynamic data are from reference 25.

Liquid	d (Å)	ε (K)	T (K)	$\sigma_{lv,\,exp}$ (mJ/m^2)	$\sigma_{lv,\,calc}$ (mJ/m^2)	T / T_c
Ar			84	13.1	13.2	0.56
(84-87 K)	3.405	117.2	90	11.9	12.3	0.60
			125	3.9	8.7	0.83
Kr			116	16.3	16.2	0.55
(116-120 K)	3.634	163.1	125	14.5	15.1	0.60
			135	12.4	14.2	0.64
N_2			70	10.5	10.9	0.56
(63-77 K)	3.636	101.6	80	8.3	9.6	0.63
			90	6.2	8.6	0.71
O_2			70	18.3	18.1	0.45
(55-90 K)	3.386	122.3	80	15.7	16.1	0.52
			90	13.2	14.4	0.58
CH_4			91	17.1	16.2	0.47
(91-111 K)	3.743	149.1	100	15.1	14.6	0.52
			110	13.1	13.3	0.58
CO_2			221	16.5	16.9	0.73
(217 K)[b]	3.762	245.3	241	11.3	16.1	0.79
			262	6.8	15.1	0.86
H_2O			273	75.6	84.5	0.42
(273-373 K)	2.71	506	373	58.9	70.9	0.58
			473	37.7	51.5	0.73

[a]Lennard-Jones potential parameters are taken from references 64-66.
[b]Liquid CO_2 does not have a normal range of liquid existence and only the triple point temperature is listed.

It is also interesting to consider the results obtained for CO_2 and H_2O using an approximated Lennard-Jones potential. These molecules can hardly be considered Lennard-Jones fluids, especially H_2O where hydrogen bonding is prevalent. However, the calculated σ_{lv} values for these systems are in reasonable accord with the experimental values, with $\sigma_{lv,calc}$ generally being larger than the experimental results. This goes to show that molecular properties, such as interfacial tension, are primarily dependent on the qualitative features of the potential and that an exact potential is not necessary to obtain satisfactory results.

4.4.3 Density Profile of the Interface

Close inspection of the calculated values in Table 4.1 reveals that although the theory is capable of correctly predicting the temperature dependence of σ_{lv}, the agreement with experimental values begins to deteriorate as the temperature approaches the critical temperature, T_c. This is shown graphically for liquid methane in Figure 4.7. The reason that the theory fails quantitatively at higher temperatures is because the interface becomes more diffuse and the density of two phases begin to approach each other up to the critical point, where the two phases are indistinguishable. Therefore, our approximation of the density profile as a step function is no longer valid.

A better, and more realistic, description of the density profile of the interface at high temperatures is to use an exponential approximation such as that shown in Figure 4.8. Berry has used such an approximation, along with the assumption that the interface thickness is of the order of 3 d, to calculate σ_{lv} for liquid methane at several different

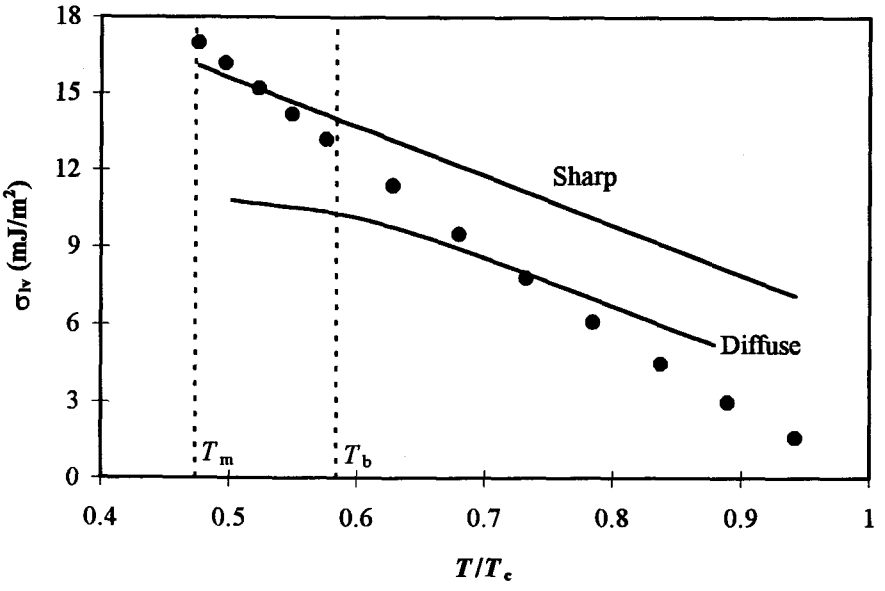

Figure 4.7 Calculated σ_{lv} values for liquid methane assuming a step function. Also shown are the values calculated by Berry assuming a diffuse interface with an interface thickness of *d*. The solid dots are experimental values.

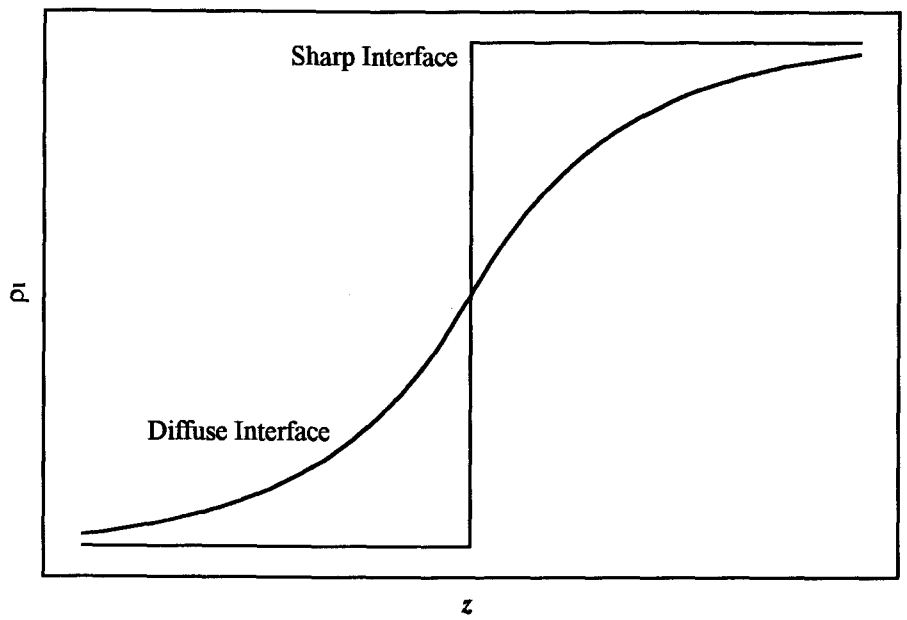

Figure 4.8 Density profiles for a sharp and diffuse interface.

temperatures.[56] His results are shown in Figure 4.7. Notice that Berry's values are in much better agreement with the experimental data at higher temperatures. However, the agreement at low temperatures is no longer satisfactory. The reason for this is that the thickness of the interface is dependent on the temperature of the liquid and as a result, the density profile of the interface varies as a function of temperature.

Further calculations have shown that the interface thickness, which is on the order of d near the triple point, increases rapidly with temperature and reaches a value of 5 d near the critical point. Since the density changes continuously over the interface as one passes from the liquid state to the gas, it becomes obvious that the approximation of a sharp interface is only valid near the triple point. Fortunately, we are interested in the surface tension of liquids in the supercooled region where it is plausible to estimate the density profile as a step function.

4.4.4 Surface Tension of Supercooled Liquids

There is virtually no information regarding the surface tension of liquids in the supercooled regime. It is common practice to estimate σ_{lv} in the supercooled region by extrapolating existing experimental values for the normal liquid range. However, it is not clear whether such an extrapolation is justifiable. Here, we will use the developed theory to calculate the surface tension of several supercooled liquids and compare the results to the extrapolated values. The liquids chosen for this calculation are methane, argon, and nitrogen, all of which can be approximated as Lennard-Jones fluids. These

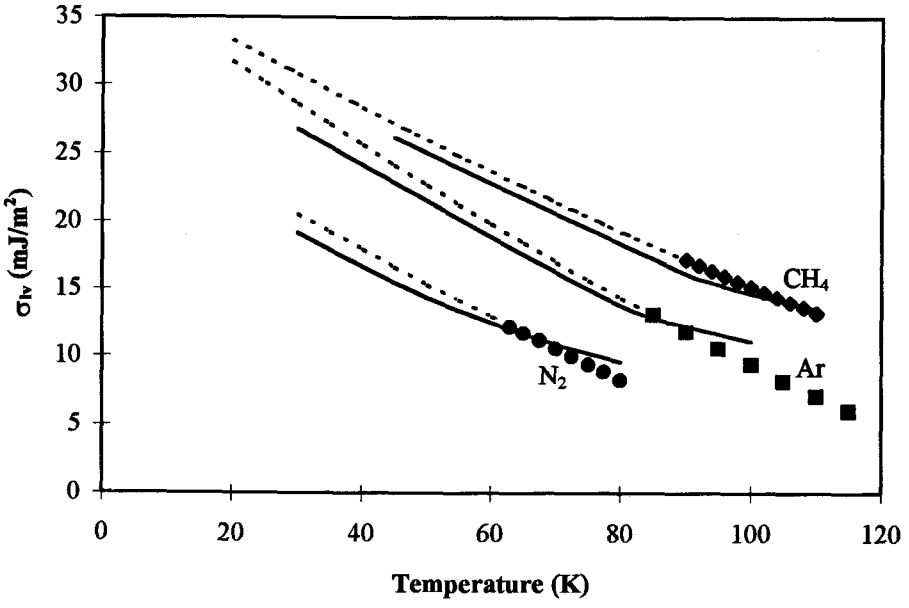

Figure 4.9 Experimental, extrapolated, and theoretical σ_{lv} values for methane, argon and nitrogen. The points are experimentally determined values while the dashed lines are an extrapolation into the supercooled region. The solid lines are the theoretical values.

systems are also attractive in that there exists accurate Lennard-Jones intermolecular potential parameters and a wealth of thermodynamic data required for the calculations.

Figure 4.9 shows a plot of the experimental, extrapolated, and calculated surface tension values for methane, argon, and nitrogen. The data points correspond to the experimental values in the normal liquid range, while the dashed line is an extrapolation into the supercooled region. The solid line is obtained from theory and is in good agreement with the extrapolated σ_{lv} values. The theory indicates that, at least for some molecules, extrapolation of surface tension values into the supercooled region is justified.

Note that the theoretical values in the supercooled region are lower than the extrapolated values in all cases. The main reason for this is that we are only considering

two body forces and are neglecting higher order interactions. Certainly, the majority of forces acting on a molecule will be due to nearest neighbor interactions. However, second and third nearest neighbor interactions are significant and should not be ignored. The net effect of these higher order interactions is to increase the attractive forces which would result in larger surface tension values.

4.5 The Solid Interface

One might consider if the theory developed for the liquid-vapor interface could be applicable in the case of a solid-vapor interface. Using (4.15) and the discrete $g(r)$ for a solid face centered cubic crystal, we have calculated σ_{sv} for solid nitrous oxide and carbon dioxide. Although the results are reasonable for nitrous oxide, the σ_{sv} values calculated for carbon dioxide are in fact negative. Thus, it appears that the theory, in its current form, does not yield satisfactory results for solid surfaces.

A possible reason for the failure of the theory in the case of a solid may be the presence of shear forces in a solid,[67] which means that the off diagonal elements of the pressure tensor (4.1) are no longer equal to zero. Moreover, according to Shuttleworth, the shear components vary depending on the crystal face.[67] Another problem could be the shape of the potential well, which is expected to be different than that of liquids. We have explored this and found that a small change in the value of d or ε determines whether the σ_{sv} value is positive or negative. Moreover, broadening of the discrete $g(r)$ function by Gaussians to emulate thermal motions in a solid gave results which were quite sensitive to the widths chosen for the Gaussian functions. Therefore, to estimate

values for σ_{sv} and σ_{sl}, we must resort to other semiempirical methods which will be discussed in the following sections.

4.5.1 Young's Equation

When a liquid drop is placed on a flat solid surface, the final shape of the drop depends on the relative magnitude of the cohesive forces that exist within the liquid and the adhesive forces between the liquid and solid. The equilibrium configuration is typically described by the contact angle, θ, which is the angle formed between the liquid and solid surface (Figure 4.10). Generally, liquids with a low interfacial tension tend to spread over the solid giving a zero contact angle while liquids with a high interfacial tension give a finite contact angle.

In 1805, Young considered the forces that exist at the three phase equilibrium shown in Figure 4.10.[68] He argued that the mechanical stability of the contact region is a result of the balance of the interfacial forces acting on the three phase contact line. Thus, he proposed that

$$\sigma_{sv} = \sigma_{sl} + \sigma_{lv} \cos\theta \tag{4.27}$$

Young's equation has been criticized by many authors over the past century due to the vague arguments Young used in his approach. However, Gibbs,[69] Johnson,[70] and Neumann[5] have independently carried out a rigorous derivation of (4.27) and concluded

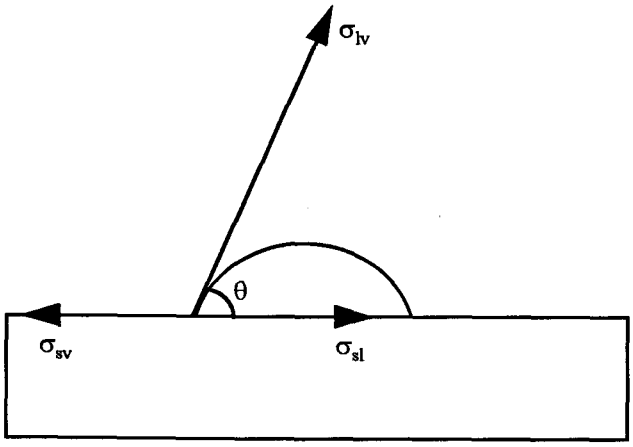

Figure 4.10 Vector diagram of the forces acting across the liquid-vapor, solid-vapor and solid-liquid interface.

that the equation is valid and that it also holds for zero contact angle in which case (4.27) reduces to

$$\sigma_{sv} = \sigma_{sl} + \sigma_{lv} \tag{4.28}$$

The contact angle is expected to be zero in cases where the liquid and solid are the same material. This is due to the fact that the cohesive forces within the liquid are balanced out by the adhesive forces between the liquid and solid surface.

Experimental verification of (4.28) is provided by Bailey and Kay, who in 1967 used the cleavage technique discussed in Section 1.3 to measure σ_{sv} and σ_{sl} for mica in an atmosphere of vapor and then in the corresponding liquid.[27] They then used (4.28) to deduce σ_{lv} for the liquid. Their data is presented in Table 4.2 with the last column

Table 4.2 Solid-fluid interfacial tension for mica/fluid systems. (all values in mJ/m^2)

Fluid	σ_{sv}	σ_{sl}	$\sigma_{sv} - \sigma_{sl}$	σ_{lv}
Water	182.8	107.3	75.5	72.8
Hexane	271	255	16	18.4

representing the experimental σ_{lv} values. The good agreement between the experimental and calculated σ_{lv} values is considered satisfactory justification of (4.28). Therefore, if two of the three interfacial tensions are known, then the third can be calculated from (4.28).

4.5.2 Semiempirical Models for the Solid-Liquid Interface

Due to lack of experimental data regarding the solid-vapor interface, there is no method available for estimating the value of σ_{sv}. There is, however, limited data available for the solid-liquid interface and several methods have been proposed to obtain estimates for σ_{sl}. These models include a purely energetic model by Zadumkin,[71] an entropic model by Ewing,[72] and a lattice model by Jackson.[73] With the evolution of faster computers, molecular dynamics and Monte Carlo calculations have also become a popular method for determining the interfacial tension.[5,74-75]

One method of estimating σ_{sl} came about as a result of Turnbull's famous experiments with liquid metals. In 1950, Turnbull found an empirical correlation between σ_{sl} and the heat of fusion which is[13]

$$\sigma_{sl} = C\frac{\Delta H_{fus}}{(N_a V^2)^{1/3}} \tag{4.29}$$

where V is the molar volume and C was found empirically to be 0.45 for metallic substances and 0.32 for nonmetallic substances. The variables ΔH_{fus} and V in (4.29) are taken to be the values at the melting point. In the case of carbon tetrachloride, (4.29) yields a σ_{sl} value of 4.6 mJ/m^2 at any temperature, a value which can be compared to Bartell's experimental value of 5.5 mJ/m^2 at 175 K.

Recently, Tegze and coworkers have developed a new method for calculating the solid-liquid interfacial tension as a function of temperature and crystal structure.[31] Their work is based on a broken-bond model which has been modified to take into account the loss of entropy for a liquid in contact with the crystal. They have derived (4.29) and shown that the constant C can be calculated for the crystal packing and temperature and need not be empirically based. Figure 4.11 shows a plot of the temperature dependence of C calculated for various crystal structures. Test calculations show that the model yields values that are in excellent agreement with experimental data. Applying this model to carbon tetrachloride yields a σ_{sl} value of 6.2 mJ/m^2 at 175 K.

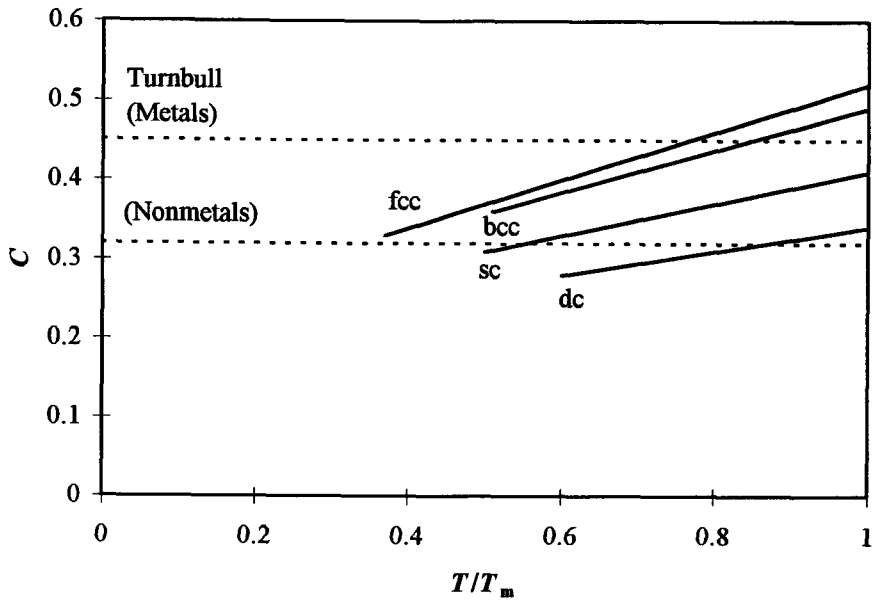

Figure 4.11 Temperature dependence of C for various crystal structures. (fcc = face centered cubic, bcc = body centered cubic, sc = simple cubic, dc = diamond cubic). The dashed lines correspond to the values of C empirically determined by Turnbull for metallic and nonmetallic substances.

5. SURFACE TENSION OF SOLIDS AND SUPERCOOLED LIQUIDS

Over the past decade, the spectral and structural properties of liquid and solid clusters formed in a jet expansion have been of considerable interest in our laboratory.[36-37] In recent years, a special interest has developed in the nucleation kinetics of these clusters.[28] In this chapter we shall examine data from several experiments where the main focus was to use measured rates of nucleation to determine the surface tension of supercooled liquids and solids.

In the previous chapter we showed that it is possible to calculate reasonable values of the surface tension of supercooled liquids from molecular theory. The theoretical results offered justification for the extrapolation of surface tension values in the normal liquid range into the supercooled regime. To take the analysis one step further, in this chapter we discuss a method we have devised which, with the aid of nucleation theory, allows us to obtain an experimental measurement of the surface tension of supercooled liquids. In the following sections, we shall discuss the results obtained for several molecular systems. The final section of this chapter is devoted to a similar application of nucleation theory in determining the surface tension of solids.

5.1 Liquid Methane

Methane is the simplest hydrocarbon and was the first molecule chosen for study due to the large amount of thermodynamic and physical data available for it. In order to study the surface tension as a function of temperature, several mixes and stagnation

conditions were used to produce liquid methane clusters from the supersaturated vapor. Figure 5.1 shows a plot of the calculated isentropes for three such expansion conditions. These conditions were chosen such that the isentropes would cross the coexistence curve well above the triple point, thereby favoring initial formation of liquid, not solid, clusters.

5.1.1 Determination of Nucleation Rates

As previously described in Section 2.3.2, the variables required to determine the nucleation rate are the number of critical nuclei N formed in the time span Δt in a given volume V. The volume is simply the laser focal volume which is estimated to be about 10^{-11} m^3. However, we will see shortly that it is not necessary to have an explicit value of V in order to determine the nucleation rate.

The variables Δt and N are deduced from the CARS spectrum and the isentropic expansion relations (2.3)-(2.6). Although we cannot measure the exact time span in which nucleation occurs, we are able to set an upper limit to the value of Δt based on the X/D position at which clusters are first observed. For example, Figure 5.2 shows that in a neat expansion, liquid clusters are present at X/D = 0.8. However, no clusters are detected at X/D = 0.5. Therefore, nucleation must have taken place between these two points and Δt is the time is takes for the gas to travel this distance. Since the beam velocity from (2.6) is 630 m/s and D = 0.25 mm, Δt in this case is 120 ns.

Determination of N is somewhat more complex because, unlike clusters, we cannot detect critical nuclei. However, if we assume that each cluster is a result of a single nucleation event, then the number of clusters (N_c) is equal to the number of critical

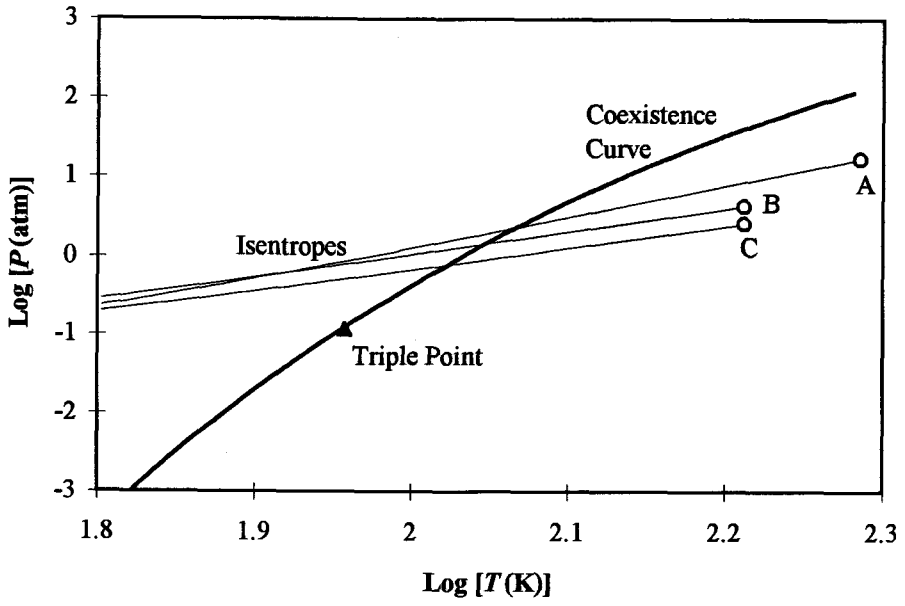

Figure 5.1 Calculated isentropes for expansions of methane. A: Neat (P_0 = 17 atm, T_0 = 193 K). B: 25% mix (P_0 = 17 atm, T_0 = 163 K). C: 15% mix (P_0 = 17 atm, T_0 = 163 K).

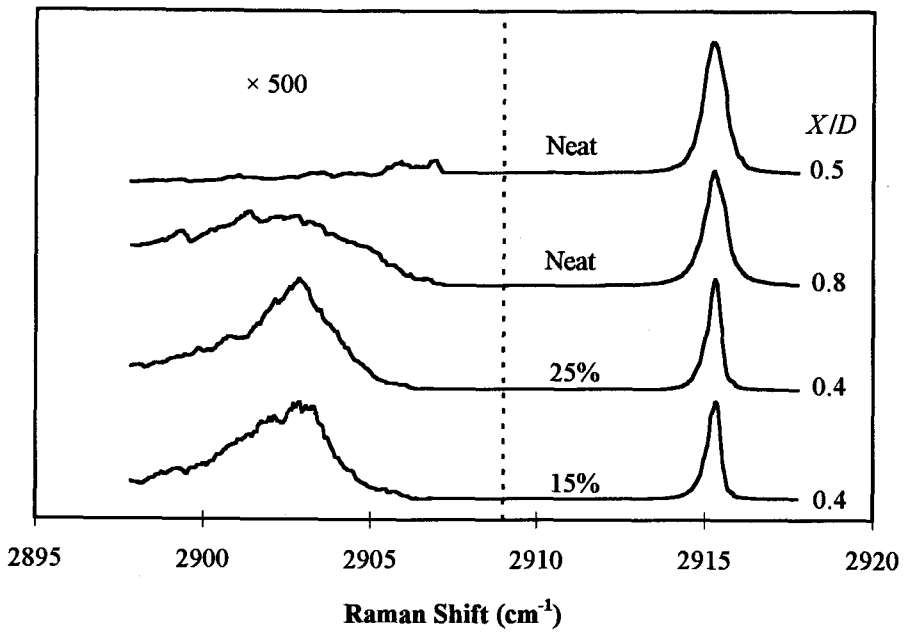

Figure 5.2 CARS spectra of methane clusters at *X/D* positions where clusters are first observed. The intensity of the cluster peak is expanded by a factor of 500.

nuclei formed. Based on Minarik's calculations, this is a reasonable assumption considering that, on the average, there is less than one cluster-cluster collision per *X/D* unit.[28] In other words, once clusters form, only a small fraction coalesce while the rest grow rapidly as a result of the addition of monomers and not cluster-cluster collisions.

Since the intensity of the cluster and monomer peaks observed in the CARS spectrum is a function of the number of molecules squared, it possible to estimate the number of clusters using (2.23), which states that the number of observed monomers (N_M) plus the number of monomers in cluster form ($N_C M_C$) is equal to the total number of monomers (N_{Total}) predicted by (2.5). The area of the monomer and clusters peaks in a plot of $(I_{CARS})^{1/2}$ yields the ratio $Z = N_M/N_C M_C$ which reduces (2.23) to

$$N_{Total} = (Z+1) N_C M_C \tag{5.1}$$

However, since the volume is constant and (2.5) yields the isentropic number *density*, we can divide both sides of (5.1) by V to get

$$N^*_{Total} = (Z+1) N^*_C M_C \tag{5.2}$$

where the asterisk indicates units of molecules per unit volume. Consequently, we can eliminate V from the rate equation and rewrite (2.22) as

$$J = \frac{N^*}{\Delta t} \tag{5.3}$$

The above analysis shows that if the number of molecules within each cluster (M_C) is known, then one can use (5.2) to calculate N_C* which can then be used to determine J from (5.3).

Table 5.1 lists the parameters required to calculate N_C* for expansions of methane. In our analysis, M_C is calculated from the mean cluster size, which is deduced from the cooling curve model described in Section 2.4.1. The fitting procedure, which will be discussed in greater detail in Chapter 6, yields cluster sizes of 15 nm and 8 nm for the neat and 25% mix expansions, respectively. These results are in accord with other data which indicate that clusters produced in jet expansions are typically in the range of 5-25 nm corresponding to 10^4-10^6 molecules per cluster.[38,42] The data for the 15% mix study is incomplete and as a result, we cannot use cooling curves to determine the size. However, we expect the 15% and 25% clusters to be of comparable size due to the similarities between the two experiments.

Using the data in Table 5.1, we find that there are 10^{19}-10^{20} clusters (or critical nuclei) per cubic meter, depending on the experimental conditions. Notice that there are more clusters in the mix expansions where the extent of clustering is greater due to colder temperatures. This is reflected in the observed values of Z which is a function of the expansion conditions and decreases as the extent of clustering increases

Having successfully obtained reasonable estimates for N* and Δt, we can now use (5.3) to calculate the nucleation rate. Table 5.1 shows that J is of the order of 10^{26}-10^{27} m^{-3} s^{-1}, depending on the expansion conditions. The rates for the mix expansions are slightly higher because the gas is colder, resulting in a lower energy

Table 5.1 Data for several expansions of methane for a jet with $D = 0.25$ mm.[a] The # sign indicates number of molecules. Values in parentheses have been estimated.

	Neat	25% Mix	15% Mix
P_0 (atm)	17	17	17
T_0 (K)	193	163	163
T_S (K)	128	118	110
X/D	0.8	0.4	0.4
Mach Number	2.4	1.7	1.7
T (K)	(88)	(78)	(70)
υ (m/s)	633	699	764
Δt (ns)	118	107	98
P_v (atm)	0.73	0.51	0.25
P_{eq} (atm)	8.2×10^{-2}	1.8×10^{-2}	3.9×10^{-3}
υ_m (m^3)	5.9×10^{-29}	5.7×10^{-29}	5.6×10^{-29}
N^*_{Total} (#/m^3)	8.2×10^{25}	6.5×10^{25}	4.0×10^{25}
Z	11.8	6.3	6.5
R_C (nm)	15	8	(8)
M_C (#)	2.5×10^5	3.7×10^4	3.7×10^4
N^*_C (#/m^3)	2.6×10^{19}	2.4×10^{20}	1.4×10^{20}
J (m^{-3} s^{-1})	2.2×10^{26}	2.3×10^{27}	1.5×10^{27}
r^* (Å)	6.4	5.2	4.7
n^* (#)	25	15	12
σ_{lv} (mJ/m^2)	14.4	16.5	17.2
$\sigma_{lv,\infty}$ (mJ/m^2)	17.4	20.6	21.9

[a]Thermodynamic data have been taken from references 25, 76, and 77.

barrier for the formation of critical nuclei. These rates are comparable to those estimated for the condensation of benzene ($\sim 10^{25}$ m^{-3} s^{-1}) in a free jet expansion.[19]

It is difficult to determine the error associated with our nucleation rates because we know very little about the uncertainties of N^* and Δt. The major source of error in the calculation of N^* is due to N^*_{Total} which is a function of the X/D position at which clusters are first observed. The reason for this error is that we are unable to accurately measure absolute X/D positions due to the poorly defined location at which $X/D = 0$. Typically, we take the origin of the expansion to be the position where the tip of the nozzle crosses the midpoint of the laser beam (see Figure 5.3). Experiments by Mayer,[38] however, suggest that the expansion begins inside the tip of the nozzle and thus, the measured X/D values are too small by as much as one X/D unit. As a result, the calculated value of N^*_{Total}, and hence N^*, could be too large by as much as a factor of four.

Additionally, we expect N^* will be smaller than our estimate if appreciable coalescence of small clusters occurs. However, as stated earlier, the number of cluster-cluster collisions is small and the probability that two colliding clusters will coalesce may also be small. Another concern in the calculation of N^* is the use of a single mean cluster size, rather than a distribution of sizes, which typically has a width of about 25% of the mean. Based on Mayer's experiments,[38] however, we are confident that the cooling curve model predicts the cluster radius to within a factor of about two and, overall, we believe N^* is accurate to within an order of magnitude.

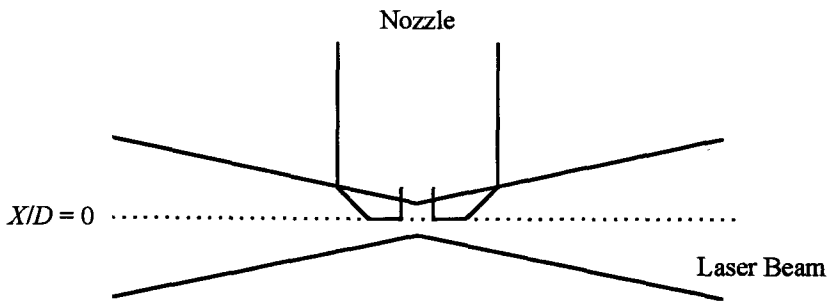

Figure 5.3 Our choice for the origin of the expansion ($X/D = 0$).

The error associated with Δt is somewhat more difficult to ascertain and is governed by the spatial resolution of the experimental apparatus. Using a typical nozzle diameter of 300 μm and a beam waist of 100 μm, we find that our spatial resolution is limited to 0.3 X/D units. Therefore, while nucleation may take place within a narrower X/D range, we are only able to set an upper limit to the value of Δt. Note that the error associated with our X/D measurements do not apply here since we are measuring relative, and not absolute, positions.

Since the formation and growth of clusters is governed by collision rates, we can estimate the time it takes to form a nucleus of a given size from gas kinetic theory. Using the data in Table 5.1 for the neat expansion, we find that there are approximately 30 collisions per nanosecond. Thus, if all collisions resulted in coalescence, a nucleus of 25 molecules could be formed in about 0.8 ns. However, only a fraction of the colliding molecules stick to each other and many more collisions are needed. Using a sticking fraction of 0.1 (based on the cooling curve model described in Section 2.4.1), the time required to form the nucleus would be about 8 ns.

Additionally, as the molecules stick to each other, the nucleus warms up due to the heat of condensation. This energy must be carried away by further collisions from the colder background gas or else the nucleus will break apart. We can estimate this number from the following simple model.

The total amount of energy released during condensation is equal to the number of molecules in the nucleus times the heat of vaporization per molecule. The amount of energy removed per non-sticking collision is equal to $C_{p,g}\,\Delta T_g$ where ΔT_g is the change in the temperature of the gas. If we assume that all of the heat released during condensation is carried away by the background gas, then the number of collisions is given by

$$n_{\text{collisions}} = \frac{n^* \Delta H_{\text{vap}}}{C_{p,g}\,\Delta T_g} \tag{5.4}$$

Beck has determined that in neat expansions of nitrogen, the rotational temperature of the gas increases by about 10 K during condensation.[37] Therefore, using a ΔH_{vap} of 8506 J/mole for methane at 100 K and a $C_{p,g}$ value of 35.6 J/mole K,[76] we find that 600 collisions are needed to remove this thermal energy. This corresponds to an additional 20 ns, thus, increasing the total time required to form a nucleus to about 28 ns.

Wegener has recently estimated the time needed to achieve nucleation to be of the order of 10-100 ns.[78] His results, along with our above estimate, show that our measured value of Δt is of the right order of magnitude. Based on the approximated errors for N^* and Δt, we are confident that our nucleation rates are accurate to within

two orders of magnitude. For methane, this means that the calculated surface tension values will have an error of about ±6 % associated with them.

It may be noted that our nucleation rates are comparable to those observed in other free jet expansion and shock tube experiments, but are 10-15 orders of magnitude higher than those observable in cloud chambers or diffusion chambers.[79] This difference is due to the much greater extent of supercooling achieved in free jets (up to 100 K) compared to chamber methods (up to 20 K). The greater supercooling lowers the energy barrier for the formation of an embryo and leads to the extremely high nucleation rates observed in free jets.

5.1.2 Nucleation Temperature

Before we undertake the task of calculating surface tension values from our measured nucleation rates, we must determine the local temperature of the monomer at the onset of nucleation. This is an important variable for it strongly influences the equilibrium vapor pressure which in turn affects the supersaturation ratio which governs the nucleation rate and the size of the critical nucleus. Thus, it is paramount that we obtain accurate estimates of this variable.

Due to the non-equilibrium conditions present in free jets, we must distinguish between the various components of temperature; namely the electronic, vibrational, rotational, and translational temperatures. The contribution from the electronic and vibrational components can be ignored since at room temperature, only the ground

electronic state is populated and a majority of the molecules are also in their ground vibrational state.

At room temperature, many rotational levels are populated and the molecules have a large velocity distribution. Upon cooling in a jet, the rotational temperature will drop considerably as the population of the higher levels decreases. This effect is even more pronounced for the translational component as the velocity distribution narrows.

Since nucleation occurs in the high density region of the jet where there are many collisions, we expect the rotational and translational temperatures of the monomer to be comparable due to nearly equilibrium conditions. This is consistent with Beck's results for expansions of nitrogen where the translational and rotational temperatures were both found to be about 50 K near the onset of condensation.[37] Further out in the jet, the translational temperature was found to be about 20 K lower than the rotational temperature.

The simplest way of determining the translational temperature of the monomer is to use (2.3) which yields the temperature as a function of *X/D*. However, as we mentioned in the previous section, the measured *X/D* positions could be off by as much as one *X/D* unit. Consequently, the temperatures obtained from (2.3) may be too high by 20-30 K. This is significant since a 20 K change in the temperature will alter the supersaturation ratio by 3-4 orders of magnitude. Thus, until we have a better method of accurately measuring *X/D* values, we must use alternate means to determine the monomer temperature at the onset of nucleation.

The rotational temperature can be determined from the intensity distribution of the monomer Q-branch rotational lines. At the resolution used in our experiments (~0.05 cm^{-1}), this method is feasible for only a handful of molecules (e.g. nitrogen and oxygen), where the rotational structure is simple and the individual rotational lines are resolvable. In the case of non-spherical molecules, one can also determine the rotational temperature from a pure rotational spectrum, such as the one shown in Figure 5.4 for nitrous oxide. Here the line spacing is large so resolution is not a limiting factor. This spectrum was taken just before the onset of condensation and based on our simulation, we deduce a rotational temperature of about 130 K.

The problem here is that cluster information is obtained from vibrational modes which can be up to 3000 cm^{-1} away from the pure rotational region. Thus, this method is practical only in situations where the gain curve of the dye laser covers a broad range of wavelengths, thus allowing us to obtain, in a single experiment, pure rotational and vibrational spectra without having to change the experimental setup. This is not viable in all our experiments so we consider next an alternate empirical method to estimate our temperatures.

Recently, Koppenwallner and Düker[80,90] have found that the temperature at the onset of nucleation for neat expansions of nitrogen in a free jet at various stagnation conditions is about 35-40 K below the saturation temperature, T_s (the temperature at which the supersaturation ratio is equal to unity). They have determined the temperature by measuring the local pressure in their very large scale jet expansions. This was done

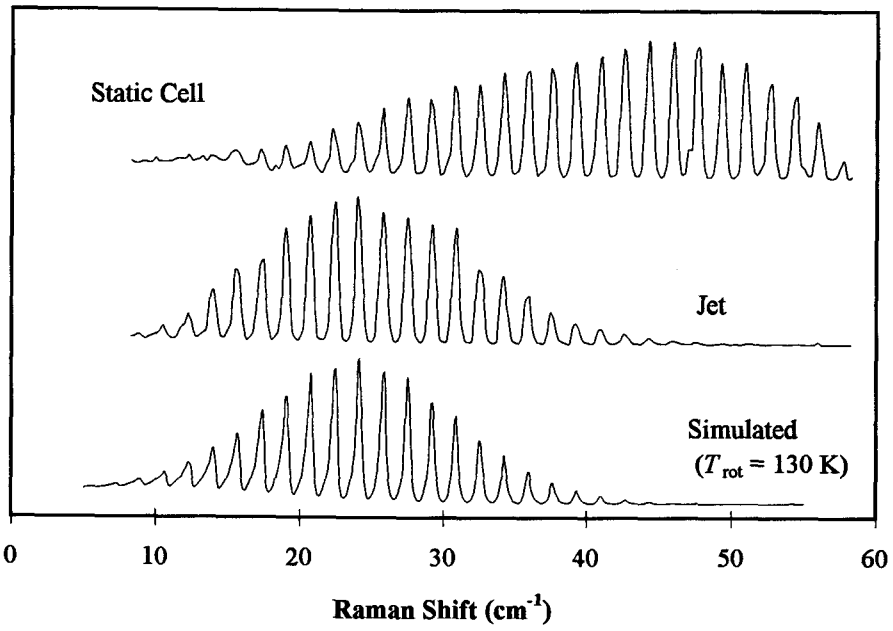

Figure 5.4 Pure rotational CARS spectrum of nitrous oxide. The static cell measurement was taken at 50 Torr. The jet spectrum was taken at the point of condensation for a 30% N_2O/He mixture with P_0 = 10 atm and T_0 = 233 K. The simulated spectrum is obtained by using the rotational constant B = 0.419011 cm^{-1}.[35]

using a Pitot tube to measure the pressure and then, from this and the isentropic relation (2.4), the translational temperature was determined.

Similarly, Williams and Lewis[81] have found that for neat expansions of materials with low boiling points, such as nitrogen (77 K), oxygen (90 K) , argon (87 K), and carbon monoxide (81 K), the temperature at condensation is about 40-45 K below the saturation temperature. These results are in agreement with Beck's data which show the rotational (and translational) temperature of nitrogen to be 52 K at the onset of condensation; about 40 K below the saturation temperature.[37]

Thus, it appears that for neat expansions (in a free jet) of small molecules with low boiling points, there is a correlation between the temperatures at saturation and

condensation. It is not clear whether this correlation holds true in the presence of carrier gas or for molecules with higher boiling points. Studies on the expansion of nitrogen in a cryogenic shock tube[78] show that the difference between T_s and the temperature at condensation is does not change appreciably when the sample is diluted with carrier gas. Also, expansions of steam in Laval nozzles[82] show that a similar correlation exists for water and that it does not change when carrier gas is introduced into the system. Unfortunately, these researchers do not report the degree of supercooling below the saturation temperature.

To determine the magnitude of supercooling below T_s for molecules with higher boiling points, we turn to the pure rotational spectrum of nitrous oxide (185 K) shown in Figure 5.4. The temperature deduced from this spectrum is 60 K below the saturation temperature of 190 K. Additionally, using Brown's carbon dioxide data,[89] we find that the rotational temperature of the gas before the onset of condensation is about 100 K. This is 67 K below the saturation temperature of 167 K. Thus, it appears that at least in the case of nitrous oxide and carbon dioxide, molecules with high boiling points will be supercooled below their saturation temperature by more than 40 K.

In this work, we will be studying argon (87 K), methane (111 K), ethylene (170 K), nitrous oxide (185 K), acetylene (189 K), and carbon dioxide (185 K). Due to lack of better knowledge, we will take the difference between T_s and the temperature at condensation to be 40 K for molecules with low boiling points (e.g. methane and argon) and 60 K for the other molecules with higher boiling points.

5.1.3 Surface Tension & Tolman's Size Relation

With the assumptions discussed above, the experimental nucleation rates were used to calculate the surface tension of liquid methane at several temperatures. The results are shown as the open diamonds in Figure 5.5. The nucleation temperatures are estimated from the empirical relation discussed in the previous section and the lines crossing each data point are used to indicate surface tension values for a temperature range of ±5 K. The vertical error bars show the effect of varying J by a factor of 10^2 and show the weak dependence of σ on J.

Although the results depicted in Figure 5.5 are of the same order of magnitude as the values extrapolated from the normal liquid range, they are considerably lower. This difference can be understood by taking into account the variation of surface tension with drop size, as described by Tolman's relation[83-84]

$$\sigma = \sigma_\infty / (1 + 2\delta / r) \tag{5.5}$$

where σ_∞ is the surface tension of a flat interface, δ is Tolman's length parameter, and r is the radius of the droplet. According to (5.5), the surface tension of a droplet decreases with decreasing radius and, as Figure 5.6 shows, the effect becomes important for very small particles.

The significance of Tolman's relation to our problem is that the surface tension deduced from nucleation rates is that of the critical nucleus, which is a nanometer sized particle. In contrast, the literature values in the normal liquid range, and hence the

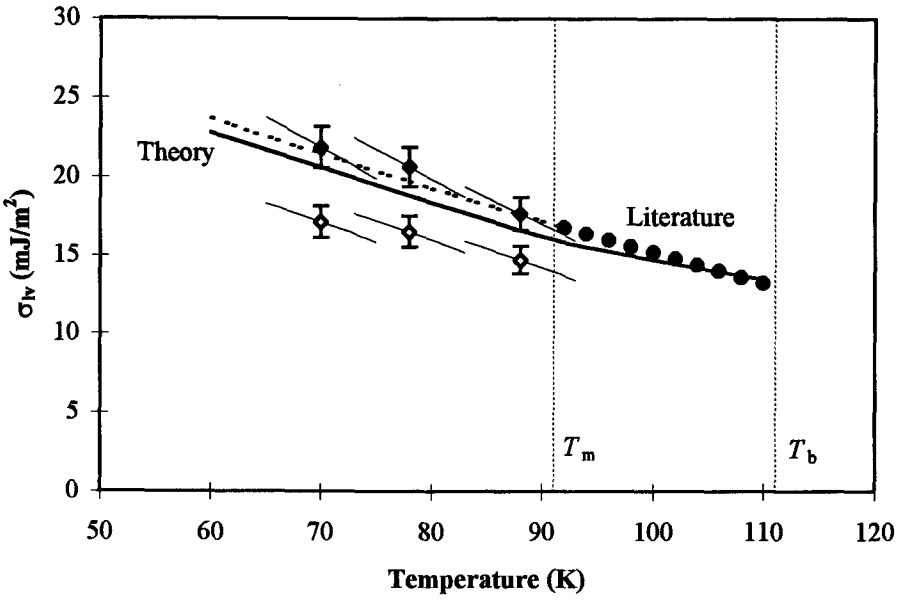

Figure 5.5 The surface tension of liquid methane. The open diamonds are values deduced from nucleation experiments and the solid diamonds are values adjusted to account for size effects. The lines through each data point correspond to a ±5 K temperature range. The vertical error bars correspond to a factor of 10^2 change in J.

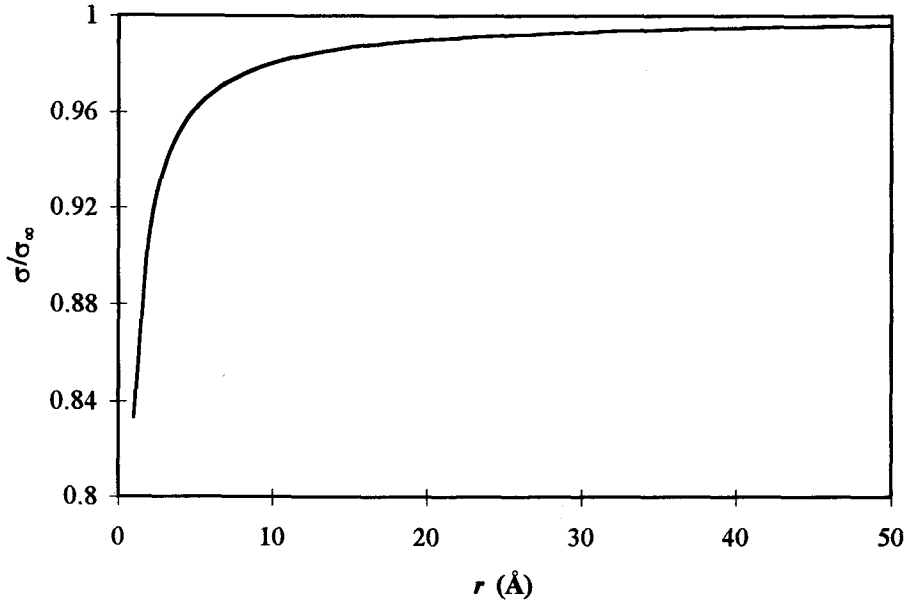

Figure 5.6 Influence of droplet size on the surface tension of a liquid with $\delta = 1$ Å.

extrapolated values, correspond to the surface tension σ_∞ of a flat interface. Thus, in order to make comparisons, the results obtained from nucleation experiments must be adjusted using (5.5).

The difficulty in applying Tolman's relation is that little is known about the parameter δ except that it is of the order of a molecular diameter. Tolman's length is commonly defined as[84]

$$\delta = R_e - R_s \tag{5.6}$$

where R_e is the radius of the equimolar surface and R_s is the radius of the surface of tension. The distinction between these two quantities is illustrated in Figure 5.7. The equimolar surface encompasses a volume $(4/3)\pi R_e^3$ that would contain the entire mass of the droplet if the density were uniform at the surface. Unfortunately, the radius of the droplet is not a well-defined quantity because the liquid-vapor interface is not sharp at a molecular level (see Section 4.4.3). As a result, we introduce an imaginary surface, the surface of tension, which lies inside the equimolar surface and is defined as the distance which gives the correct relation between Δp and σ in Laplace's relation[5]

$$\Delta p = \frac{2\sigma}{R_s} \tag{5.7}$$

where Δp is the pressure difference between two phases separated by a spherical interface. Accordingly, the variable r in (5.5) should be associated with R_s rather than R_e. The significance of this is that the results obtained from nucleation rates correspond

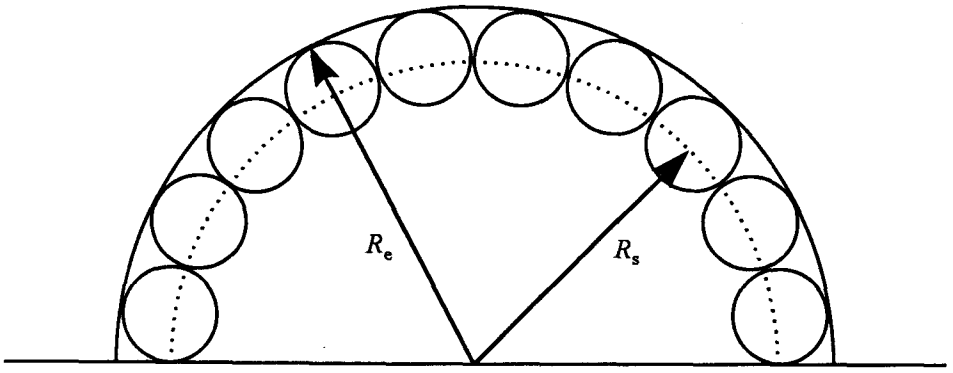

Figure 5.7 The relationship between the equimolar surface and the surface of tension. The small circles represent the individual molecules within the droplet.

to the surface tension of a critical nucleus of radius R_s* (i.e. $r^* = R_s^*$) Therefore, if δ were known, one could use (5.5) to determine the surface tension for a flat interface at the same temperature.

Part of the problem in establishing a reasonable value for δ is the poorly defined quantities R_e and R_s. The problem is further complicated in that there is no information regarding the variation of δ with temperature and droplet size. Nevertheless, theoretical calculations and Monte Carlo simulations have shown that δ is of the order of an angstrom for nanometer sized particles and decreases as the particle size decreases.[54,75] Due to the small size of the critical nuclei in our experiments and lack of better knowledge regarding δ, we will follow Sivier and adopt a value of 0.65 Å.[85]

Using a critical radius given in Table 5.1, we find a δ/r^* ratio of about 0.1 which implies that our experimental values must be multiplied by a factor of 1.2 to represent the surface tension of a flat interface. These 'adjusted' values are depicted by the solid

diamonds shown in Figure 5.5. It is seen that the correspondence between the experimental and extrapolated values is much better after this use of Tolman's relation to correct for size effects. The experimental results are also in pleasing agreement with the theoretical curve calculated using a simple Lennard-Jones potential, as described in Chapter 4. These results further support the notion that the surface tension of a supercooled liquid can be estimated by linear extrapolation of values in the normal liquid range.

5.2 Other Simple Liquids

To determine the extent to which our unique method of measuring surface tension is applicable to molecules other than methane, several other systems, including ethylene and argon were examined. As with the methane experiments, several mixes of each sample were prepared, allowing us to measure nucleation rates at various temperatures. In each case, expansion conditions were chosen to favor the formation of liquid clusters.

5.2.1 *Liquid Ethylene*

Ethylene is an attractive molecule in that it readily forms clusters in a jet expansion at various stagnation conditions. Figure 5.8 shows the isentropes for each expansion condition. The CARS spectrum for the first liquid ethylene clusters produced in each expansion is presented in Figure 5.9. The features are very similar to

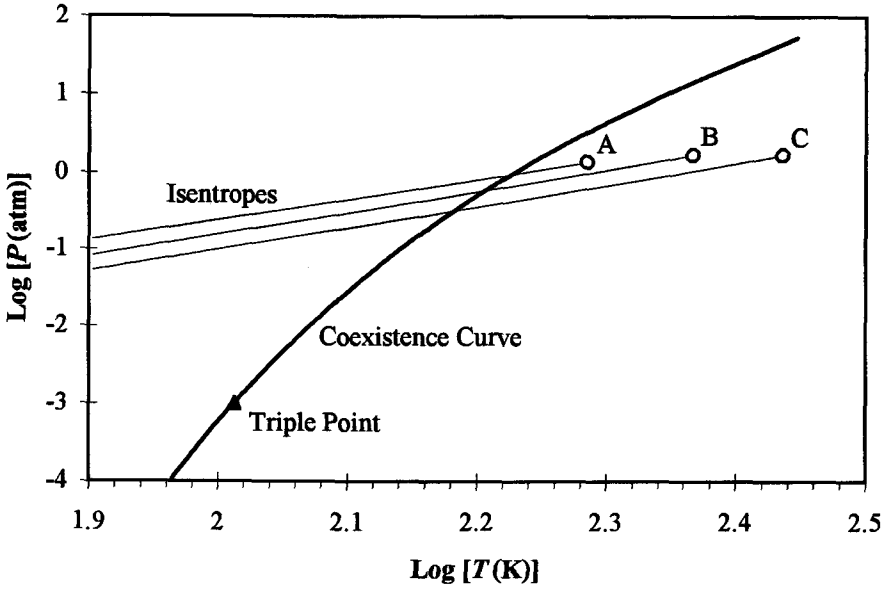

Figure 5.8 Calculated isentropes for expansions of ethylene. A: 10% Mix (P_0 = 13.6 atm, T_0 = 193 K). B: 25% mix (P_0 = 6.8 atm, T_0 = 233 K). C: 25% mix (P_0 = 6.8 atm, T_0 = 273 K)

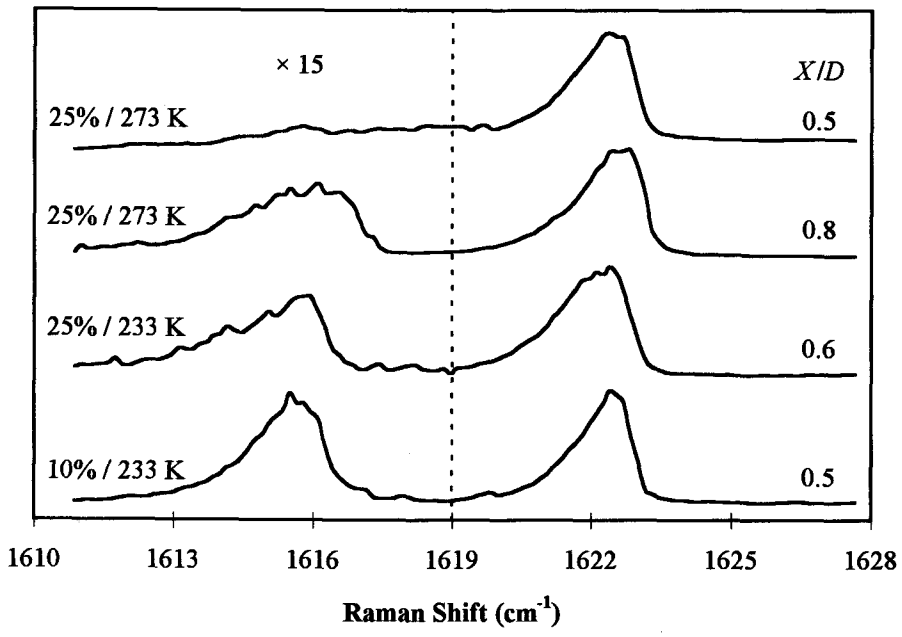

Figure 5.9 CARS spectra of ethylene clusters at *X/D* positions where clusters are first observed. The intensity scale in the cluster region in each spectrum is expanded by a factor of 15.

Table 5.2 Data for several expansions of ethylene for a jet with $D = 0.25$ mm.[a] The # sign indicates number of molecules. Values in parentheses have been estimated.

	25% Mix	25% Mix	10% Mix
P_0 (atm)	6.8	6.8	13.6
T_0 (K)	273	233	233
T_S (K)	148	158	156
X/D	0.8	0.6	1.0
Mach Number	2.4	2.1	1.7
T (K)	(88)	(98)	(96)
υ (m/s)	877	747	868
Δt (ns)	85	100	86
P_v (atm)	4.7×10^{-2}	1.1×10^{-1}	1.2×10^{-1}
P_{eq} (atm)	5.2×10^{-5}	4.3×10^{-4}	2.9×10^{-4}
υ_m (m^3)	6.9×10^{-29}	7.0×10^{-29}	7.0×10^{-29}
N^*_{Total} (#/m^3)	8.4×10^{24}	1.4×10^{25}	1.5×10^{25}
Z	4.0	3.0	2.6
R_C (nm)	(10)	(10)	(6)
M_C (#)	5.9×10^4	5.9×10^4	1.3×10^4
N^*_C (#/m^3)	2.9×10^{19}	6.1×10^{19}	3.2×10^{20}
J (m^{-3} s^{-1})	3.3×10^{26}	6.1×10^{26}	3.7×10^{27}
r^* (Å)	4.1	4.5	4.2
n^* (#)	7	8	7
σ_{lv} (mJ/m^2)	24.7	24.1	24.0
$\sigma_{lv,\infty}$ (mJ/m^2)	32.5	31.0	31.4

[a]Thermodynamic data have been taken from references 25, 76, and 86.

those observed for methane clusters, especially the region in the jet where clusters are initially observed. The major difference between the two systems is that the monomer to cluster ratio, Z, for ethylene is smaller indicating a higher extent of clustering.

The nucleation rates for the various expansions of ethylene were determined by using the same procedure that was used for methane. The results are tabulated in Table 5.2. To deduce the cluster size from the cooling curve model, we considered studying bulk ethylene samples to establish a temperature-frequency relation which could be used to determine the cluster temperatures. However, after careful examination of the cluster data, we concluded that such an effort was not justified since the cluster peaks shift by less than 0.2 cm^{-1} over the entire range of the expansion (8 X/D units). This is to be contrasted with the case of methane, where the cluster peaks shift by more than 1 cm^{-1} within the same X/D range. Furthermore, due to the shape and broad linewidth of the ethylene cluster peak, it was less accurate to assign a single vibrational frequency to represent the peak center. Therefore, cluster temperatures calculated from the bulk data would have a large error leading to a large uncertainty in the size estimate.

A qualitative way of estimating the cluster size is by comparing the expansion conditions to other experiments where the cluster size is known. For example, the results of the previous section show that methane clusters produced in a neat expansion (P_0 = 17 atm) have a radius of 15 nm. Diluting the sample with carrier gas to one-fourth the mole fraction leads to a cluster radius of about 8 nm. Based on these results, and cluster sizes deduced for expansions of nitrogen and carbon dioxide,[37-38,42] we estimate a cluster radius of about 6-10 nm for mix expansions of ethylene.

The open diamonds in Figure 5.10 represent the surface tension of ethylene calculated from the experimental nucleation rates listed in Table 5.2. Once again, these values are significantly lower than the extrapolated values due to size effects discussed previously. The solid diamonds represent the surface tension of a flat interface calculated using Tolman's relation with δ = 0.65 Å. There is excellent agreement between the adjusted values and the extrapolated values and also the theoretical predictions.

The nucleation rates for ethylene are remarkably close to those obtained for methane, in the range of 10^{26}-10^{27} m^{-3} s^{-1} depending on the expansion conditions. As we shall see in Section 5.3.1, these rates are comparable to those measured for nitrous oxide. Similarly, we have used Beck's nitrogen data[37] to estimate a nucleation rate of ~10^{26} m^{-3} s^{-1}. Thus, it appears that nucleation rates observed in a free jet will always fall in a relatively narrow range for clustering to be observed in an expansion. This is due to the fact that the conditions in the expansion do not vary significantly from one molecule to another. Therefore, the variables required to determine J (i.e. N^* and Δt) remain relatively constant.

In fact, a more general conclusion is that the observed nucleation rate is a function of the method used to achieve supersaturation. For example, a review of nucleation experiments from 1968 to 1992 shows that rates observed in diffusion chambers are of the order of 10^{5}-10^{10} m^{-3} s^{-1} while those observed in shock tubes are about 10^{16}-10^{21} m^{-s} s^{-1}.[79] Similarly, nucleation rates for various molecules in a jet expansion are reported to be of the order of 10^{22}-10^{26} m^{-3} s^{-1}. Thus, it appears that

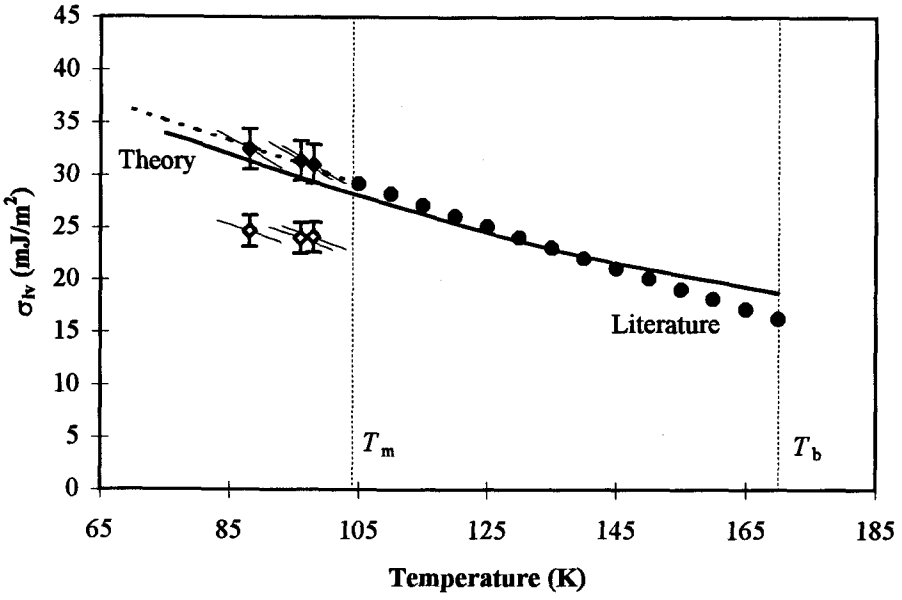

Figure 5.10 The surface tension of liquid ethylene. Theoretical values have been calculated using Lennard-Jones parameters of d = 4.070 Å and ε = 244.3 K from reference 65.

different methods can access only a certain range of nucleation rates. This is mainly a result of the degree of supercooling attainable by each method.

In our experiments, nucleation rates observed for neat expansions are about 10^{26} m^{-3} s^{-1} while those for mix expansions are slightly higher at 10^{27} m^{-3} s^{-1}. Also, our rates tend to be on the high end of the range given above for free jets . This is most likely due to the size, shape, and type of nozzle used along with the experimental conditions.

The significance of this conclusion is that it may not be necessary to accurately determine the nucleation rate. Instead, all that is required in the calculation of surface tension are the conditions (P_0 and T_0) necessary to form clusters. This information can be then used with an assumed J value of 10^{26}-10^{27} to compute σ; a procedure which is

validated by the very weak dependence of σ on J. This hypothesis will be tested in the following section.

5.2.2 Liquid Argon

We have already shown that CARS is a useful tool in studying the formation of clusters along with cluster properties such as structure and phase. However, an alternative and much simpler method of determining the conditions at which clusters form is by Rayleigh scattering. A unique feature of this method is that it allows us to study monatomic species, such as argon, which cannot be probed by any form of rotational-vibrational spectroscopy including CARS.

Detection of clusters by Rayleigh scattering is based on the fact that large particles scatter light more effectively than small particles. As shown in the thesis of S. Mayer,[38] the scattering intensity for N monomers is proportional to N while the vertically polarized (isotropic) intensity (I_{VV}) of a cluster composed of N monomers is proportional to N^2. Thus, the formation of clusters can be readily detected due to a sudden and enormous increase in scattering intensity.

The Rayleigh detector is simply a PMT which is placed outside of the vacuum chamber at 90° to the laser crossing axis . The intense scattering produced in the probing volume is imaged onto the detector with the aid of a lens and aperture system. A polarizer is placed in front of the detector to filter out the depolarized (I_{VH}) light. For a more detailed description of the setup and theory, please refer to S. Mayer's thesis.[38]

Several experiments using Rayleigh scattering were designed to determine the conditions necessary to produce liquid argon clusters. Each experiment was carried out by first positioning the jet at some *X/D* position and maintaining a constant nozzle temperature, T_0. The backing pressure, P_0, was then increased gradually and the scattering signal recorded at various pressure intervals. Due to random fluctuations in the scattering intensity, the signal was averaged over 100 laser shots to enhance *S/N* ratio.

Figure 5.11 shows a plot of the Rayleigh scattering intensity as a function of P_0 at constant *X/D* and T_0. At low pressures, where clusters have not yet formed, the signal is a result of scattering from the monomer and increases linearly as a function of pressure. In the case of a non-condensing jet, we would expect the signal to continue to increase linearly and follow the dashed line. However, Figure 5.11 shows that the scattering intensity begins to increase rapidly at about P_0 = 8.5 atm. This pronounced deviation from linearity is due to the formation of clusters whose scattering intensity is expected to increase quadratically. Therefore, the onset of condensation is designated as the point at which the slope of the signal begins to change.

Table 5.3 lists several expansion conditions under which liquid argon clusters are formed. Figure 5.12 shows the surface tension of supercooled liquid argon calculated from the data presented in Table 5.3. As before, the solid diamonds correspond to adjusted values which represent the surface tension of a flat interface. There is again pleasing agreement between the experimental values and the extrapolated values and theoretical curve..

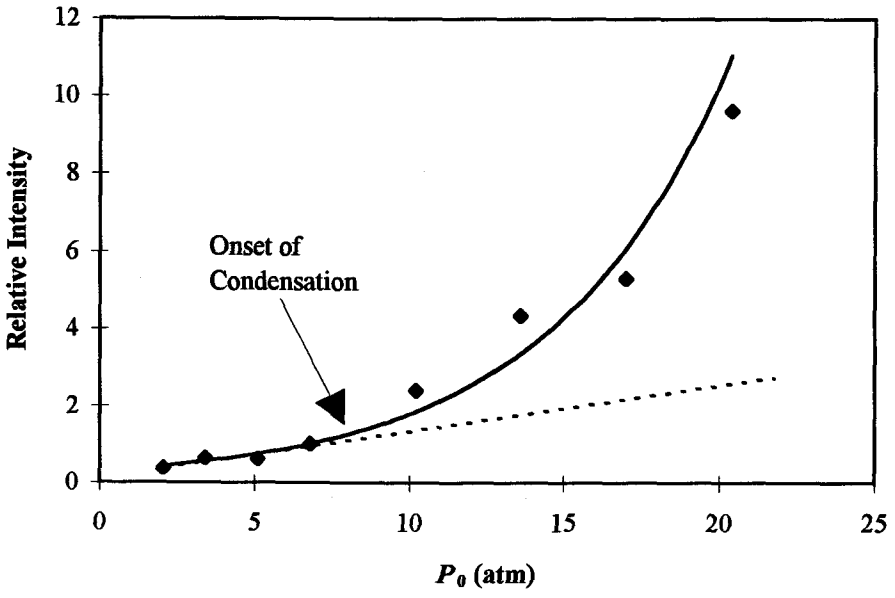

Figure 5.11 The onset of condensation determined by Rayleigh scattering. The dashed line is the linear increase in intensity predicted for a non-condensing jet. Data taken at $X/D = 0.8$ and $T_0 = 193$ K.

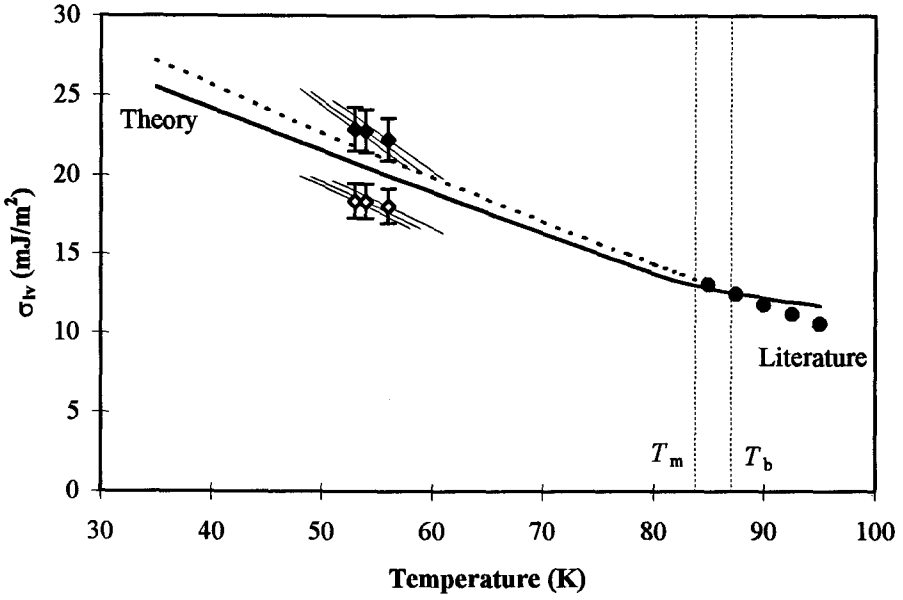

Figure 5.12 Surface tension of liquid argon deduced from nucleation rates. Solid diamonds represent the values adjusted for size using Tolman's relation.

Table 5.3 Expansion conditions which result in the formation of liquid argon for a jet with $D = 0.25$ mm.[a] Assumed nucleation rates are also listed.

	Neat	Neat	Neat
P_0 (atm)	5.1	8.5	15.3
T_0 (K)	163	193	233
T_S (K)	93	94	96
T (K)	(53)	(54)	(56)
P_v (atm)	0.31	0.35	0.45
P_{eq} (atm)	1.9×10^{-3}	2.6×10^{-2}	4.7×10^{-2}
υ_m (m^3)	4.1×10^{-29}	4.1×10^{-29}	4.1×10^{-29}
J (m^{-3} s^{-1})	1×10^{26}	1×10^{26}	1×10^{26}
r^* (Å)	4.1	4.1	4.3
n^* (#)	11	11	12
σ_{lv} (mJ/m^2)	18.4	18.3	18.0
$\sigma_{lv,\infty}$ (mJ/m^2)	22.9	22.8	22.3

[a]Thermodynamic data have been taken from references 25 and 76.

In view of the simplicity of the measurements, it is clear that Rayleigh scattering is a powerful tool in determining the onset of clustering. Additionally, the theory indicates that the anisotropic scattering I_{VH} differs in its N dependence for liquids and solids, due to the relative order in the solid (see Table 5.4).[38] Thus, in future studies, it may be possible to distinguish between liquid/amorphous and solid clusters by comparing the N dependence of the I_{VV} and I_{VH} scattering intensities. This feature makes Rayleigh scattering a promising tool for the study of cluster properties.

Table 5.4 The N dependence of the I_{VV} and I_{VH} scattering intensities of gases, liquids, and solids.

	Gas	Liquid/Amorphous	Solid[a]
I_{VH}	N	N	N, N^2
I_{VV}	N	N^2	N^2

[a]The N dependence of I_{VH} intensity for solids also depends on the crystall lattice.

5.3 Solid Surfaces

There is very little known about the surface tension of solids since it is extremely difficult to measure this quantity. The success of using nucleation theory to determine the surface tension of supercooled liquids, however, led us to believe that it might be possible to use the same method to determine the surface tension of solids. Recall from earlier discussion of expansion isentropes that the initial phase of the clusters can be controlled by adjusting the stagnation conditions. Thus, by choosing appropriate P_0 and T_0 values, we can force the isentrope to cross the coexistence curve below the triple point, which favors the formation of solid clusters. In the following sections, we will discuss experimentally determined σ_{sv} values for solid nitrous oxide, acetylene, and carbon dioxide.

5.3.1 Solid Nitrous Oxide

Nitrous oxide is an interesting molecule in that its physical properties are very similar to those of carbon dioxide and acetylene, materials which are solids when the

vapor pressure is 1 atm. Nitrous oxide does have a region of normal liquid existence, between 182.3 K and 184.7 K,[76] but due to the narrow range of this, and the high triple point pressure (~0.9 atm), it is relatively easy to bypass the liquid phase and directly form solid clusters in a jet.

In this work, 5% and 30% N_2O/He mixtures were used to produce solid clusters in a jet expansion. As Figure 5.13 shows, the stagnation conditions were chosen such that the isentrope would cross the coexistence curve at or below the triple point, ensuring the initial formation of solid clusters. Figure 5.14 shows a plot of CARS spectra taken for N_2O clusters at the initial position where clusters are observed. The broad peak centered at ~1291 cm^{-1} is attributed to the crystalline phase and has a linewidth of about 5 cm^{-1} which is in good agreement with the reported literature width of 6 cm^{-1}.[87] There is no evidence of liquid N_2O, which would have a broad feature (~4 cm^{-1}) centered at ~1284 cm^{-1}.[88]

The nucleation rate for each expansion was calculated using the same procedure described for methane and ethylene. As in the case of ethylene, cluster sizes have been estimated from results of other similar experiments. The vapor-solid nucleation rates listed in Table 5.5 are comparable to those observed for vapor-liquid transitions. This is to be expected since according to the nucleation theory presented in Chapter 2, the kinetics of formation of a solid and liquid nucleus are identical.

The solid squares in figure 5.15 represent the surface tension of solid nitrous oxide calculated from the data in Table 5.5. The values have been adjusted using Tolman's relation with $\delta = 0.65$ Å to take into account variations with size. Notice that

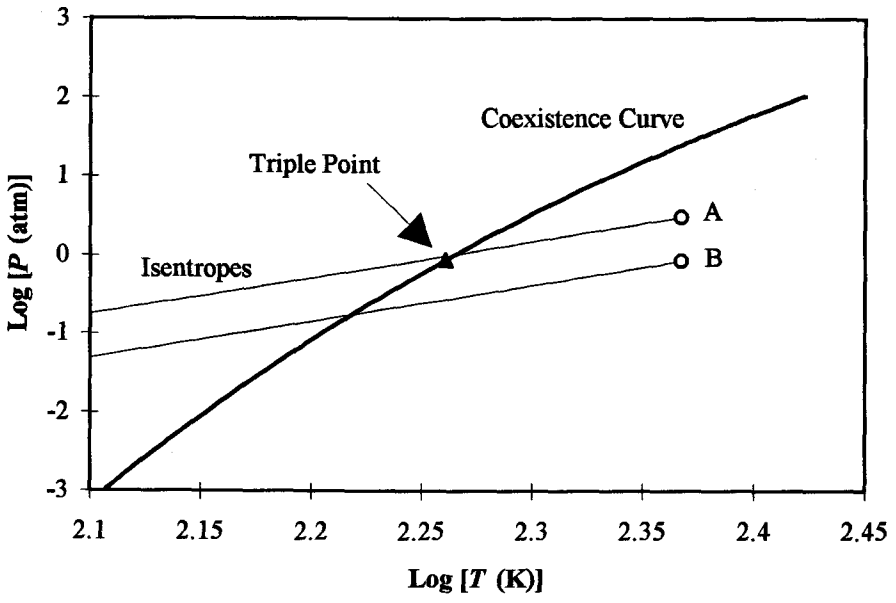

Figure 5.13 Calculated isentropes for expansions of nitrous oxide. A: 30% Mix (P_0 = 10 atm, T_0 = 2333 K). B: 5% mix (P_0 = 17 atm, T_0 = 233 K).

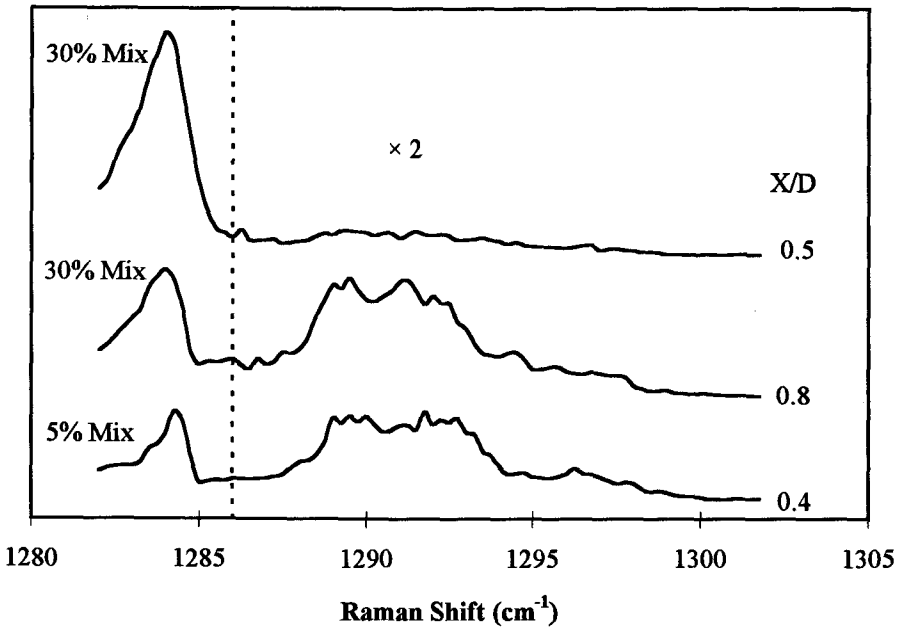

Figure 5.14 CARS spectra of nitrous oxide clusters at *X/D* positions where clusters are first observed. The cluster intensities are expanded by a factor of 2.

Table 5.5 Data for several expansions of nitrous oxide for a jet with $D = 0.3$ mm.[a] The # sign indicates number of molecules. Values in parentheses have been estimated.

	30% Mix	5% Mix
P_0 (atm)	10	17
T_0 (K)	233	233
T_S (K)	190	174
X/D	0.8	0.4
Mach Number	2.3	2.1
T (K)	(130)	(114)
υ (m/s)	631	810
Δt (ns)	118	93
P_v (atm)	0.49	0.12
P_{eq} (atm)	1.5×10^{-3}	2.0×10^{-5}
υ_m (m^3)	4.1×10^{-29}	4.1×10^{-29}
N^*_{Total} (#/m^3)	8.2×10^{25}	1.2×10^{25}
Z	1.5	0.9
R_C (nm)	(10)	(6)
M_C (#)	5.9×10^4	1.3×10^4
N^*_C (#/m^3)	1.3×10^{20}	4.1×10^{20}
J (m^{-3} s^{-1})	1.1×10^{27}	4.4×10^{27}
r^* (Å)	3.9	3.2
n^* (#)	10	6
σ_{lv} (mJ/m^2)	48.5	46.9
$\sigma_{lv,\infty}$ (mJ/m^2)	64.9	65.8

[a]Thermodynamic data have been taken from references 25, 76, and 91.

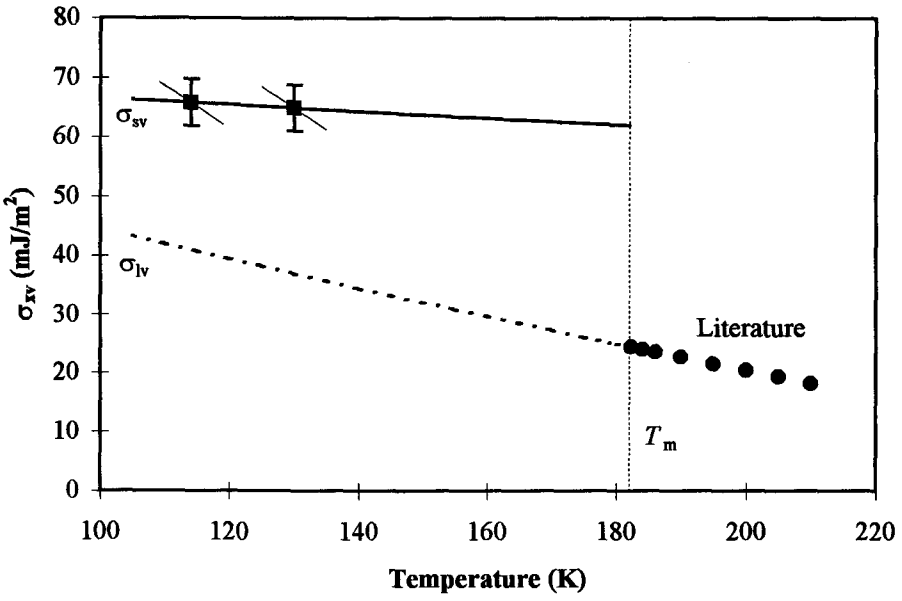

Figure 5.15 The surface tension of solid nitrous oxide calculated from nucleation rates. The solid line is a linear fit of the experimental points.

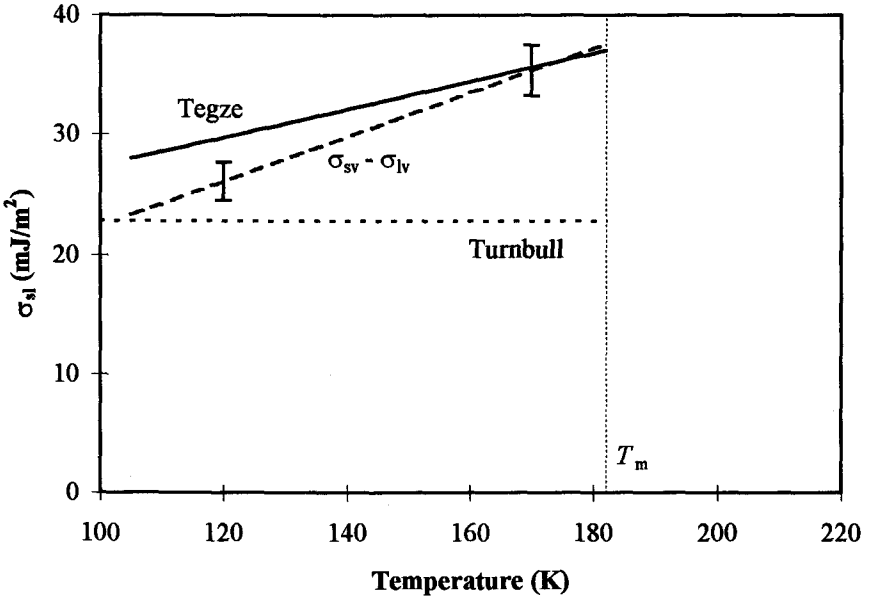

Figure 5.16 The solid-liquid interfacial tension of nitrous oxide calculated from Young's equation and compared to the models of Tegze and Turnbull.

the surface tension of the solid at a given temperature is considerably higher than the corresponding value for the liquid. This is mainly a consequence of the larger difference in density between the solid and vapor compared to the liquid and vapor.

The σ_{sv} values reported here for nitrous oxide are the first of their kind and as a result, we have no experimental or theoretical numbers to which to compare our results. However, judging from the success of this method in predicting the surface tension of supercooled liquids, we are confident that the results obtained for nitrous oxide are a reasonable representation of the true σ_{sv} values.

One way of evaluating the validity of these σ_{sv} values is by using Young's equation (4.22) to calculate σ_{sl}, which can then be compared to estimates obtained from any of the available semiempirical models. This is done by taking the difference between the solid and dashed lines in Figure 5.16. The σ_{sl} values calculated from Young's equation, along with Turnbull and Tegze's predicted values, are plotted in Figure 5.16.

Considering the relative error of the σ_{sv} values (which do not include the uncertainty in temperature), and the fact that we are extrapolating from two points, we can only say that the agreement between our results and Tegze's model is reasonable. This result could of course be fortuitous; accordingly we examine next the data for acetylene and carbon dioxide to determine whether similar results are obtained for other systems.

5.3.2 Solid Acetylene

Acetylene exists in liquid form at slightly above atmospheric pressure (melting occurs at 191.7 K and 895 Torr). Acetylene clusters have been studied extensively in our laboratory by Minarik, Lee, and Triggs.[28,36] They have each observed that, depending on the stagnation conditions, either liquid or cubic solid clusters are formed. Upon further cooling in the jet, it is possible to observe the cubic solid to orthorhombic solid transition as well. In this section, however, we will only be interested in experiments where the initial phase of the clusters was cubic solid. The conditions which result in the formation of cubic solid clusters are listed in Table 5.6.

The solid squares in Figure 5.17 represent the surface tension of solid acetylene calculated from the data in Table 5.6. Once again, these values are significantly larger than the surface tension of the liquid. Figure 5.18 shows the σ_{sl} values that have been calculated from Young's equation using the same procedure described for nitrous oxide. Also plotted in this figure are Turnbull and Tegze's predicted values and Minarik's experimental values.

Figure 5.18 shows that there is good agreement between the values deduced from Young's equation and Tegze's model. The results, however, are significantly higher than Minarik's experimental values. The reason for this appears to be that the cluster sizes deduced by Minarik are 2-3 orders of magnitude smaller than the actual sizes due to an error in his cooling curve calculation. Since the liquid-solid nucleation rate is inversely proportional to cluster size (Section 2.3.3), Minarik's nucleation rates are too high by about 6-9 orders of magnitude. Also, due to the large size of these clusters,

Table 5.6 Acetylene expansion conditions which result in the formation of cubic solid.[a] Assumed nucleation rates are also listed.

	4% Mix[b]	10% Mix[b]	10% Mix[c]	12% Mix[b]
P_0 (atm)	31	27	23	27
T_0 (K)	185	213	252	200
T_S (K)	192	200	189	208
T (K)	(132)	(140)	(129)	(148)
P_v (atm)	0.51	0.84	0.36	1.38
P_{eq} (atm)	2.3×10^{-3}	7.2×10^{-3}	1.4×10^{-3}	2.0×10^{-2}
υ_m (m^3)	5.9×10^{-29}	5.9×10^{-29}	5.9×10^{-29}	5.9×10^{-29}
J (m^{-3} s^{-1})	1×10^{27}	1×10^{27}	1×10^{27}	1×10^{27}
R_s^* (Å)	4.5	4.8	4.4	5.0
n^* (#)	10	11	9	13
σ_{sv} (mJ/m^2)	37.4	37.0	36.5	36.7
$\sigma_{sv,\infty}$ (mJ/m^2)	48.2	47.0	47.3	46.1

[a]Thermodynamic data have been taken from references 25, 76, and 92.
[b]Data obtained by Minarik with He as the carrier gas.[28]
[c]Data obtained by Lee with Ne as the carrier gas.[36]

heterogeneous nucleation may have played a role in the condensation process. As a result, the σ_{sl} values calculated from the measured rates are expected to be too small by about 15-25%.

Overall, we feel that these results are encouraging for two reasons. First, they show that the agreement observed for nitrous oxide is not an isolated case. Second, and

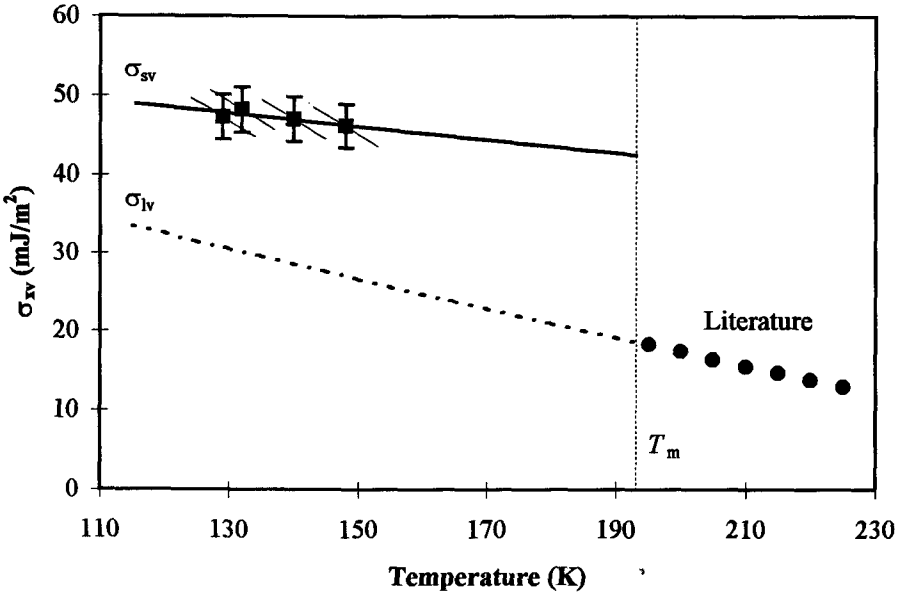

Figure 5.17 The surface tension of cubic solid acetylene calculated from nucleation rates. The solid line is a linear fit of the experimental points.

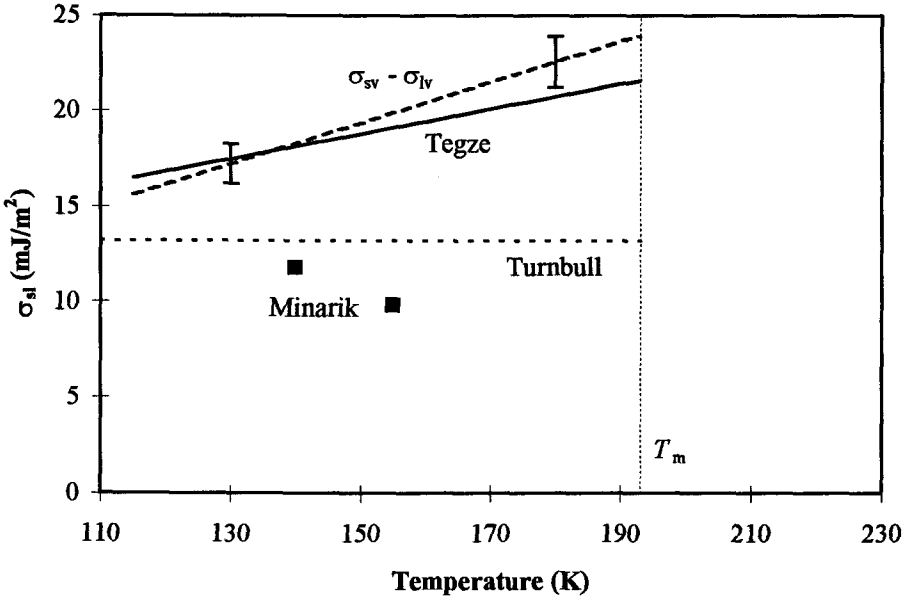

Figure 5.18 The solid-liquid interfacial tension of acetylene calculated from Young's equation and compared to Tegze's model. The solid squares are experimental values obtained by Minarik.[28]

more important, they show that the σ_{sl} values calculated from the experimentally determined σ_{sv} values are within the predicted range and that they also exhibit the correct temperature dependence. This means that the σ_{sv} values themselves are of the right order of magnitude. As a final test example, we will look at results for carbon dioxide in the next section.

5.3.3 Solid Carbon Dioxide

Carbon dioxide is yet another interesting molecule in that it exists in liquid form only at pressures above 5.2 atm (melting point of 216.6 K).[76] Thus, one can form solid clusters in a jet expansion with relative ease. In fact, studies in our laboratory by Brown,[89] Richardson,[42] and Mayer[38] have shown that only solid clusters are formed, even under extreme conditions (high P_0, low T_0) where liquid clusters might be expected.

The expansion conditions used to form solid carbon dioxide clusters are listed in Table 5.7. As before, the surface tension of solid carbon dioxide was calculated from this data and the results are displayed in Figure 5.19. The solid squares represent the experimental values which have been adjusted using Tolman's relation and the solid line is a linear fit of these points. The features observed for carbon dioxide are similar to those observed for nitrous oxide and acetylene; namely, σ_{sv} is larger than σ_{lv} and increases with decreasing temperature.

The solid-liquid interfacial tension was calculated from Young's equation and the results, along with Tegze and Turnbull's predictions, are shown in Figure 5.20. Although the agreement between our results and Tegze's model is not as good as it was for nitrous

Table 5.7 Expansion conditions which result in the formation of solid carbon dioxide.[a] Assumed nucleation rates are also listed.

	Neat[b]	10% Mix[b]	5% Mix[b]	Neat[c]	12% Mix[c]	5% Mix[c]
P_0 (atm)	27	28	14	14	14	14
T_0 (K)	298	273	298	248	248	260
T_S (K)	222	196	175	226	192	179
T (K)	(162)	(136)	(115)	(166)	(132)	(119)
P_v (atm)	1.78	0.43	0.06	2.33	0.31	0.09
P_{eq} (atm)	4.0×10^{-2}	1.0×10^{-3}	1.6×10^{-5}	6.4×10^{-2}	5.1×10^{-4}	3.9×10^{-5}
υ_m (m^3)	4.6×10^{-29}	4.5×10^{-29}	4.5×10^{-29}	4.6×10^{-29}	4.5×10^{-29}	4.5×10^{-29}
J (m^{-3} s^{-1})	1×10^{26}	1×10^{27}	1×10^{27}	1×10^{26}	1×10^{27}	1×10^{27}
r^* (Å)	5.0	3.9	3.2	5.1	3.8	3.4
n^* (#)	16	9	6	17	8	7
σ_{sv} (mJ/m^2)	46.3	49.0	47.0	46.1	48.7	47.7
$\sigma_{sv,\infty}$ (mJ/m^2)	58.4	65.4	65.9	57.9	65.5	66.2

[a]Thermodynamic data taken from references 25 and 76.
[b]Data obtained by Brown with He as the carrier gas.[89]
[c]Data obtained by Mayer with He as the carrier gas.[38]

oxide and acetylene, the values are within the right range and they exhibit the correct temperature dependence.

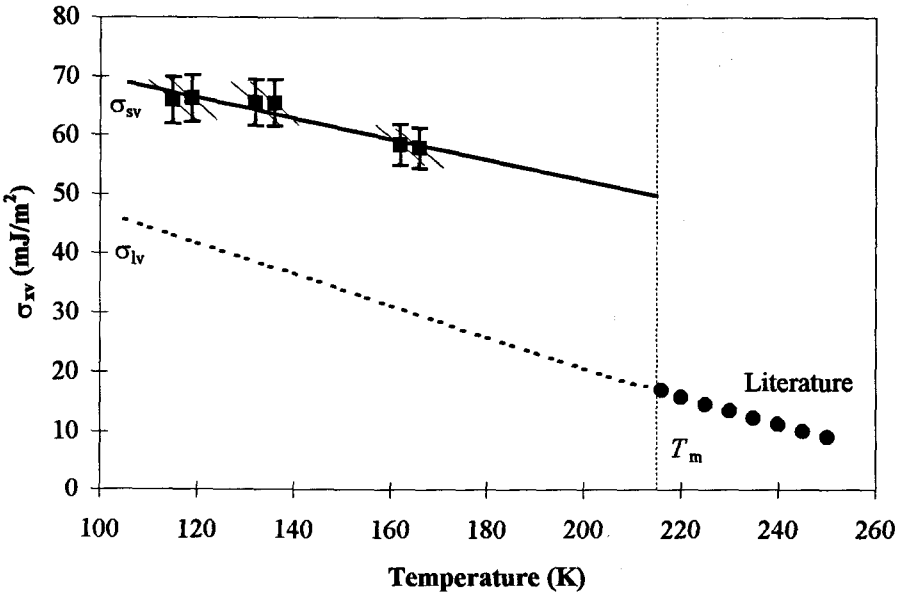

Figure 5.19 The surface tension of solid carbon dioxide calculated from nucleation rates. The solid line is a linear fit of the experimental points.

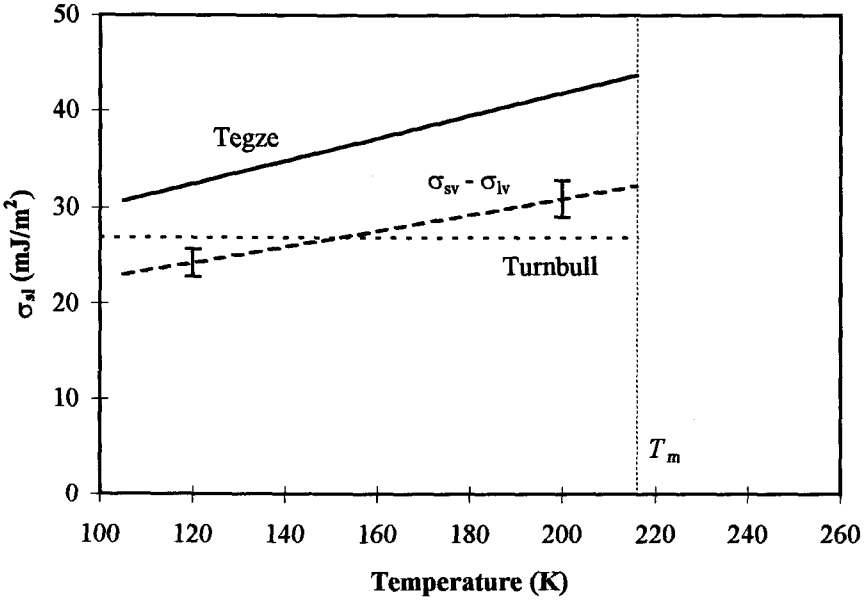

Figure 5.20 The solid-liquid interfacial tension of carbon dioxide calculated from Young's equation and compared to Tegze's model.

5.4 Final Remarks

The results presented in this chapter show that it is possible to determine the surface tension of supercooled liquids and solids from measured nucleation rates and that the results are in good accord with theoretical and empirical predictions. However, it must be admitted that there are legitimate questions as to the physical meaning of the results and the models. For example, the data for all the systems studied show that the critical nucleus is composed of only about 5-15 molecules. How does one define a surface for a such a small ensemble and does surface tension, generally accepted as a bulk quantity, have any meaning in this regime? It is difficult to answer this question for this is a region where it is virtually impossible to study equilibrium thermodynamic properties.

Additionally, there are concerns regarding the theory of homogeneous nucleation. Recent experiments and calculations have shown that classical nucleation theory can at times severely underestimate nucleation rates.[93-95] Correction factors have been suggested[11,94-95] which bring the theory into better agreement with experiments but these add complexity which is hard to justify given the quality of the available data.

Another problem is the lack of the required auxiliary thermodynamic data over a wide temperature range, and especially in the supercooled regime. Errors in extrapolating available data can have a significant effect on the results; for example, relatively minor deviations in the liquid or solid vapor pressure can change the value of σ by 10-20%.

Despite these qualifications and concerns, we feel that the material presented in this chapter forecasts an exciting future in the field of surface science and nucleation. We have shown that our technique, unusual as it may be, provides one of the few available means to obtain reasonable surface tension values for supercooled liquids and solids for at least a limited number of systems. In the case of liquids, the results are in remarkable accord with values predicted from a simple theoretical model and a Lennard-Jones potential. Although not directly applicable to solids, extensions of the theory may be stimulated by our experimental values of the surface tension of solids, which we emphasize are very difficult to determine by any other method.

The success and versatility of this method also opens the door to a wide variety of experiments. Some areas of interest include ion induced nucleation from the vapor phase, nucleation on foreign particles, and nucleation in supersaturated solutions. Efforts are underway in our laboratory to pursue some of these experiments. In the next chapter, we will show that this same method can also be used to determine the solid-liquid interfacial tension. Minarik[28] and Bartell[20] have already demonstrated the ability to measure the solid-solid interfacial tension using this technique.

6. SOLID-LIQUID INTERFACIAL TENSION

In the previous chapter we demonstrated the capability to form liquid clusters, measure the nucleation rate, and determine the liquid-vapor interfacial tension. If the liquid clusters are allowed to cool further in the jet expansion, they will eventually transform to the crystalline phase. In this chapter we show that Raman spectroscopy can be used to monitor the freezing rate of these clusters. The freezing rate can then be used to calculate the nucleation rate and hence the solid-liquid interfacial tension.

6.1 Nitrogen

Several years ago, Beck[37] and Yang[96] observed the liquid to solid phase transition of nitrogen clusters produced in a jet expansion. Their main interest, however, was to study the phase, temperature, and size of the clusters. Here, we will reexamine the nitrogen data focusing our attention on the nucleation kinetics and the solid-liquid interfacial tension.

Yang produced nitrogen clusters in a neat expansion with a backing pressure of 40 atm and a nozzle temperature of 160 K. Figure 6.1 shows a plot of the spectra of the clusters as a function of X/D. The liquid and solid peaks are centered around 2326.4 cm^{-1} and 2326.7 cm^{-1}, respectively. Note that although the liquid and solid peaks are less than 0.3 cm^{-1} apart from each other, they are still distinguishable due to the narrow linewidth of the peaks, which is less than 0.1 cm^{-1}. The freezing of the liquid clusters begins at $X/D \approx 12.5$ and is complete by $X/D \approx 15$, implying that the clusters freeze in less than 0.8 μs.

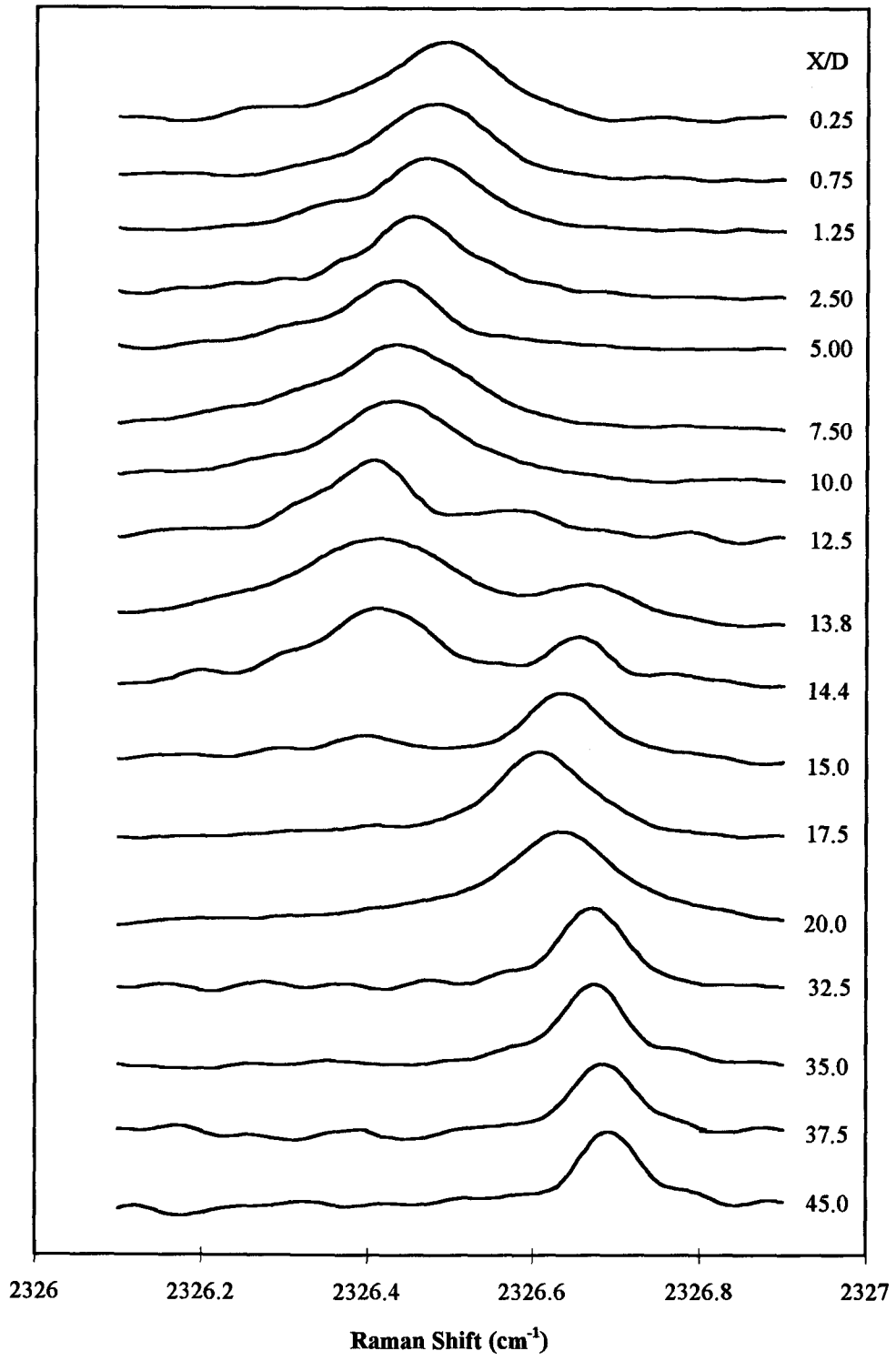

Figure 6.1 CARS spectra of liquid and β-solid nitrogen clusters produced in a neat expansion.

In order to extract the nucleation rate from this data, we must first determine whether the rate limiting step in the freezing of a cluster is the formation of a critical nucleus or the growth of the crystal. Some insight comes from a consideration of the adiabatic and isothermal freezing processes (see figure 2.6). Careful analysis of the cluster peaks in Figure 6.1 reveals some interesting features. First, as the liquid begins to freeze, the linewidth of the liquid peak begins to broaden. This is an indication that the temperature of the liquid is increasing in the freezing region. Meanwhile, the solid peak is shifting to **lower** frequency, implying that the temperature of the solid is also **increasing** in the freezing zone. The temperature of the solid begins to decrease **only** after the liquid has completely disappeared (see Figure 6.2). These observations closely match the isothermal freezing model shown in Figure 2.6.

Figure 6.2 also shows that, in the freezing zone, there is a mixture of liquid and solid at **distinctly different temperatures**, which is indicative of the adiabatic freezing process. However, the adiabatic model predicts a temperature difference of $\Delta H_{fus}/C_{p,liq} \sim$ 16 K between the liquid and solid clusters, which is twice as much as the observed temperature difference of about 3-8 K. Thus, it appears that freezing of nitrogen clusters is not completely adiabatic or isothermal, but rather an intermediate process which exhibits characteristic properties of both models.

A second issue is that the rate of freezing may be limited by the rate of removal of the heat of fusion by evaporation and collisions. Since we are in the low density region of the jet, we expect the number of collisions to be small and that evaporation is the main mechanism of heat loss. From modeling calculations of the type used for

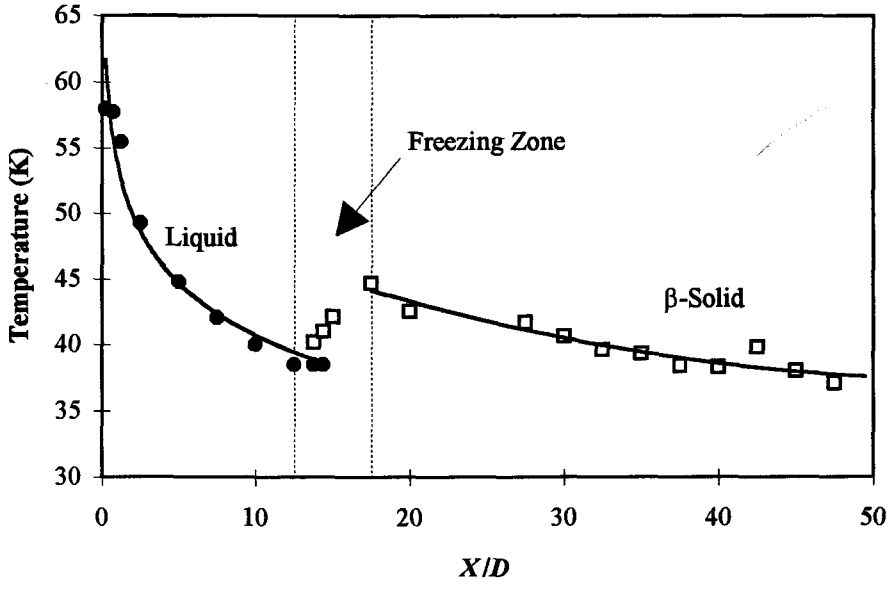

Figure 6.2 Liquid and solid temperatures of nitrogen clusters produced in a neat expansion. Cluster temperatures are estimated from temperature-frequency relations for the bulk liquid and solid which have been determined by Beck.[37]

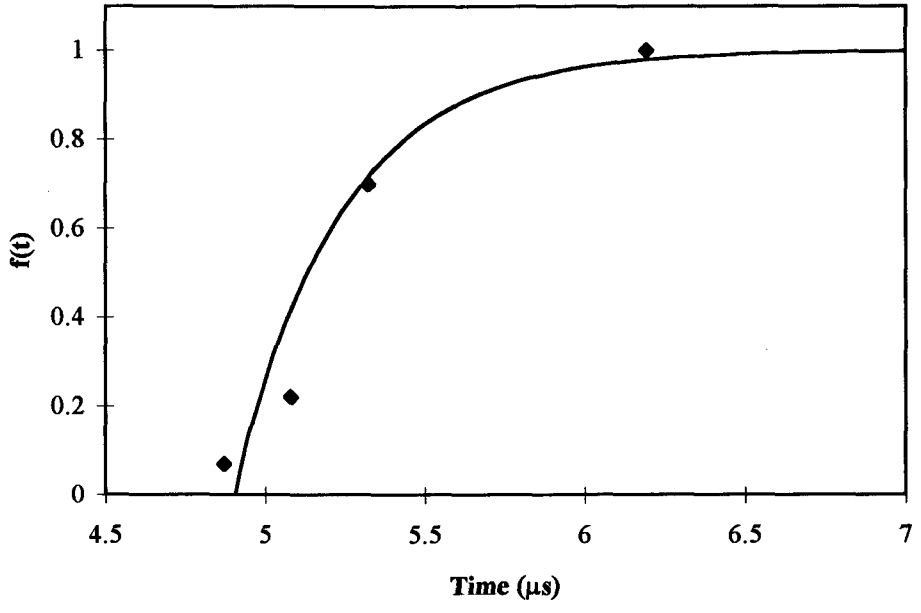

Figure 6.3 Fraction of clusters that have frozen as a function of time.

computation of cooling curves, it appears that heat removal should be faster than the observed time of freezing.

In our nucleation model, it was assumed that freezing was mononuclear and that the clusters froze immediately after the formation of a critical nucleus (adiabatic freezing). The above analysis suggests that freezing is not immediate and there may be clusters composed of a liquid/solid mix, which could permit another nucleus to form within the liquid region. This process is not viewed as likely however because, once a nucleus is formed, the temperature of the cluster increases and the probability of forming another nucleus decreases.

A criterion to establish whether freezing is mononuclear has been suggested by Kashchiev.[97] According to him, freezing is mononuclear if the linear growth rate G of the solid obeys the inequality

$$G >> JV_C^{4/3}\xi^{1/3} \tag{6.1}$$

where V_C is volume of the cluster and ξ is a ratio of the volume of the critical nucleus to the volume of the cluster. For nitrogen clusters formed in a neat expansion, we find that G must be much larger than 6×10^{-3} m/s. For comparison, Bartell has determined that the freezing of ammonia clusters with a radius of 5 nm will be mononuclear if G is much larger than 5×10^{-3} m/s.[21]

Experimental growth rates at large supercoolings are not known so it is difficult to ascertain whether Kashchiev's criterion is satisfied. However, recent molecular dynamic simulations[98] have shown that the growth rate for argon crystals at half the

melting point is very large, 80 m/s, about 10^4 times the rates computed above for mononuclear growth. We expect that growth rates for nitrogen will be of the same order of magnitude because of the large supercooling. Thus, we are confident that Kashchiev's criterion is fulfilled and that freezing is mononuclear.

Assuming then that the freezing rate is not governed by the growth rate of the crystal, we can now proceed to determine the nucleation rate. Figure 6.3 shows a plot of the fraction of clusters that are frozen versus time. The solid line is the best fit of the data points obtained by varying the parameters JV_C and t_0 in (2.25). The fit shows that the clusters begin to freeze 4.8 μs after exiting the nozzle and that the quantity, JV_C, is ~3 MHz. Using a cluster radius of 17 nm determined by Yang from cooling curves,[96] we find that the implied nucleation rate J is 1.5×10^{29} m^{-3} s^{-1}. This is comparable to nucleation rates for freezing measured by electron diffraction for other jet expansions of molecules such as CCl_4 (1.1×10^{29} m^{-3} s^{-1}),[16-17] NH_3 (1.2×10^{30} m^{-3} s^{-1}),[99] and H_2O (~10^{30} m^{-3} s^{-1}).[21]

This experimental nucleation rate, along with the required physical properties listed in Table 6.1, can now be used to calculate a value for σ_{sl}. Figure 6.4 shows plots of σ_{sl} as a function of nucleation temperature calculated for several cluster sizes. These plots show that even if the estimated cluster radius of 17 nm is off by a factor of five, the calculated σ_{sl} value would vary by less than 6%. Therefore, it is not necessary to have extremely accurate cluster sizes. The simple cooling curve model, which predicts cluster sizes within a factor of two, is sufficient for these calculations.

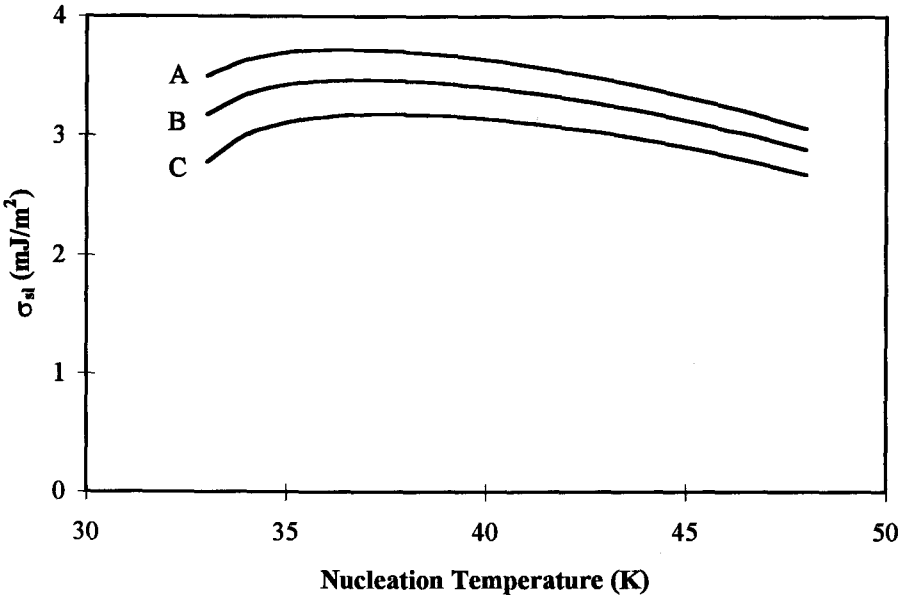

Figure 6.4 Calculated σ_{sl} values as a function of nucleation temperature assuming different cluster sizes. A: $r = 75$ nm, $J = 10^{27}$ m^{-3} s^{-1}. B: $r = 17$ nm, $J = 10^{29}$ m^{-3} s^{-1} C: $r = 3$ nm, $J = 10^{31}$ m^{-3} s^{-1}.

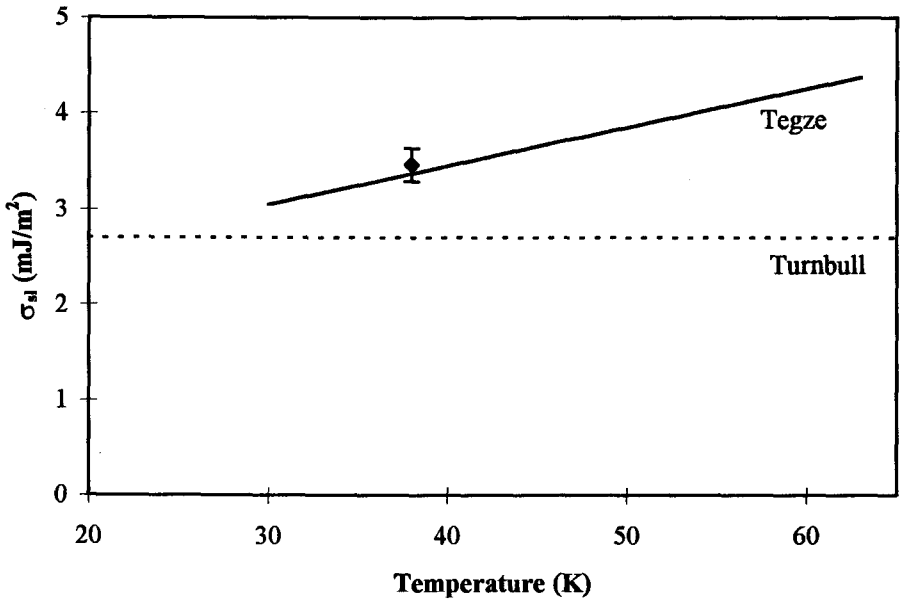

Figure 6.5 Experimental σ_{sl} value compared to predicted σ_{sl} values by Tegze and Turnbull.

Table 6.1 Thermodynamic data used in the calculation of σ_{sl} for nitrogen and methane.[a]

	N_2	CH_4
T_m (K)	63.19	90.66
$\Delta H_{fus,mp}$ (J/mole)	720.9	937.2
X/D	12.5	~1.8
T (K)	38	40
υ_m (m^3)	4.8×10^{-29}	5.1×10^{-29}
η (Pa s)	1.9×10^{-3}	1.1×10^{-2}
$C_{p,liq}$ (J/mole K)	46.2	37.4
$C_{p,sol}$ (J/mole K)	36.9	28.1
JV_C (MHz)	3	0.7
R_C (nm)	17	8
J (m^{-3} s^{-1})	1.5×10^{29}	3.1×10^{29}
r^* (Å)	8.7	7.7
n^* (#)	58	37
σ_{sl} (mJ/m^2)	3.5	4.1

[a]Thermodynamic data taken from references 25, 44, 76, 77, and 100.

Also, keep in mind that Figure 6.4 does not represent the temperature dependence of σ_{sl}. Instead, it shows the values of σ_{sl} which reproduce the observed nucleation rate for different assumed cluster temperatures. From Figure 6.2, we find that in fact the temperature of the liquid is approximately 38 K at the onset of crystallization. This nucleation temperature is in excellent accord with the predicted evaporative cooling

temperature of 34-36 K for liquid nitrogen.[21] At this temperature, we calculate a σ_{sl} value of 3.5 mJ/m^2, which is in fair agreement with a value of 2.7 mJ/m^2 predicted by Turnbull's relation. Another comparison can be made using Tegze's model to calculate σ_{sl}. Figure 6.5 shows a plot of σ_{sl} calculated using his relation over the temperature range of interest. It is seen that there is excellent accord between the experimental value at 38 K and a value of 3.4 mJ/m^2 calculated from Tegze's model. Also note that this value has not been corrected using Tolman's relation discussed in the previous chapter. This is because we expect size effects to be very small since the radius of the critical nucleus is almost twice as large as those observed in nucleation from the vapor phase. Furthermore, we anticipate that δ will also be very small since the density change across the solid-liquid interface is much smaller than that across a liquid-vapor or solid-vapor interface. Thus, the ratio δ/r^*, will be small and the reported value of σ_{sl} is an accurate representation for that of a bulk flat interface.

It may also be noted that σ_{sl} is, of course, much lower than the experimental σ_{lv} value of 12.2 mJ/m^2 at the melting point or, by extrapolation, 18.6 mJ/m^2 at 38 K. By applying Young's equation, we can estimate a σ_{sv} value of 22.1 mJ/m^2 for solid nitrogen at 38 K. The relative magnitudes of σ_{sv}, σ_{lv}, and σ_{sl} can be understood qualitatively from the degree of disparity between the two phases across the interface; namely, the difference in density.

The fact that freezing of nitrogen clusters is not completely adiabatic and exhibits some isothermal character means that the nucleation rate determined is somewhat slower than the actual nucleation rate. As a result, the calculated σ_{sl} should be considered an

upper limit and the actual σ_{sl} is expected to be somewhat smaller. This effect is minor however; according to Figure 6.4, if the actual nucleation rate were 100 times faster, of the order of 10^{31} m^{-3} s^{-1}, then the calculated σ_{sl} would drop by only 10%, to a value of 3.2 mJ/m^2.

6.2 Methane

In Chapter 5, we described several experiments, including a neat and seeded expansion, where we observed the formation of liquid clusters from vapor. In these same experiments, we attempted to study the liquid-solid phase transition of methane by probing the clusters farther out in the jet. The main problem with methane is that for the ν_1 transition, the linewidth of the liquid and solid peaks are 2-3 cm^{-1} at FWHM (full-width half-max) while the frequency difference between the two peaks is only 1 cm^{-1}.[101] This means that the liquid and solid peaks will be overlapped and direct identification of the phase of the clusters is not possible.

Figures 6.6 and 6.7 show plots of scans taken at selected *X/D* for the neat and 25% mix expansion, respectively. The peak at ~2916 cm^{-1} is the monomer and the peak at ~2905 cm^{-1} is the cluster peak. The features observed for both expansions are identical with the main difference being that the intensity of the cluster peaks for the mix are a factor of two stronger than those for the neat expansion, indicating a higher extent of clustering due to colder temperatures. The frequencies and linewidths of the cluster and monomer peaks at each *X/D* position are summarized in Appendix D.

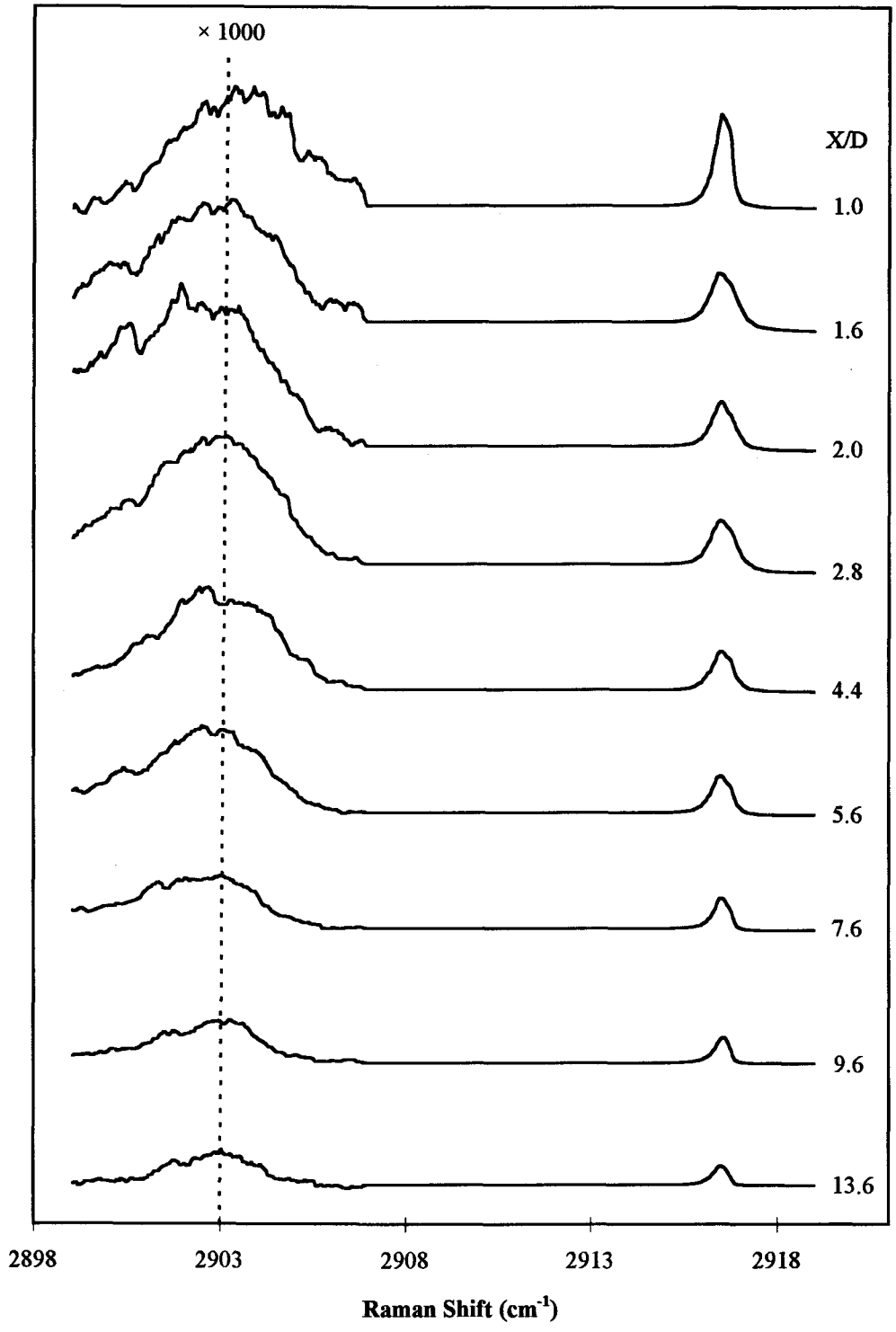

Figure 6.6 CARS spectra of neat methane clusters at various positions in the jet.

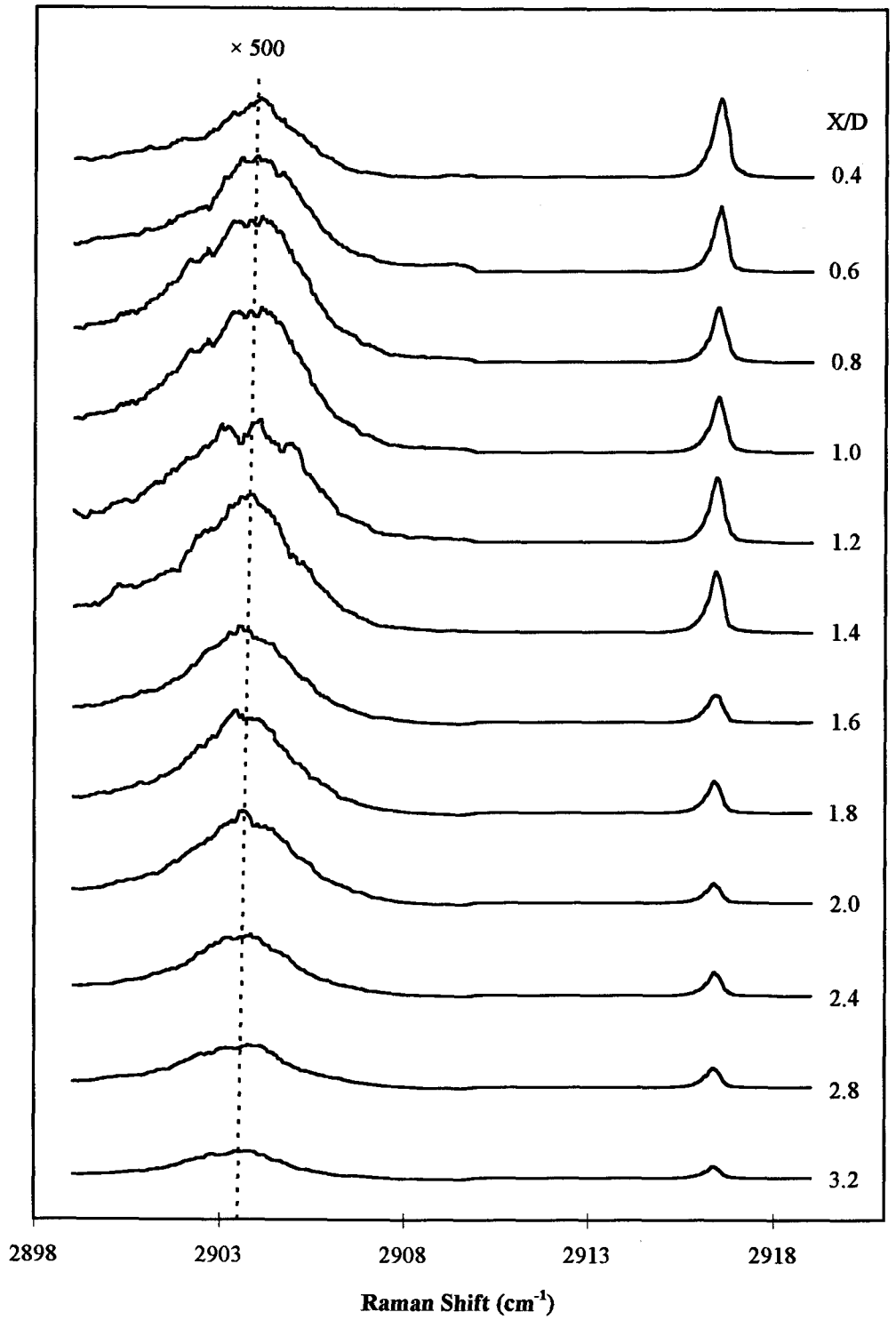

Figure 6.7 CARS spectra of 25% methane clusters at various positions in the jet.

The dashed lines in Figures 6.6 and 6.7 are used to locate the cluster peak centers at each *X/D* position. As expected, the peak centers shift to lower frequency as we move away from the nozzle due to the fact that the clusters get colder. Not much can be said regarding the cluster frequencies observed in the two expansions since the cluster phase is unknown. The only noticeable difference between the two data sets is that the cluster linewidths for the mix expansion are significantly narrower than the linewidths of the neat clusters. This is an indication of colder temperatures and/or different phases and will be discussed in more detail shortly.

One method of identifying the cluster phase is to examine the temperature profile assuming that the clusters are either all liquid or all solid. Figures 6.8 shows the temperature profiles for these cases for the neat expansion, as calculated from the bulk temperature-frequency relations given by (C.1) and (C.2) in Appendix C. The solid line, obtained assuming all liquid clusters, begins at about 100 K and drops down to about 47 K, indicating the formation of supercooled liquid droplets. The dashed line, obtained assuming all solid clusters, begins well **above** the boiling point and eventually falls below absolute zero. This anomalous behavior suggests that the clusters produced in the neat expansion are not crystalline solid and, therefore, must be liquid.

The same procedure can be used to help identify the phase of the clusters produced in the mix expansion. Figure 6.9 shows the temperature profile for the mix expansion assuming either liquid or solid clusters. The solid line shows the temperature of liquid clusters while the dashed line is obtained by assuming the clusters to be all

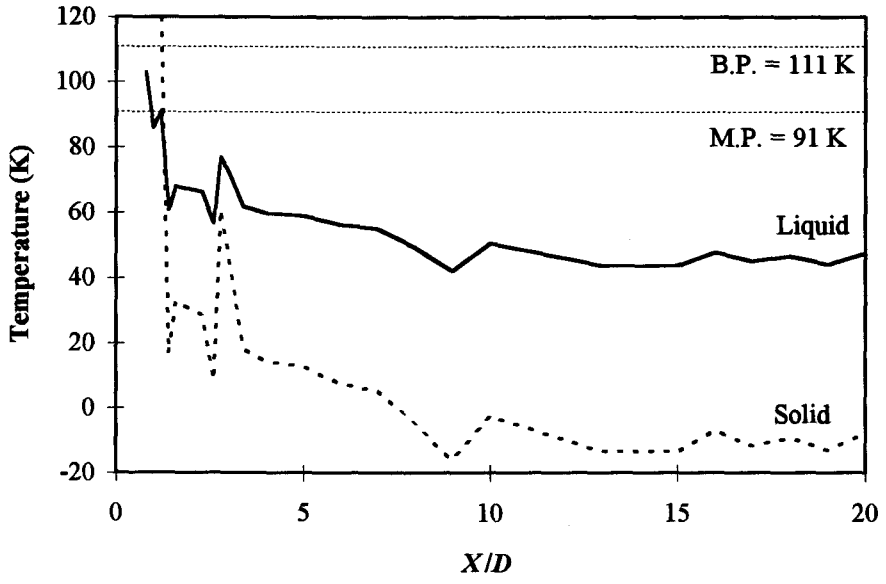

Figure 6.8 Temperature profile for methane clusters produced in a neat expansion, assuming all liquid or solid clusters.

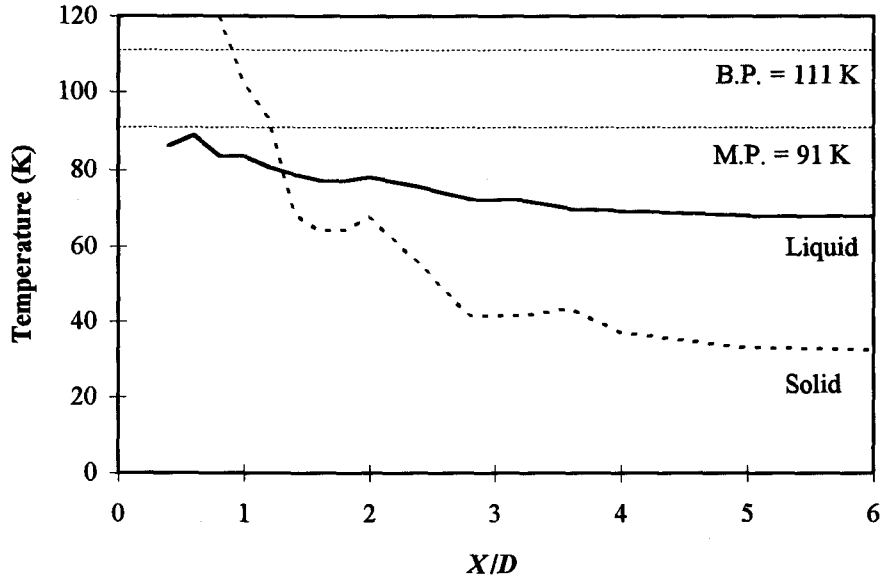

Figure 6.9 Temperature profile for methane clusters produced in a 25% mix expansion, assuming all liquid or solid clusters.

crystalline solid. Unlike the case for the neat expansion, we cannot eliminate one of the phases and must consider all possibilities.

These clusters are expected to be liquid in the initial stages of the expansion since the experimental conditions were such that the isentrope crossed the coexistence curve well above the triple point (Figure 5.1). This argument is supported by the temperature profiles in Figure 6.9, which show that close to the nozzle the clusters cannot be solid since their temperatures would be above the melting point. Farther away from the nozzle, however, the clusters can be liquid or solid and we must use alternate means to determine the phase.

One such method is to compare the cluster linewidths to those measured for bulk samples (see Appendix C). Figure 6.10 shows the measured cluster linewidths for the neat and mix expansions as a function of *X/D*. In the case of the neat expansion, we find that the cluster linewidths are ~4 cm^{-1} compared to ~3 cm^{-1} for bulk liquid samples, confirming our earlier conclusion that the neat clusters are liquid. The slight broadening of the cluster peaks, which has also been observed for nitrogen and carbon dioxide, is expected because there is a distribution of cluster sizes and temperatures in the jet giving rise to an inhomogeneous distribution of vibrational band centers which overlap to yield a single peak.

For the mix expansion, the measured linewidths are consistent with our prediction of liquid clusters in the early stages of the expansion. Farther away from the nozzle, however, the linewidth decreases and is not inconsistent with that of the bulk solid (~2.4 cm^{-1} near the melting point), suggesting that the clusters could have

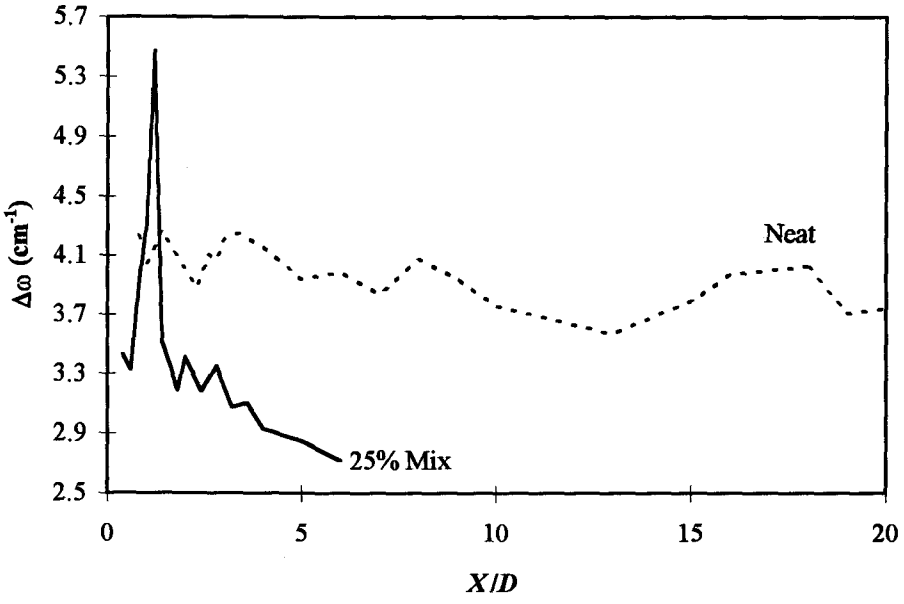

Figure 6.10 Cluster linewidths as a function of *X/D* for the neat and 25% mix expansions.

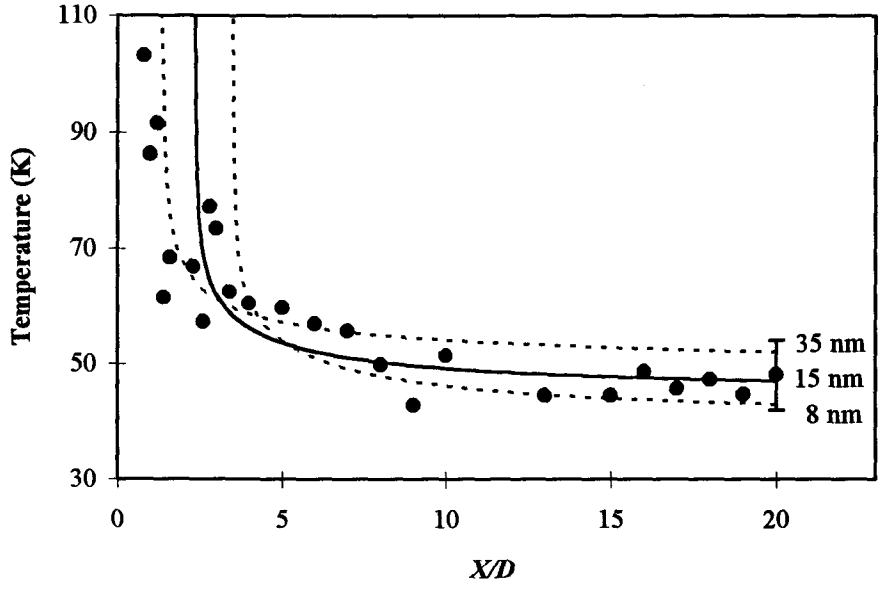

Figure 6.11 Cooling curve for liquid methane clusters produced in a neat expansion.

undergone a phase transition. Also, due to the overlap of the liquid and solid peaks, in the freezing zone we would expect to observe an increase in the measured linewidths, due to the warming of the liquid and the presence of solid, followed by a decrease in the linewidth due to the disappearance of the liquid and the cooling of the solid. As Figure 6.10 shows, this is in fact what we observe for the mix expansion.

The final evidence regarding the phase of the clusters is given by the size estimates obtained from the cooling curve model. Figure 6.11 shows a plot of the fit obtained for the neat expansion assuming all liquid clusters. As in all such analysis, the points at small *X/D* are ignored because the cooling curve model does not take into account many body collisions that take place close to the jet. According to this model, the liquid clusters have a mean radius of 15 nm, which is comparable to sizes obtained for neat expansions of nitrogen (17 nm) and carbon dioxide (13 nm).

A similar fit for the mix expansion, assuming liquid clusters, yields a cluster radius of ~350 nm (Figure 6.12). This value is clearly incorrect since we expect these clusters to be smaller than the those produced in a neat expansion due to the lower molecular density in the jet. However, if we assume that the clusters are crystalline in the latter stages of the expansion, we find that the cooling curve model yields a cluster radius of 6-12 nm (Figure 6.13), which is far more reasonable and is in accord with size estimates obtained for mix expansions of carbon dioxide. Also, Mayer has used Rayleigh scattering measurements in conjunction with CARS to deduce a cluster radius of 6-10 nm,[102] which is in excellent accord with the cooling curve results for crystalline methane.

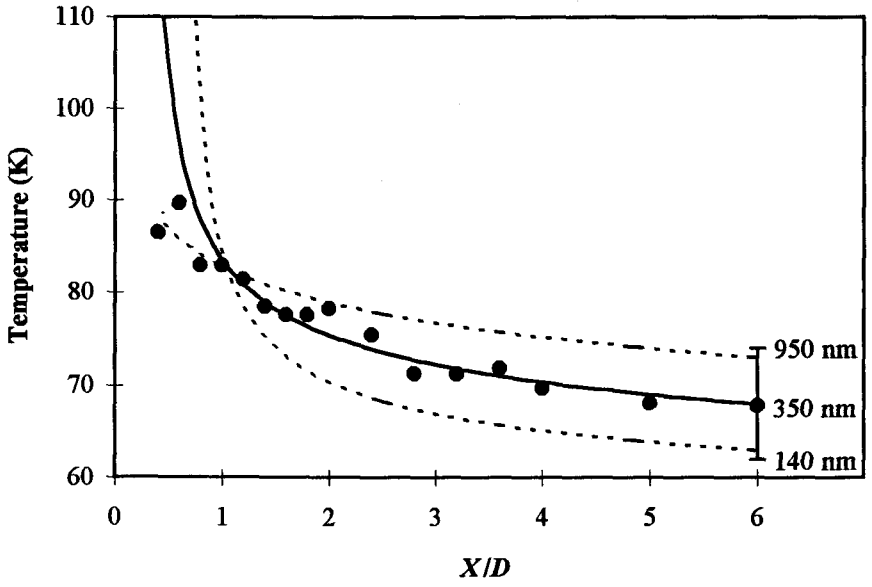

Figure 6.12 Cooling curve model for the 25% mix expansion assuming liquid clusters.

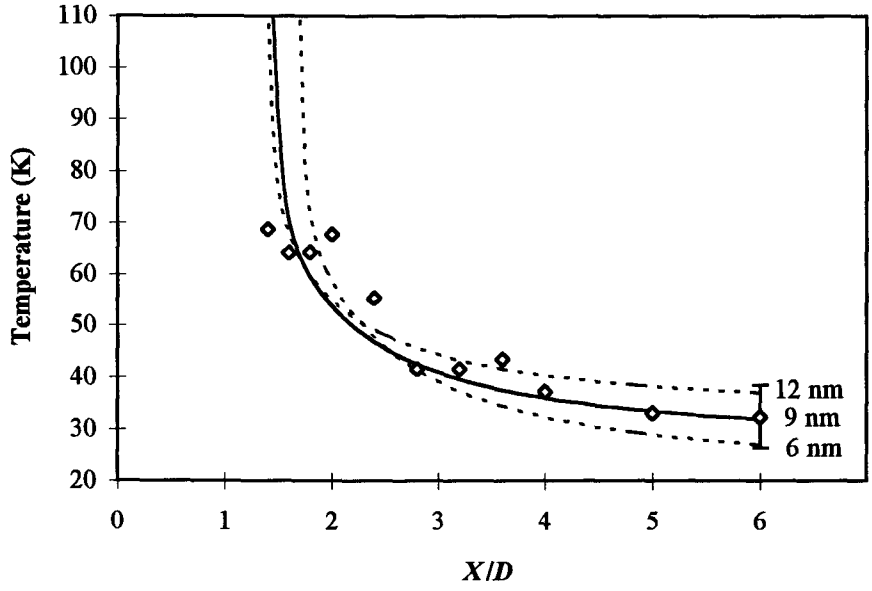

Figure 6.13 Cooling curve model for the 25% mix expansion assuming solid clusters.

Additional efforts were undertaken to directly confirm the presence of solid clusters. The above experiments were repeated by studying the ν_3 asymmetric stretch of methane, where the liquid and solid peaks are 10 cm^{-1} apart and clearly distinguishable from each other.[101] This transition, however, is unfortunately a thousand times weaker than the ν_1 symmetric stretch and as a result, it proved impossible to detect the presence of any clusters. We also considered studying the low frequency lattice modes, which could provide conclusive evidence that the clusters are crystalline. Unfortunately, the intensities of these too are extremely low;[103] hence we decided that the probability of observing these transitions was not high and the experiment was judged not worthwhile.

Overall, although we were not able to directly observe the liquid-solid phase transition of methane, we believe the evidence strongly indicates that freezing occurred in the mix expansion. Hence, we can estimate a nucleation rate by considering the limiting case, where all the clusters are liquid at $X/D = 0$ ($t = 0$ μs) and solid at $X/D = 6$ ($t = 1.5$ μs). This leads to a nucleation frequency of 0.7 MHz, which corresponds to a nucleation rate of 3.1×10^{29} m^{-3} s^{-1} for 8 nm clusters.

To determine σ_{sl} from this nucleation rate, we need to know the temperature of the liquid clusters at the onset of nucleation. This information cannot be extracted from our data since the liquid and solid peaks are indistinguishable. However, if freezing is completely adiabatic, then we might expect a temperature difference of about $\Delta H_{fus}/C_{p,liq}$ ~ 25 K between the liquid and solid clusters. Based on the solid temperatures shown in Figure 6.13, this would correspond to a liquid temperature of about 40 K. This temperature is slightly lower than the predicted evaporative cooling temperature of

44-46 K for methane but this is reasonable because the carrier gas will act as a heat sink and allow the clusters to cool below T_{evp}.

Using a nucleation temperature of 40 K, and the thermodynamic data in Table 6.1, we calculate a σ_{sl} value of 4.1 mJ/m^2, which is in good accord with values of 3.3 mJ/m^2 and 3.6 mJ/m^2 predicted from Turnbull and Tegze's relations, respectively. It should be noted that this experimental σ_{sl} value is an upper limit since the actual nucleation rate is expected to be higher than our estimated rate. Once again, the σ_{sl} value is much lower than the σ_{lv} value of 17.0 mJ/m^2 at the melting point or the extrapolated value of 28.4 mJ/m^2 at 40 K. From the latter result, and our σ_{sl}, we estimate a σ_{sv} value of 32.5 mJ/m^2 for solid methane at 40 K.

6.3 Final Remarks

Other systems which we have studied in our laboratory include methyl chloride, ethane, and ethylene. These molecules were chosen because the liquid and solid phases are readily distinguishable by Raman spectroscopy. Various mixtures and stagnation conditions were used to promote freezing of the liquid clusters. In all cases, however, the droplets remained in liquid form and we were unable to observe the liquid to solid phase transition. As we discuss below, the fact that some molecules do not crystallize in a jet is not only dependent on the experimental conditions but also on certain physical properties of the molecule being studied.

6.3.1 Kinetics of Freezing

The crystallization of a liquid clusters in a jet expansion is governed by thermodynamics, which determines whether the droplet will freeze, and kinetics, which determines how fast the droplet freezes. From the thermodynamic point of view, the cluster must be cold enough such that the formation of a critical nucleus is energetically favorable (see Figure 2.4). In our experiments, the clusters are supercooled by as much as 50 K and thermodynamics plays a minor role in the freezing process.

Kinetics is the key factor in the freezing process because the clusters must crystallize within the time scale of the experiment, which is of the order of 1-10 μs. In order for a liquid droplet to freeze, the molecules within the droplet must reorient themselves to form a crystal structure. The barrier to reorientation is dependent on the molecular geometry. For example, spherical and quasispherical molecules (e.g., rare gases, methane, sulfur hexafluoride) have a small orientational barrier and are able to readily organize themselves into crystalline form.[104] However, less symmetrical molecules such as ethane, benzene, and ethylene, require greater reordering to conform with the surface of a crystalline solid.

It is plausible to associate the barrier to molecular reorientation with the entropy of fusion.[105] This quantity is indicative of the amount of reordering necessary for a molecule to adhere to a crystalline structure. Thus, a small entropy of fusion implies a small barrier to molecular reorientation. Table 6.2 gives a brief listing of various materials along with their entropy of fusion and the observed phase of the cluster. Note that materials with a small entropy of fusion ($\Delta S_{fus}/R < 3$) tend to freeze while those with

a large entropy of fusion ($\Delta S_{fus}/R > 3$) remain in liquid form. There do, however, appear to be exceptions to this rule.

To account for these exceptions, Bartell has suggested that the range of liquid existence of a material also influences the phase of the clusters.[105-106] He argues that the greater the range of liquid existence, the more likely that clusters will remain in liquid form. Conversely, molecules with small liquid ranges tend to freeze to form solid clusters. On the basis of this argument, he has proposed an empirical index to predict the phase of the clusters. This index, h_c, is given by

$$h_c = \frac{T_b - T_m}{T_b} + 0.007\left(\frac{\Delta S_{fus}}{R}\right)^2 \qquad (6.2)$$

where $(T_b - T_m) / T_b$ is the range of liquid existence expressed in reduced form. The values in Table 6.1 indicate that materials with $h_c > 0.32$ yield liquid clusters while materials with $h_c < 0.32$ tend to produce liquid clusters which then freeze to form solid clusters. Thus, the combination of ΔS_{fus} and the range of liquid existence is a better criterion for predicting cluster phase than either individual property. As indicated in Table 6.2, this criterion predicts that methyl chloride, ethane, and ethylene will form liquid, and not solid, clusters, as observed.

6.3.2 Cluster Properties

Based on our experiments and available literature data, liquid clusters produced in a jet expansion exhibit certain unique properties. First, the cluster radius is on the

Table 6.2 Physical properties which influence the phase of a cluster.

	$\Delta S_{fus} / R$	$(T_b - T_m) / T_b$	h_c	Phase
PF_3	0.93	0.29	0.30	L/S
CCl_4	1.19	0.29	0.30	L/S
CH_4	1.25	0.16	0.17	L/S
N_2	1.37	0.18	0.19	L/S
Ar	1.69	0.04	0.06	L/S
C_2H_2	2.41	-0.02	0.00	L/S
H_2O	2.64	0.27	0.32	L/S
SF_6	2.72	-0.08	-0.03	S[a]
CS_2	3.28	0.38	0.56	L
NH_3	3.47	0.18	0.26	L/S
C_2H_5OH	3.81	0.55	0.65	L
C_2H_6	3.83	0.51	0.61	L
C_2H_4	3.87	0.39	0.49	L
C_6H_6	4.24	0.21	0.34	L
N_2O	4.31	0.01	0.14	L/S[b]
CH_3Cl	4.49	0.29	0.43	L
CO_2	4.63	-0.17	-0.02	S[a]
$CHCl_3$	5.05	0.37	0.55	L

[a]Materials with a negative h_c value bypass the liquid phase and form solid clusters.
[b]Although not observed in our experiments, it should be possible to form liquid N_2O clusters in a neat expansion with high P_0 and low T_0.

order of 5-25 nm and never exceeds this range since the molecular density falls rapidly in the expansion and there are not enough collisions for the cluster to grow.

In addition, nucleation occurs in a narrow temperature range and exhibits a constant rate. For neat expantions, nucleation tends to take place at the evaporative

cooling temperature while clusters formed in the presence of a carrier gas freeze at slightly lower temperatures. Furthermore, as with the liquid-vapor nucleation rate, the liquid-solid nucleation rate is nearly constant, of the order of 10^{29}-10^{30} m^{-3} s^{-1}.

The extraordinarily high nucleation rates observed in supersonic expansions are due to the small cluster size and the extremely cold temperatures attained in a jet. Other techniques, where temperatures are higher and clusters are larger than those in a jet, such as emulsions and cloud chambers,[12-13,23] display nucleation rates on the order of 10^{9}-10^{15} m^{-3} s^{-1} for H_2O and CCl_4. This observation is in accord with nucleation theory which predicts lower nucleation rates at higher temperatures due to the increase in the free energy barrier for the formation of a critical nucleus.

The observations above indicate that it is possible to estimate reasonable σ_{sl} values for clusters produced in a jet expansion without even observing a phase transition. Table 6.3 gives a list of molecules that have been studied in our laboratory and by Bartell at University of Michigan.[16,17,21,99] In cases where freezing was not observed, the nucleation rate is assumed to be of the order of 10^{29} m^{-3} s^{-1} and the nucleation temperature is taken to be T_{evp}. The estimated σ_{sl} values for these systems are in remarkable agreement with the values predicted by Turnbull and Tegze. Of course, this approximation yields a σ_{sl} value at a single temperature. If one is interested in determining the temperature dependence of σ_{sl}, then it is necessary to measure the nucleation rate at several different temperatures. Such studies might be warranted in future work, especially if accompanied by development of more sophisticated theoretical models for interfacial tensions.

Table 6.3 Experimental and predicted σ_{sl} values for various molecules.

	J ($\times 10^{29}$ m^{-3} s^{-1})	T (K)	σ_{sl} (mJ/m^2)	Turnbull (mJ/m^2)	Tegze (mJ/m^2)
N_2	1.5	38	3.5	2.7	3.4
CH_4	3.1	40	4.1	3.3	3.6
CH_3Cl	1.0	91	20.5	18.7	21.9
C_2H_4	1.0	54	11.4	9.4	10.7
C_2H_6	1.0	47	9.2	8.5	9.6
[a]C_6H_6	1.0	169	20.0	18.9	19.5
[b]CCl_4	1.1	175	5.5	5.0	5.4
[b]NH_3	12.0	120	23.0	27.0	25.6
[b]H_2O	10.0	200	22.0[c]	32.2	35.2

[a]Only liquid clusters observed by Ke at OSU and Bartell at Michigan.[105]
[b]Nucleation rate determined from electron diffraction studies by Bartell.[16,17,21,99]
[c]Value is for freezing to cubic ice while predicted values are for hexagonal ice.[21]

7. CONCLUSION

Interfacial tension is defined as an attractive force which acts parallel to the surface and prevents it from extending. This is a quantity which plays an important role in many industrial and atmospheric processes and is extremely difficult to measure when one of the phases is a solid. The work presented in this thesis has focused on theoretical and experimental determination of liquid-vapor (σ_{lv}), solid-vapor (σ_{sv}), and solid-liquid (σ_{sl}) interfacial tension of simple molecules.

In Chapter 4, we have used the mechanical definition of interfacial tension (1.7) to derive an equation for the liquid-vapor interfacial tension in terms of the intermolecular potential $u(r)$ and the radial distribution function $g(r)$. This equation was then used to calculate σ_{lv} using a hard-sphere and a Lennard-Jones 6-12 potential. The hard-sphere potential, which is hardly an accurate representation of the intermolecular forces but allows us to solve the problem analytically, yields negative σ_{lv} values. This unphysical result is not surprising considering the fact that interfacial tension is an attractive force while the hard-sphere potential has no attractive part.

Using a Lennard-Jones potential, which is a more realistic representation of the intermolecular forces, complicates matters since there is no analytic form for $g(r)$ which means that the problem must be solved numerically. We have used an algorithm to do this and have found that this model yields values which are in excellent agreement with experimental σ_{lv} values at temperatures much lower than the critical temperature. Additionally, we have calculated σ_{lv} values for several supercooled liquids and found that

the results are in good agreement with values obtained by linear extrapolation of the experimental points.

In Chapter 5 we demonstrate how Coherent anti-Stokes Raman Spectroscopy (CARS) can be used to measure the vapor-liquid nucleation rates. Experiments with liquid methane and ethylene show that the nucleation rate is of the order of 10^{26}-10^{27} m^{-3} s^{-1} for neat and dilute expansions. These rates are several orders of magnitude higher than rates observed in chamber experiments due to the rapid cooling rates achieved in jet expansions.

These nucleation rates are then used to calculate the interfacial tension of supercooled liquids. It is found that the measured values are significantly lower than the theoretical and extrapolated values. These is due to the small size of the clusters which leads to a lower value for the interfacial tension. By taking into account the variation of interfacial tension with size, we find that our experimental values are in good agreement with the theoretical and extrapolated values.

Additionally, the measured rates are expected to be relatively constant since the conditions in the expansion (i.e. cooling rates) change little from one molecule to another. Therefore, we propose that all that is required in the calculation of σ_{lv} are the temperature and pressure which lead to condensation. Rayleigh scattering, which is much simpler than CARS, has been used to determine the conditions at the onset of condensation for argon. This information is then used to calculate σ_{lv} for supercooled liquid argon which is found to be in satisfactory agreement with the theoretical and extrapolated values.

We have also employed CARS to measure the vapor-solid nucleation rate for nitrous oxide. As expected, the vapor-solid nucleation rate is of the same order of magnitude as the vapor-liquid nucleation rate. This nucleation rate is then used to calculate the interfacial tension of the solid. Using available data, we have also calculated σ_{sv} values for acetylene and carbon dioxide. We have found that the σ_{sv} values at a given temperature are significantly higher than the corresponding σ_{lv} values and that they exhibit the correct temperature dependence (i.e. increase with decreasing temperature). Since these are the first values of their kind, we have no theoretical or experimental values to which to compare our results.

Finally, CARS has been used to study the liquid to solid phase transition of several systems in order to determine the nucleation rate and hence, σ_{sl}. The nucleation rate for nitrogen is found to be of the order of 10^{29} m^{-3} s^{-1}, in agreement with nucleation rates reported for other molecules. A similar rate has been observed for the freezing of methane, implying once again that rates observed in a jet expansion are within a narrow range of values. The σ_{sl} values calculated from these nucleation rates are much smaller than the σ_{lv} value and are in good accord with predicted values. It has also been found that molecules with a high orientational barrier (i.e. ΔS_{fus}) tend to remain in liquid form in the expansion.

BIBLIOGRAPHY

1. Adam, N. K. *The Physics and Chemistry of Surfaces*, Humphrey: London, 1941.

2. Adamson, A. W. *Physical Chemistry of Surfaces*; Wiley: New York, 1967.

3. Bikerman, J. J. *Surface Chemistry for Industrial Research*; Academic: New York, 1958.

4. Neumann, A. W. *Adv. Colloid Interface Sci.* **1974**, *4*, 105.

5. Rowlinson, J. S.; Widom, B. *Molecular Theory of Capillarity*; Clarendon Press: Oxford, 1982.

6. Levine, I. N. *Physical Chemistry,* 3rd Ed.; McGraw-Hill: New York, 1988.

7. Moelwyn-Hughes, E. A. *Physical Chemistry,* 2nd Ed.; Pergamon: New York, 1961.

8. Jaycock, M. J.; Parfitt, G. D. *Chemistry of Interfaces*; Halsted: New York, 1981.

9. Oxtoby, D. W. Nucleation of Crystals from the Melt. In *Evolution of Size Effects in Chemical Dynamics*; Rice, S. A.; Wiley: New York, 1988; p. 263.

10. Skripov, V. P. Homogeneous Nucleation in Melts and Amorphous Films. In *Crystal Growth and Materials*; Kaldis, E.; North Holland: Amsterdam, 1977; Chapter 10.

11. Laaksonen, A.; Talanquer, V.; Oxtoby, D. W. *Annu. Rev. Phys. Chem.* **1995**, *46*, 489.

12. Turnbull, D.; Fisher, J. C. *J. Chem. Phys.* **1949**, *17*, 71.

13. Turnbull, D. *J. Appl. Phys.* **1950**, *21*, 1022.

14. Buckle, E. R. *Proc. Roy. Soc. London* **1961**, *A261*, 189.

15. Bradley, R. S. *Quart. Rev. Chem. Soc.* **1951**, *5*, 315.

16. Bartell, L. S.; Dibble, T. S. *J. Phys. Chem.* **1991**, *95*, 1159.

17. Bartell, L. S.; Chen, J. *J. Phys. Chem.* **1992**, *96*, 8801.

18. Bartell, L. S. *J. Phys. Chem.* **1990**, *94*, 5102.

19. Bartell, L. S.; Machonkin, R. A. *J. Phys. Chem.* **1990**, *94*, 6469.

20. Bartell, L. S.; Xu, S. *J. Phys. Chem.* **1994**, *98*, 6688.

21. Bartell, L. S. *J. Phys. Chem.* **1995**, *99*, 1080.

22. Koverda, V. P. *Fluid Mech. Soviet Res.* **1991**, *20*, 106.

23. Thomas, D. G.; Staveley, L. A. K. *J. Chem. Soc.* **1952**, 4569.

24. Udin, H.; Shaler, A. J.; Wulff, J. *J. Metals* **1949**, **1**, 186.

25. TAPP, Version 2.1; ES Microware, Inc., 2234 Wade Court, Hamilton, OH 45013.

26. Hobbs, P. V. *Ice Physics*; Clarendon Press: Oxford, 1974.

27. Bailey, A. I.; Kay, S. M. *Proc. Roy. Soc. London* **1967**, *A301*, 47.

28. Minarik, P. R. Ph.D. Thesis, Oregon State University, 1996.

29. Graedel, T. E.; Crutzen, P. J. *Atmospheric Change: An Earth System Perspective*; W.H. Freeman: New York, 1993.

30. Miller, D. R. Free Jet Sources. In *Atomic and Molecular Beam Methods*; Scoles, G., Ed.; Oxford University: Oxford, U.K., 1988; Vol. I, Chapter 2.

31. Gránásy, L.; Tegze, M.; Ludwig, A. *Mat. Sci. & Eng.* **1991**, *A133*, 577

32. Frenkel, J. *Kinetic Theory of Liquids*; Dover: New York, 1955.

33. Eyring, H. *J. Chem. Phys.* **1936**, *4*, 283.

34. Nibler, J. W.; Knighten, G. V. Coherent anti-Stokes Raman Spectroscopy. In *Topics in Current Physics*; Weber,A., Ed.; Springer: Berlin, 1979; Vol. 11, Chapter 7.

35. Herzberg, G. *Molecular Spectra and Molecular Structure: Infrared and Raman Spectra of Polyatomic Molecules*; Van Nostrand: Princeton, 1945.

36. Lee, K. H.; Triggs, N. E.; Nibler, J. W. *J. Phys. Chem.* **1994**, *98*, 4382.

37. Beck, R. D.; Hineman, M. F.; Nibler, J. W. *J. Chem. Phys.* **1990**, *92*, 7068.

38. Mayer, S. G. Ph.D. Thesis, Oregon State University, 1997.

39. Hagena, O. F.; Obert, W. *J. Chem. Phys.* **1972**, *56*, 1793.

40. Farges, J.; De Feraudy, M. F.; Raoult, B.; Torchet, B. *Surf. Sci.* **1981**, *106*, 95.

41. Cradock, S.; Hinchcliffe, A. J. *Matrix Isolation: A Technique for the Study of Reactive Inorganic Species*; Cambridge University Press: Cambridge, 1975.

42. Richardson, A. Ph.D. Thesis, Oregon State University, 1993.

43. Harrison, G. *The Dynamic Properties of Supercooled Liquids*; Academic Press: New York, 1976.

44. Yaws, C. L. *Handbook of Viscosity*; Gulf Publishing: Houston, 1995.

45. Angell, C. A.; Dworkin, A.; Figuière, P.; Fuchs, A.; Szwarc, H. *J. Chim. Phys.* **1985**, *82*, 773.

46. Bässler, H. *Phys. Rev. Lett.* **1987**, *58*, 767.

47. Rössler, E. *Ber. Bunsen-Ges. Phys. Chem.* **1990**, *94*, 392.

48. Takeda, K.; Oguni, M.; Suga, H. *J. Phys. Chem. Solids* **1991**, *52*, 991.

49. Takeda, K.; Oguni, M.; Suga, H. *Thermochimica Acta* **1990**, *158*, 195.

50. Sugawara, I.; Tabata, Y. *Chem. Phys. Lett.* **1976**, *41*, 357.

51. Maxwell, J. C. *The Scientific Papers of James Clark Maxwell*; Dover, New York, 1955.

52. Fowler, R. H. *Proc. Roy. Soc. A.* **1937**, *159*, 229.

53. Buff, F. P. *J. Chem. Phys.* **1955**, *23*, 419.

54. Kirkwood, J. G.; Buff, F. P. *J. Chem. Phys.* **1949**, *17*, 338.

55. Ono, S.; Kondo, S. *Handb. Phys.* **1960**, *10*, 134.

56. Navascués, G.; Berry, M. V. *Mol. Phys.* **1977**, *34*, 649.

57. McQuarie, D. A. *Statistical Mechanics*; Harper Collins: New York, 1976.

58. Irving, J. H.; Kirkwood, K. G. *J. Chem. Phys.* **1950**, *18*, 817.

59. Harasima, A. *Adv. Chem. Phys.* **1958**, *1*, 203.

60. Navascués, G. *Rep. Prog. Phys.* **1979**, *42*, 1132.

61. Weeks, J. D.; Chandler, D.; Andersen, H. C. *J. Chem. Phys.* **1971**, *54*, 5237.

62. Throop, G. J.; Bearman, R. J. *J. Chem. Phys.* **1965**, *42*, 2408.

63. Habenschuss, A.; Johnson, E.; Narten, A. H. *J. Chem. Phys.* **1981**, *74*, 5234.

64. McDonald, I. R.; Singer, K. *Mol. Phys.* **1972**, *23*, 29.

65. Rigby, M.; Smith, E. B.; Wakeham, W. A.; Maitland, G. C. *The Forces Between Molecules*; Clarendon Press: Oxford, 1986.

66. Monchick, L.; Mason, E. A. *J. Chem. Phys.* **1961**, *35*, 1676.

67. Shuttleworth, R. *Proc. Roy Soc. A.* **1950**, *63*, 444.

68. Young, T. *Phil. Trans. Roy. Soc.* **1805**, *95*, 65.

69. Gibbs, J. W. *The Collected Works of J. Willard Gibbs*; Yale University Press: New Haven, 1928.

70. Johnson, R. E. *J. Phys. Chem.* **1959**, *63*, 1655.

71. Zadumkin, S. N. *Phys. Met. Mettalogr.* **1962**, *13*, 22.

72. Ewing, R. H. *J. Cryst. Growth* **1971**, *11*, 221.

73. Jackson, K. A. *Liquid Metals and Solidification*; ASM: Cleveland, 1958.

74. Wolde, P. R.; Ruiz-Montero, M. J.; Frenkel, D. *J. Chem. Phys.* **1996**, *104*, 9932.

75. Vishnyakov, A.; Piotrovskaya, E. M.; Brodskaya, E. N. *J. Chem. Phys.* **1997**, *106*, 1593.

76. Beaker, W.; Mossman, A. L. *The Matheson Unabridged Gas Data Book*; Matheson: New Jersey, 1975.

77. Sychev, V. V.; Vasserman, A. A.; Golovsky, E. A.; Kozlov, A. D.; Spiridonov, G. A.; Tsymarny, V. A. *Thermodynamic Properties of Methane*; Hemisphere: Washington, 1987.

78. Wegener, P. P. *J. Phys. Chem.* **1987**, *91*, 2479.

79. Heist, R. H.; He, H. *J. Phys. Chem. Ref. Data* **1994**, *23*, 781.

80. Koppenwallner, G.; Düker, M. In *Progress in Astronautics and Aeronautics*; Fisher, S. S., Ed.; AIAA: New York, 1980; Vol. 74, Page 1190.

81. Williams, W. D.; Lewis, J. W. L. In *Progress in Astronautics and Aeronautics*; Potter, J. L., Ed.; AIAA: New York, 1977; Vol. 51, Page 1137.

82. Barschdorff, D.; Dunning, W. J.; Wegener, P. P.; Wu, B. J. C. *Nature (London), Phys. Sci.* **1972**, *240*, 166.

83. Tolman, R. C. *J. Chem. Phys.* **1949**, *17*, 333.

84. Bartell, L. S. *J. Phys. Chem.* **1987**, *23*, 5985.

85. Sivier, K. R. *Digital Computer Studies of Condensation in Expanding One-Component Flows*, Office of Aerospace Research USAF, ARL-Report, 1965.

86. Egan, C. J.; Kemp, J. D. *J. Amer. Chem. Soc.* **1937**, *59*, 1264.

87. Andersen, A.; Sun, T. S. *Chem. Phys. Lett.* **1971**, *8*, 537.

88. Costines, M. E.; Marsault-Herail, F.; Marsault, J. P.; Levi, G. *Mol. Phys.* **1979**, *38*, 1035.

89. Brown, K. W. Ph.D. Thesis, Oregon State University, 1991.

90. Koppenwallner, G.; Dankert, C. *J. Phys. Chem.* **1987**, *91*, 2482.

91. Blue, R. W.; Giauque, W. F. *J. Amer. Chem. Soc.* **1935**, *57*, 991.

92. Bourbo, P. S. *J. Phys.* **1943**, *7*, 286.

93. McGraw, R.; Laaksonen, A. *J. Chem. Phys.* **1997**, *106*, 5284.

94. Talanquer, V. *J. Chem. Phys.* **1997**, *106*, 9957.

95. Wilemski, G. *J. Chem. Phys.* **1995**, *103*, 1119.

96. Yang, M. Ph.D. Thesis, Oregon State University, 1990.

97. Kashchiev, D.; Verdoes, D.; van Rosmalen, G. M. *J. Cryst. Growth* **1991**, *110*, 373.

98. Burke, E.; Broughton, J. Q.; Gilmer, G. H. *J.Chem. Phys.* **1988**, *89*, 1030.

99. Huang, J.; Bartell, L. S. *J. Phys. Chem.* **1994**, *98*, 4543.

100. Giauque, W. F.; Clayton, J. O. *J. Amer. Chem. Soc.* **1933**, *55*, 4875.

101. Anderson, A.; Savoie, R. *J. Chem. Phys.* **1965**, *43*, 3469.

102. Mayer, S. Personal Communication, 1997.

103. Cabana, A.; Thé, N. D. *Can. J. Chem.* **1977**, *55*, 3862.

104. Sherwood, John, N. *The Plastically Crystalline State*; John Wiley & Sons: Chichester, 1979.

105. Bartell, L. S.; Harsanyi, L.; Valente, E. J. *J. Phys. Chem.* **1989**, *93*, 6201.

106. Bartell, L. S.; Valente, E. J.; Dibble, T. S. *J. Phys. Chem.* **1990**, *94*, 1452.

107. Wertheim, M. S. *Phys. Rev. Lett.* **1963**, *10*, 321.

108. Thiele, E. *J. Chem. Phys.* **1963**, *39*, 474.

109. Thiéry, M. M.; Fabre, D.; Kobashi, K. *J. Chem. Phys.* **1985**, *83*, 6165.

110. Torchet, G.; Farges, J.; De Feraudy, M. F.; Raoult, B. *Annals de Phys.* **1989**, *14*, 245.

111. Farges, J.; De Feraudy, M. F.; Raoult, B.; Torchet, G. *Ber. Bunsenges. Phys. Chem.* **1984**, *88*, 211.

APPENDICES

APPENDIX A. DERIVATION OF THE SHAPE FACTOR

The shape factor α is a variable which assures that the number of molecules on the surface of a nucleus of n molecules is equal to $\alpha n^{2/3}$.[15] Since the number of molecules on the surface is equal to the surface area of the nucleus divided by the area occupied by each molecule, we can write

$$\alpha n^{2/3} = \frac{4\pi r^2}{\upsilon_m^{2/3}} \tag{A.1}$$

where r is the radius of the nucleus and υ_m is the molecular volume. The volume of a spherical nucleus composed of n molecules is given by

$$V = n\upsilon_m = \frac{4}{3}\pi r^3 \tag{A.2}$$

Solving (A.2) for r gives

$$r = \left(\frac{3n\upsilon_m}{4\pi}\right)^{1/3} \tag{A.3}$$

Substituting (A.3) into (A.1) gives

$$\alpha n^{2/3} = 4\pi\left[\left(\frac{3n\upsilon_m}{4\pi}\right)^{1/3}\right]^2 \upsilon_m^{-2/3} \tag{A.4}$$

Solving (A.4) for α yields a value of $(36\pi)^{1/3} \approx 4.84$. Similarly, for a cubic nucleus of side l, (A.1) becomes

$$\alpha n^{2/3} = \frac{6l^2}{\upsilon_m^{2/3}} \tag{A.5}$$

while the volume of the nucleus is

$$V = n\upsilon_m = l^3 \tag{A.6}$$

Solving (A.6) for l and substituting into (A.5) gives

$$\alpha n^{2/3} = \frac{6(n\upsilon_m)^{2/3}}{\upsilon_m^{2/3}} \tag{A.7}$$

which shows that $\alpha = 6$ for a cubic nucleus.

APPENDIX B. HARD SPHERE $g(r)$

The following are two FORTRAN programs which are used to compute the hard-sphere radial distribution. The first program (START.FOR)[57] asks the user to enter the packing fraction and calls the subroutine GR.FOR which calculates $g_{hs}(r)$ by numerically inverting the Laplace transform of the Percus-Yevick equation.[62,107-108] The programs must be linked together during the compiling procedure.

```
C       Begin START.FOR
C       g(r) test program
        real rho
        dimension g(801),r(801)
        write(*,'(''Enter rho'')')
        read(*,*) rho
        dr = 0.01
        call talbot(g,r,rho,dr)
        do 10 i = 1,401
10      print*,r(i),g(i)
        stop
        end


C       Begin GR.FOR
C       HARD SPHERE G(R) PROGRAM
        SUBROUTINE TALBOT(GR,RR,RHO,DR)
C       FOR R = 1 TO R = 5
C       rho - the packing fraction.
        DIMENSION GR(801),RR(801)
        ROW = RHO*6.0/3.1415927
        DO 10 I = 1,401
        R = DR*FLOAT(I-1) + 1.0001
        Y = YD(ROW,R)
        GR(I) = Y
        RR(I) = R
10      CONTINUE
        RETURN
        END
        FUNCTION YD(row,r1)
C       Calculates yd(row,r1). Corrections made to PY using
C       method of Verlet and Weiss
        complex ex12,ig102,ig202,ig212,ig222,ig302,ig312,ig322,ig332,
     1  IG402,IG412,IG422,IG432,IG442,IT2,EX2,IXL1C,IXL2C,IXL3C,IXL4C,
     2  IXL5C,ILTC,JX,ISPC,ISDPC
```

```
      REAL LT,LT1,LT2,LP
      PI = ACOS(-1.0)
      K = 0
      RHOS = 0.0
      IF(K.NE.0)GO TO 1
      X = 2.0*PI/3.0
      JX = CEXP(CMPLX(0.0,X))
      K = 1
    1 IF(ABS(ROW-RHOS).LT.1.0E-04)GOTO 10
      RHOS = ROW
      ETAC = PI*ROW/6.0
      ETA = ETAC*(1.0-ETAC/16.0)
      ETAM = 1.0 - ETA
      BOT1 = ETAM**4
      TOP = 1.0 + 2.0*ETA
      TOP1 = TOP*TOP
      C1 = TOP1/BOT1
      BOT2 = 4.0*BOT1
      TOPP = 2.0 + ETA
      TOP2 = TOPP*TOPP
      C2 = -TOP2/BOT2
      C2 = 6.0*ETA*C2
      C3 = ETA*C1/2.0
      A1 = 0.75*ETA*ETA*(1.0-ETA*(0.7117 + 0.114*ETA))/BOT1
      A2 = 24.0*A1/ETA*ETAM*ETAM/(1. + 0.5*ETA)
      A3 = CUBER(ETAC/ETA)
C     ETA12 = 12.0*ETA
      LT1 = 1.0+ETA/2.0
      LT2 = 1.0+ 2.0*ETA
      LP = LT1
      XETA = 1.0/(1.0 - ETA)
      ETA3 = (1.0 - ETA)**2
      SP1 = 1.0
      SP2 = 4.0*ETA*XETA
      SP3 = 6.0*(ETA*XETA)**2
      SDP1 = 2.0
      SDP2 = SP2
      STP = 2.0
      FF = (3.0-ETA)*ETA + 3.0
      PAR = SQRT(1.+2.0*(ETA**2/FF)**2)
      YP = CUBER(1.0+PAR)
      YM = CUBER(1.0-PAR)
      PAR = CUBER(2.0*ETA*FF)
      T1 = XETA*(-2.0*ETA + PAR*(YP+YM))
      IT2 = XETA*(-2.0*ETA + PAR*(YP*JX + YM/JX))
      XF1 = 3.0*ETAM*ETAM
      PAR = ETA3**2/ETA
      XF2 = PAR*3./4.
      PAR = PAR*ETA3/ETA
      XF3 = PAR*3./8.
      PAR = PAR*ETA3/ETA
      XF4 = PAR*9./32.
      LT = LT1*T1 + LT2
      SDP = SDP1*T1+SDP2
      SP = (SP1*T1+SP2)*T1 + SP3
```

```
      EX11 = EXP(-T1)
      XL1 = (LT/SP)**2
      XL2 = 15.*SDP**2 - 4.0*SP*STP
      XL3 = LT + 4.*T1*LP
      XL4 = LT*SDP/SP
      XL5 = 2.*LT + 3.*T1*LP
      G101 = T1*LT/XF1/SP
      G201 = -LT/XF2/SP**2
      G211 = LT*(1.0 - T1*(2.+SDP/SP)) + 2.*LP*T1
      G221 = LT*T1
      G301 = LT/XF3/SP**3
      G311 = LT**2*T1/SP**2*(3.*SDP**2-SP*STP) - 3.*LT*SDP/SP*
     1       (LT+3.*T1*LP) + 6.*LP*(LT + LP*T1)
      G321 = LT*(6.0*LP*T1 + LT*(2.-3.*SDP*T1/SP))
      G331 = G221*LT
      G401 = -LT/XF4/SP**4
      G411 = 5.*T1*XL1*LT/SP*SDP*(2.*SP*STP - 3.*SDP**2) + XL1
     1       *XL2*XL3 - 24.*LP*XL4*XL5 + 12.*LP**2*(3.*LT + 2.*T1*LP)
      G421 = (T1*XL1*XL2 - 12.*(XL4*XL3 - LP*XL5))*LT
      G431 = (-6.*T1*XL4 + 3.*XL3)*LT**2
      G441 = G331*LT
      ILTC = LT1*IT2 + LT2
      ISDPC = SDP1*IT2 + SDP2
      ISPC = (SP1*IT2 + SP2)*IT2 + SP3
      EX12 = CEXP(-IT2)
      IXL1C = (ILTC/ISPC)**2
      IXL2C = 15.*ISDPC**2 - 4.*ISPC*STP
      IXL3C = ILTC + 4.*IT2*LP
      IXL4C = ILTC*ISDPC/ISPC
      IXL5C = 2.*ILTC + 3.*IT2*LP
      IG102 = IT2*ILTC/XF1/ISPC
      IG202 = -ILTC/XF2/ISPC**2
      IG212 = ILTC*(1. - IT2*(2. + ISDPC/ISPC)) + 2.*LP*IT2
      IG222 = ILTC*IT2
      IG302 = ILTC/XF3/ISPC**3
      IG312 = ILTC**2*IT2/ISPC**2*(3.0*ISDPC**2 - ISPC*STP) -3.*ILTC*
     1        ISDPC/ISPC*(ILTC + 3.*IT2*LP) + 6.*LP*(ILTC + LP*IT2)
      IG322 = ILTC*(6.*LP*IT2 + ILTC*(2. - 3.*ISDPC*IT2/ISPC))
      IG332 = IG222*ILTC
      IG402 = -ILTC/XF4/ISPC**4
      IG412 = 5.0*IT2*IXL1C*ILTC/ISPC*ISDPC*(2.*ISPC*STP
     1        -3.*ISDPC**2) + IXL1C*IXL2C*IXL3C - 24.*LP*IXL4C*IXL5C
     2        + 12.*LP**2*(3.*ILTC + 2.0*IT2*LP)
      IG422 = (IT2*IXL1C*IXL2C - 12.*(IXL4C*IXL3C - LP*IXL5C))*ILTC
      IG432 = (-6.*IT2*IXL4C + 3.*IXL3C)*ILTC**2
      IG442 = IG332*ILTC

10    R = R1*A3

      IF(R.GE.0.999999.AND.R.LE.5.0) GOTO 1010
      IF(R.GE.5.0)GOTO 1011

      R3 = R*R*R
      YD = C1 + C2*R + C3*R3
      RETURN
```

```
1011    YD = 1.0
        RETURN

1010    RRG = 0.0
C       FIRST SHELL
        EX1 = EX11*EXP(R*T1)
        EX2 = EX12*CEXP(R*IT2)
        RRG = RRG + G101*EX1 + 2.0*IG102*EX2
        IF (R.LE.2.0) GOTO 99

C       SECOND SHELL
        EX1 = EX1*EX11
        EX2 = EX2*EX12
        RRG = RRG + G201*EX1*(G211 + G221*R)
     1        + 2.*IG202*EX2*(IG212 + IG222*R)
        IF (R.LE.3.0) GOTO 99

C       THIRD SHELL
        RX = R - 3.0
        EX1 = EX1*EX11
        EX2 = EX2*EX12
        RRG = RRG + G301*EX1*((G331*RX + G321)*RX + G311) + 2.*IG302*
     1        EX2*((IG332*RX + IG322)*RX + IG312)
        IF(R.LE.4.0)GOTO 99

C       FOURTH SHELL
        RX = R - 4.0
        EX1 = EX1*EX11
        EX2 = EX2*EX12
        RRG = RRG + G401*EX1*(((G441*RX + G431)*RX + G421)*RX + G411) +
     1        2.*EX2*IG402*(((IG442*RX + IG432)*RX + IG422)*RX + IG412)

99      Z = A2*(R1 - 1.0)
        YD = RRG/R + A1/R1*EXP(-Z)*COS(Z)
        RETURN
        END

        FUNCTION CUBER(X)
C       CUBE ROOT
        IF(X.LT.0.0)GOTO 10
        CUBER = X**(1.0/3.0)
        RETURN
10      AX = -X
        AA = AX**(1.0/3.0)
        CUBER = -AA
        RETURN
        END
```

APPENDIX C. BULK METHANE DATA

Methane is the simplest hydrocarbon and is a quasi-spherical molecule which belongs to the T_d point group. According to group theory, methane has nine vibrational modes of which two are triply degenerate, one is doubly degenerate and one is singly degenerate. Table C.1 lists these modes along with the Raman frequencies reported in the literature.[101,103,109]

At 1 atm, methane condenses at 111 K, freezes at 91 K and undergoes a solid-solid phase transition at 20 K.[101] The higher temperature phase, referred to as solid I, is orientationally disordered and considered a plastic crystal. This is due to the fact that the molecule is a spherical top. Many other quasi-spherical molecules exhibit this property (e.g.. CF_4, SF_6, $C(CH_3)_4$).[104] The low temperature phase, referred to as solid II, is the famous James-Keenan phase with each unit cell containing six molecules in the D_{2d} symmetry site and two molecules in the O_h symmetry site.[109] In both solid phases, the carbon atoms form an f.c.c. lattice with a nearest neighbor distance of 4.17 Å.[53-54]

It was decided to study the ν_1 fully symmetric C-H stretch of methane. The advantage of the ν_1 fundamental is that it has a very large Raman cross section meaning that even small concentrations of methane give rise to a large signal. The disadvantage is that the liquid and solid frequencies are very close to each other, making it difficult to distinguish between the two phases.

It is necessary to study the bulk liquid and solid to determine the temperature dependence of the vibrational frequency so that we may determined the temperature of

Table C.1 Vibrational modes and frequencies for all phases of methane.

Mode	Vapor (cm^{-1})	Liquid (cm^{-1})	Solid I (cm^{-1})	Solid II (cm^{-1})
$\nu_1 (A_1)$	2916.5	2905	2904	2902 2908
$\nu_2 (E)$	3018.7	3020	3030	3009
$\nu_3 (T_2)$	1534	1535	1538	1526 1530 1553
$\nu_4 (T_2)$	1306	1300	-----	-----

clusters from their vibrational frequencies. Equilibrium samples were prepared in a cryostat and cooled to 15 K as described in Chapter 3; spectra were taken at 5 K intervals. Figure C.1 shows spectra of the two solid phases and the liquid phase of methane at selected temperatures. The temperature of the liquid is above the boiling point because the vapor above the sample was at up to 2 atm pressure. Table C.2 lists the frequencies and the linewidths at full-width half-maximum (FWHM) for the liquid and two solid phases as a function of temperature.

The liquid peak is located at ~2905 cm^{-1} and is about 3 cm^{-1} wide. As the liquid is cooled, the peak shifts to lower frequency and the width decreases. Solid I is located at ~2904 cm^{-1} and has a FWHM of about 2 cm^{-1}. This peak also shifts to lower frequency and narrows as the solid is cooled. Solid II gives rise to two peaks located at ~2902 cm^{-1} and 2908 cm^{-1}. The reason for this splitting is due to the fact that the unit cell has molecules in two different symmetry sites. Both of these peaks shift to lower frequencies as the sample is cooled.

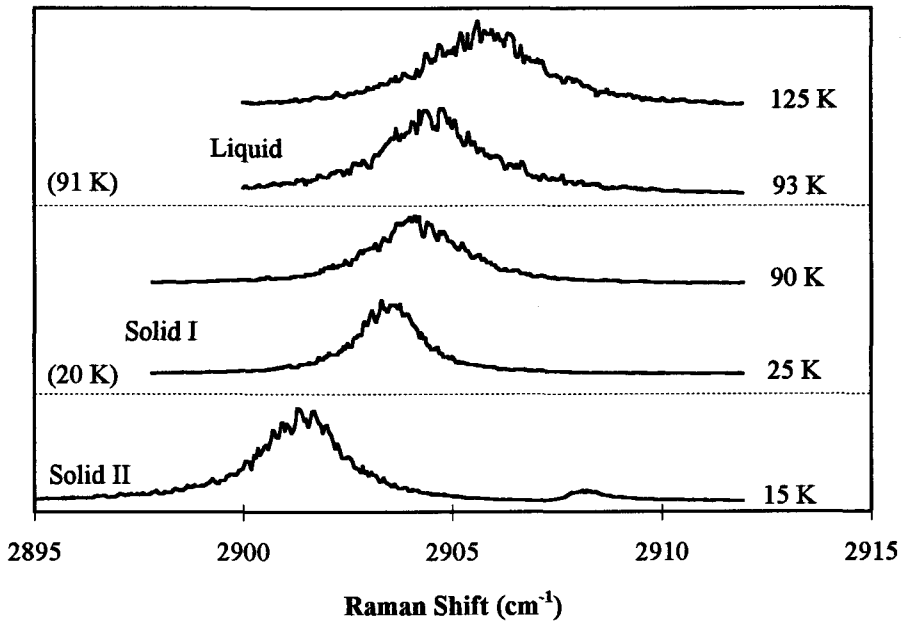

Figure C.1 Raman spectrum of condensed methane at selected temperatures. The numbers in parentheses correspond to the phase transition temperatures.

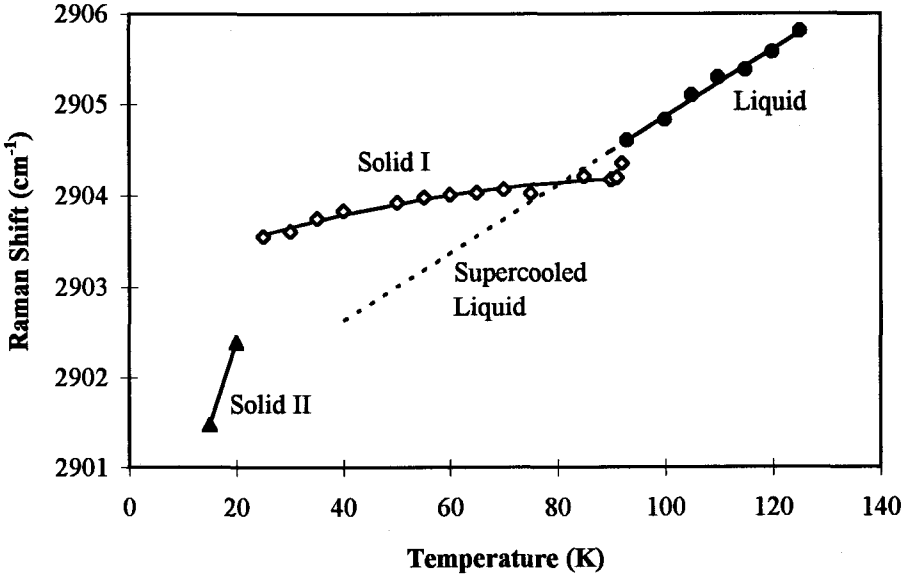

Figure C.2 Temperature dependence of the ν_1 vibrational frequency of methane. The dashed line is a linear extrapolation of the liquid data into the supercooled regime.

Table C.2 Vibrational frequencies and linewidths for liquid and solid methane at various temperatures.

	Liquid		Solid I		Solid II	
T (K)	ω (cm^{-1})	Δω (cm^{-1})	ω (cm^{-1})	Δω (cm^{-1})	ω (cm^{-1})	Δω (cm^{-1})
125	2905.81	3.02				
120	2905.57	3.09				
115	2905.38	2.78				
110	2905.29	2.83				
105	2905.11	2.99				
100	2904.83	2.75				
93	2904.61	2.85				
91			2904.21	2.39		
90			2904.18	2.22		
85			2904.21	2.31		
75			2904.03	2.39		
70			2904.07	2.11		
65			2904.04	1.82		
60			2904.02	1.84		
55			2903.99	1.84		
50			2903.93	1.69		
40			2903.84	1.64		
35			2903.75	1.79		
30			2903.61	1.93		
25			2903.56	1.61		
20					2902.39	2.08
					2908.24	1.32
15					2901.47	2.25
					2908.32	0.71

[a]Listed frequencies and linewidths are accurate to within 0.05 cm^{-1} and 0.1 cm^{-1}, respectively. Raw data is located in CH4-XXK.PRN where XX corresponds to the temperature. A correction factor of 0.60 cm^{-1} was added to all frequencies to account for the dye laser offset.

Figure C.2 shows a plot of the Raman shift versus temperature. The temperature dependence of the ν_1 vibrational frequency for the liquid and solid I are represented by

$$\omega_{liq}(cm^{-1}) = 2901.197 + 3.67 \times 10^{-2} T \qquad (C.1)$$

$$\omega_{sol(I)}(cm^{-1}) = 2903.110 + 2.13 \times 10^{-2} T - 1.04 \times 10^{-4} T^2 \qquad (C.2)$$

with a standard error of 0.045 cm^{-1} for the liquid and 0.041 cm^{-1} for the solid. The solid data could also be well represented by a linear fit. The application of appropriate statistical tests show, however, that the quadratic equation is significantly better. Thus, for a given cluster frequency, (C.1) and (C.2) can be used to deduce the cluster temperature.

In our jet experiments, we form supercooled liquid clusters and would like to know the temperature of these clusters. This is a problem for we cannot study the temperature dependence of the vibrational frequency of supercooled equilibrium samples. Due to lack of knowledge regarding the behavior of the vibrational frequency in the supercooled regime, we are forced to linearly extrapolate (C.1) into the supercooled region.

APPENDIX D. CLUSTER DATA FOR METHANE & ETHYLENE

Cluster data obtained for methane and ethylene are listed in the following tables. Table D.1 lists the frequencies and linewidths for both monomer and clusters observed in a neat expansion. Table D.2 sows the same data obtained for the 25% expansion of methane. Also listed in both tables are the calculated cluster temperatures, assuming either liquid or solid, from the temperature-frequency relations obtained in Appendix C. Data for the 15% expansion is not shown explicitly. However, the raw data files are available and listed in Table D.3. The raw data files for the expansions of ethylene are also available and the filenames are listed in Table D.4.

Table D.1 Frequencies and linewidths for methane monomer and clusters produced in a neat expansion. Calculated cluster temperatures are also shown assuming all liquid or solid phase.

	Monomer[a]		Cluster[b]		Cluster Temp.[c]	
X/D	ω (cm^{-1})	Δω (cm^{-1})	ω (cm^{-1})	Δω (cm^{-1})	Liquid (K)	Solid (K)
0.8	2916.55	0.67	2904.98	4.24	103.1	
1.0	2916.56	0.41	2904.35	4.04	85.9	
1.2	2916.55	0.63	2904.55	4.15	91.2	>120
1.4	2916.57	0.51	2903.43	4.27	60.9	16.6
1.6	2916.54	0.49	2903.69	4.17	67.9	32.7
2.3	2916.55	0.45	2903.64	3.88	66.4	28.7
2.6	2916.55	0.45	2903.28	4.11	56.7	8.4
2.8	2916.58	0.41	2904.02	4.07	76.8	60.7
3.0	2916.56	0.48	2903.88	4.21	72.9	46.8
3.4	2916.58	0.58	2903.47	4.25	61.9	18.7
4.0	2916.57	0.61	2903.39	4.16	59.9	14.6
5.0	2916.52	0.54	2903.37	3.94	59.1	12.9
6.0	2916.53	0.53	2903.27	3.99	56.3	7.7
7.0	2916.55	0.51	2903.22	3.84	55.1	5.5
8.0	2916.52	0.45	2903.01	4.08	49.1	-4.9
9.0	2916.54	0.47	2902.74	3.95	42.1	-15.9
10.0	2916.55	0.37	2903.06	3.76	50.7	-2.4
13.0	2916.54	0.41	2902.81	3.57	43.8	-13.4
15.0	2916.54	0.34	2902.81	3.79	43.8	-13.4
16.0	2916.52	0.36	2902.96	3.97	47.9	-6.9
18.0	2916.53	0.32	2902.91	4.03	46.6	-9.1
19.0	2916.49	0.36	2902.82	3.71	44.1	-13.1
20.0	2916.51	0.31	2902.94	3.74	47.5	-7.7

[a]Monomer frequencies and linewidths are accurate to within 0.05 cm^{-1} and 0.1 cm^{-1}, respectively. [b]Cluster frequencies are accurate to within 0.2 cm^{-1} and linewidths are accurate to within 0.8 cm^{-1}. [c]Calculated liquid and solid temperatures have an uncertainty of ±5 K and ±10 K, respectively.

Table D.2 Frequencies and linewidths for methane monomer and clusters in a 25% mix expansion. Calculated cluster temperatures are also shown assuming all liquid or solid phase.

	Monomer[a]		Cluster[b]		Cluster Temp.[c]	
X/D	ω (cm^{-1})	Δω (cm^{-1})	ω (cm^{-1})	Δω (cm^{-1})	Liquid (K)	Solid (K)
0.4	2916.71	0.32	2904.35	3.43	86.42	
0.6	2916.69	0.28	2904.42	3.32	89.66	
0.8	2916.66	0.33	2904.21	3.91	82.91	>120
1.0	2916.66	0.33	2904.14	4.31	82.94	102.23
1.2	2916.63	0.33	2904.19	5.47	81.41	92.77
1.4	2916.61	0.33	2904.04	3.52	78.5	68.79
1.6	2916.59	0.38	2903.99	3.36	77.58	64.22
1.8	2916.58	0.35	2903.97	3.19	77.61	64.35
2.0	2916.57	0.37	2904.01	3.41	78.31	67.81
2.4	2916.58	0.35	2903.92	3.18	75.45	55.38
2.8	2916.57	0.36	2903.86	3.35	71.26	41.61
3.2	2916.57	0.36	2903.81	3.07	71.23	41.53
3.6	2916.54	0.300	2903.72	3.11	71.86	43.38
4.0	2916.56	0.25	2903.71	2.93	69.68	37.17
5.0	2916.55	0.27	2903.47	2.85	68.13	33.09
6.0	2916.54	0.23	2903.36	2.72	67.86	32.41

[a]Monomer frequencies and linewidths are accurate to within 0.05 cm^{-1} and 0.1 cm^{-1}, respectively. [b]Cluster frequencies and linewidths are accurate to within 0.1 cm^{-1} and 0.5 cm^{-1}. [c]Calculated liquid and solid temperatures have an uncertainty of ±3 K and ±6 K, respectively.

Table D.3 Location of raw data files for methane clusters. All data file names have a .PRN extension.

Neat[a]		25% Mix[b]		15% Mix[b]	
X/D	Filename	*X/D*	Filename	*X/D*	Filename
0.8	CH4C51	0.4	CH4CHE10	0.4	CH4CHE1
1.0	CH4C55	0.6	CH4CHE11	0.6	CH4CHE2
1.2	CH4C50	0.8	CH4CHE12	0.7	CH4CHE5
1.4	CH4C56	1.0	CH4CHE13	0.8	CH4CHE3
1.6	CH4C49	1.2	CH4CHE14	0.9	CH4CHE6
2.3	CH4C57	1.4	CH4CHE15	1.0	CH4CHE4
2.6	CH4C47	1.6	CH4CHE16	1.2	CH4CHE8
2.8	CH4C58	1.8	CH4CHE17	1.4	CH4CHE7
3.0	CH4C46	2.0	CH4CHE18		
3.4	CH4C59	2.4	CH4CHE19		
4.0	CH4C25	2.8	CH4CHE20		
5.0	CH4C26	3.2	CH4CHE21		
6.0	CH4C27	3.6	CH4CHE22		
7.0	CH4C28	4.0	CH4CHE23		
8.0	CH4C29	5.0	CH4CHE24		
9.0	CH4C30	6.0	CH4CHE25		
10.0	CH4C31				
13.0	CH4C34				
15.0	CH4C36				
16.0	CH4C37				
18.0	CH4C39				
19.0	CH4C40				
20.0	CH4C41				

[a]A correction factor of 1.08 cm^{-1} must be added to all frequencies.
[b]A correction factor of 1.24 cm^{-1} must be added to all frequencies.

Table D.4 Location of raw data files for ethylene clusters. All data file names have a .PRN extension.

25% Mix (233 K)[a]		25% Mix (273 K)[a]	
X/D	Filename	*X/D*	Filename
0.2	C2H4-30	0.4	C2H4-19A
0.4	C2H4-29	0.6	C2H4-18A
0.6	C2H4-28	0.9	C2H4-17A
0.9	C2H4-27	1.1	C2H4-16A
1.1	C2H4-26	1.4	C2H4-15A
1.4	C2H4-25	1.6	C2H4-14A
1.6	C2H4-24	1.9	C2H4-13A
1.9	C2H4-23	2.1	C2H4-12A
2.1	C2H4-22	2.4	C2H4-11A
2.4	C2H4-21	2.6	C2H4-10A
2.6	C2H4-20	2.9	C2H4-9A
2.9	C2H4-19	3.1	C2H4-8A
3.1	C2H4-18	3.4	C2H4-7A
3.4	C2H4-17	3.9	C2H4-6A
3.6	C2H4-16	4.4	C2H4-5A
3.9	C2H4-15	4.9	C2H4-4A
4.1	C2H4-14	5.4	C2H4-3A
4.4	C2H4-12	5.9	C2H4-2A
4.6	C2H4-13	6.4	C2H4-1A
4.9	C2H4-11		
5.4	C2H4-10		
5.9	C2H4-9		
6.4	C2H4-8		
6.9	C2H4-7		
7.4	C2H4-6		
7.9	C2H4-5		

[a]No correction factor for the measured frequencies is available.